Spring 2019

# Diffusion kinetics in promising adsorbents for gas capture processes

Teresa Gelles



Department:

# DIFFUSION KINETICS IN PROMISING ADSORBENTS FOR GAS CAPTURE PROCESSES

by

TERESA MARIE GELLES

A THESIS

Presented to the Faculty of the Graduate School of the

MISSOURI UNIVERSITY OF SCIENCE AND TECHNOLOGY

In Partial Fulfillment of the Requirements of the Degree

MASTER OF SCIENCE IN CHEMICAL ENGINEERING

2019

Approved by:

Fateme Rezaei, Advisor
Ali A. Rownaghi
Joseph Smith

## PUBLICATION THESIS OPTION

This thesis consists of the following two articles:

Paper I: Pages 10-54 have been submitted to Chemical Engineering Science

Paper II: Pages 55-99 have been submitted to AICHE Journal

## ABSTRACT

This reports the results of experimental studies aimed at characterizing the transport properties of promising adsorbents for various gas capture processes by the "zero length column" (ZLC) technique. ZLC was used to measure the intracrystalline diffusivities of single and binary components of ethane and ethylene in powder and pellet samples of paraffin-selective adsorbents Ni(bdc)(ted)$_{0.5}$ (Ni-BT) and ZIF-7 for the purpose of olefin/paraffin separation. Results show that binary gaseous systems result in intracrystalline diffusion time constants slightly lower than those in single component gaseous streams due to coadsorption effects. It was also found that ethylene diffusion was affected by surface resistances due to strong interactions between the C-C double bond at adsorbent pore entrances. Additionally, $CO_2$ sorption kinetics of poly(ethylenimine) (PEI)-impregnated MIL-101, γ-alumina, and UVM-7 silica were investigated via ZLC for the purposes of understanding the effect of amine-content, adsorbent porosity, and adsorption temperature on $CO_2$ sorption rates. It was found that increasing the amine content resulted in diminished diffusion rates and that microporous MIL-101 yielded substantially slow desorption rates upon amine-functionalization compared to mesoporous γ-alumina. Additionally, research yielded faster sorption kinetics at higher temperatures for PEI-impregnated silica and showed that upon desorption, this material exhibited two distinct regions of mass transfer control that is best explained by first the occurrence of surface diffusion followed by diffusion out of the branched PEI amine.

# ACKNOWLEDGEMENTS

I am sincerely grateful to all of the staff and faculty in the Chemical Engineering Department, and to all of those who have helped me during this time.

In particular, I would like to take this opportunity to express my utmost gratitude to my thesis advisor, Dr. Fateme Rezaei, for her advice and guidance over the course of this study. I am deeply grateful for all of the opportunities that she has provided me. I consider myself truly fortunate to have had to opportunity to work for such a great mentor. I would also like to acknowledge and thank Dr. Ali Rownaghi for all of his support, guidance, and mentorship, and I would like to express a special appreciation to Dr. Joseph Smith for his support serving on my thesis committee.

My greatest appreciation goes to my parents Sundhya and Gregory, and brother Aidan, for their perpetual support throughout all of my endeavors. I especially would like to acknowledge Aaron, for his love, motivation, and encouragement, even across great distances.

# TABLE OF CONTENTS

# LIST OF ILLUSTRATIONS

SECTION Page

# LIST OF TABLES

# NOMENCLATURE

| SYMBOL | DESCRIPTION |
|---|---|
| $\beta_1$ | Roots of transcendental equation, dimensionless |
| $C$ | ZLC outlet concentration, mol/cm$^3$ |
| $C_0$ | ZLC saturation concentration, mol/cm$^3$ |
| $D_c$ | Crystalline diffusion, cm$^2$/s |
| $D_K$ | Knudsen diffusion, cm$^2$/s |
| $D_m$ | Molecular diffusion, cm$^2$/s |
| $D_P$ | Macropore diffusion, cm$^2$/s |
| $\varepsilon_P$ | Pellet porosity, dimensionless |
| $\gamma$ | ZLC model parameter, dimensionless |
| $F$ | ZLC purge flow rate, cm$^3$/s |
| $H$ | Henry's Law, mmol/g bar |
| $k$ | Surface mass transfer coefficient, cm/s |
| $K$ | Henry's Law Constant, dimensionless |
| $L$ | ZLC model parameter, dimensionless |
| $P$ | Pressure, bar |
| $\rho_P$ | Pellet density, g/cm$^3$ |
| $L´$ | ZLC apparent model parameter, dimensionless |
| $q$ | Amount adsorbed, mmol/g |
| $r_c$ | Crystal radius, cm |
| $R_P$ | Pellet radius, cm |

| | |
|---|---|
| $t$ | Time, s |
| $V_g$ | ZLC dead volume, $cm^3$ |
| $V_s$ | Volume of adsorbent, $cm^3$ |

SECTION

# 1. INTRODUCTION

## 1.1 OLEFIN/PARAFFIN SEPARATION

Light olefins such as ethylene and propylene are the most important chemical feedstocks used in the petrochemical industry. Serving as the building blocks for the production of many types of chemicals, plastics, polymers, and rubbers, light olefins are produced in larger quantities than any other kind of organic compound [1]. The production of olefins requires the separation of the olefin from its corresponding paraffin and is generally done by means of distillation. However, due to the similar sizes and low relative volatilities of olefin and paraffins such as ethylene and ethane, they must be separated by cryogenic distillation [2]. The high pressure and low temperature requirements for cryodistillation represents one of the most costly gas separations in the chemical and petrochemical industry, requiring an energy demand of up to 30% of the total cost of the entire production process [3]. Therefore, finding an alternative method that can be used in the separation of olefins and paraffins that does not require the same energy demands of cryodistillation is highly sought after.

Many alternatives to cryodistillation have been investigated, including absorption, membrane-based, and adsorption separations [1]. Proposed absorption technologies include reactive absorption processes where light olefin molecules would form reversible chemical complexations with transition metal ions, and where they could then be separated from their corresponding paraffin using a mass-separating agent such as a

selective membrane [1,4,5]. While this method would not require the high energy demands of cryodistillation, absorption-based technologies still suffer from high energy requirements and poor solvent chemical stability, making it an ineffective alternative to the current technology. Selective membranes have also been widely researched as a potential alternative. Such selective membranes include carbon molecular sieve (CMS) membranes, polymer composite membranes, and MOF/polymeric mixed matrix membranes [6–10]. While membranes are advantageous in the sense that they can be selectively designed to meet a number of different demands, they suffer from issues surrounding poor thermal and chemical stability and poor selectivity. They are also far too costly to economically scale up for industrial use and would therefore be a poor alternative to ethylene/ethane separation [11].

Adsorption-separation technologies are an attractive alternative to cryodistillation due to both the maturity of the technology and the continual development of novel adsorbents that can be synthesized to have high adsorption selectivity to a desired sorbent. Historically, adsorbents that have been studied for the purposes of olefin/paraffin separations have preferential selectivity to olefins over paraffins due to the $\pi$-complexation formed between the olefin and adsorbent. Such adsorbents include zeolite 4A, CMS, and $Ag^+$ exchanged resins [12–15]. While this is an attractive mode of adsorption due to the strong bonds formed by the complexations, these bonds also result in significant energy requirements upon desorption. Additionally, once desorbed an additional step is then required to recover the olefin, resulting in lower recovery and purity rates [16,17].

Adsorption separation by means of paraffin-selectivity would mitigate the need for this additional step upon desorption and would not impose the same energy requirements due to the weaker van der Waals forces formed between paraffin and adsorbent. The most promising paraffin-selective adsorbents that have been investigated thus far include metal organic frameworks (MOFs) [18–22]. MOFs are hybrid materials consisting of metal ions coordinated to organic ligands. Unlike traditional adsorbents such as zeolites, MOFs can undergo structural changes caused by non-covalent interactions such as van der Waals forces upon the adsorption of different sorbents. These features, through the selection of appropriate building blocks, allow for the well-controlled design and synthesis of MOFs to be suited to meet a number of demands, including olefin and paraffin gas separations and storage [23–27]. Two subclasses of MOFs that have exhibited high ethane selectivity for the separation of ethane and ethylene are zeolite imidazolate frameworks (ZIFs) and pillard-layered MOFs [20–22].

ZIFs are an attractive option for many gas separation purposes due to their excellent thermal stability, hydrophobic properties, and wide topological varieties. ZIF-7 has a sodalite topology with a crystallographic six-membered ring pore opening and has been shown to exhibit strong paraffin selectivity over olefin through a gate-opening mechanism. ZIF-7 has exhibited an ethane uptake of 3.21 mmol/g at 25 °C and 1 bar [21,28]. $Ni(bdc)(ted)_{0.5}$ (Ni-BT) is a type of pillard-layers MOF that is comprised of 3D paddle-wheel building units composed of Ni cations and two organic linkers and has exhibited high ethane adsorption of 5.11 mmol/g at 25 °C and 1 bar [22,28]. The current research focus for paraffin-selective MOFs has been the adsorptive characterization of powders. In our previous work, we expanded upon the current research and examined the

large-scale feasibility of ZIF-7 and Ni-BT by investigating the adsorptive capacities of ZIF-7 and Ni-BT coated monoliths [28]. Monoliths allow for easy adoption into a wide range of gas separation processes and serves as a suitable bed of contact between gas and adsorbent. MOF-coated monoliths can be further formulated into pellets for integration into laboratory and industrial settings [29].

In cyclic processes where adsorbent is saturated and regenerated, understanding the mass transfer in and out of an adsorbent is significant and has lasting effects on the performance and efficiency of the process, especially when dealing with large industrial operations. While adsorption behavior has been investigated and modeled for ZIF-7 and Ni-BT [21,22], the transport properties of ethane and ethylene in these materials is unknown. This serves as the motivation of study of Paper I.

## 1.2 ANTHROPOGENIC $CO_2$ CAPTURE

Rising $CO_2$ emissions resulting from fossil fuel combustion has been widely regarded as the primary cause to the rise in global temperatures, and it is generally accepted that these fossil fuels will remain the main source of energy production for at least the next fifty years [30]. In order to limit the average global temperature rise to between 2 – 2.4 °C, a 50 % reduction in global $CO_2$ emissions is necessary [31]. Therefore, the rapid deployment of cost-effective carbon capture and sequestration (CCS) technologies are essential for the mitigation of $CO_2$ in the short term [32–35]. CCS refers to technologies that can selectively capture and store up to 90 % of $CO_2$ emissions produced from gaseous streams at large-point sources. Captured and stored $CO_2$ can then be utilized in a variety of ways, including as a feedstock for the production of many

chemical processes and fuels [36] or as a safer and more environmentally friendly alternative to hydrofracking [37].

CCS technologies consist of three primary routes, including (i) the direct removal of $CO_2$ from flue gas streams (post-combustion capture), (ii) the capture of $CO_2$ utilizing reformed synthesis gas from an upstream gasification unit (pre-combustion capture), or (iii) the utilization of pure oxygen for fuel combustion (oxyfuel combustion) [36]. Capturing $CO_2$ at different source points accrues different energy penalties that are dependent upon the industry in question. Power plants alone account for almost 45 % of world-wide $CO_2$ emissions [38], and the industrial integration of post-combustion capture onto power plants has been viewed as the most promising form of $CO_2$ abatement.

Many post-combustion CCS technologies have been investigated, including membrane, absorption, and adsorption-based $CO_2$ capture [34]. $CO_2$ capture by membrane separation have been shown to effectively operate under continuous conditions, and, as long as a minimum pressure gradient is maintained across the membrane, $CO_2$ and other flue gas components will permeate. Additionally, membranes can be finely tuned in order to meet a number of different gas demands, including membrane configuration and composition. Polymeric and mixed matrix membranes (MMM) and have been tested for $CO_2$ separation from post-combustion flue gas. However, the low pressure of flue gas streams can render membranes impractical as they are generally better suited for high-pressure applications [39,40].

Chemical absorption via amines or ammonia is the most mature separation method used in various industries, such as power plants or oil refineries [41]. Aqueous monoethanol amine (MEA) absorption is considered the benchmark technology for $CO_2$

capture that can capture > 90 % of $CO_2$ from flue gas streams, but results in high energy penalties upon solvent regeneration that would, if applied, raise the cost of electricity production by 70 %, making it uneconomical for large-scale implementation [42,43]. Additionally, equipment corrosion and poisoning from flue gas impurities further diminish the stability of the solvents and reduce working capacities.

In recent years, solid-state adsorption has arisen as an attractive and cost-effective alternative to absorption-based amine scrubbing. Solid adsorbents, traditionally including zeolites, carbon molecular sieves, activated carbons, activated alumina, and metal-organic frameworks (MOFs), are physical adsorbents and have been extensively studied due to their low capture costs, low regeneration requirements, and long-term stability [44]. However, these adsorbents suffer from inferior capture capacities compared to aqueous amine-scrubbing, as well as reduced working capacities in humidified conditions [45,46]. Therefore, recent research has focused on the incorporation of amine-moieties onto physical adsorbents in order to enhance the $CO_2$ selectivity and adsorption capacity of these materials. Solid supported amine-adsorbents couple the effects of chemical and physical adsorption and offer many advantages over typical solid adsorbents, including superior heats of adsorption, high $CO_2$ equilibrium capacities, high efficiencies in humidified conditions, and fast adsorption kinetics [47–50].

Often, mesoporous materials, such as aluminas and silicas, are chosen for amine-functionalization due to large surface areas and pore volumes that can achieve dispersed amine loadings and enhance diffusional transport of $CO_2$ onto the amine [51,52]. More recently, MOFs have arisen as potential supports for amine-functionalization due to high

pore volumes and exceptional chemical and thermal stabilities. In particular, MIL-101(Cr) has shown incredible promise due to enhanced $CO_2$ uptakes at low partial pressures (400 ppm) [26,53,54]. In particular, "molecular basket" sorbents have shown enhanced capture capacities due to synergistic effects that occur in the pores of the mesoporous support between adsorbent and aminopolymer [55]. Branched polyethyleneimine (PEI) has been well-established as a preferred aminopolymer for amino-adsorbent functionalization due to long polymer chains that promote van der Waal's adhesion and cyclic stability within adsorbent pores. PEI-functionalization has been the focus of considerable investigations due to its a convenient and scalable synthesis procedure that renders it practical for a myriad of $CO_2$ capture applications [51,52,55–57].

Many investigations focus on improvement of the equilibrium or dynamic adsorption capacities, characterizations of $CO_2$ transport properties is largely lacking. Understanding the mass transfer characteristics of $CO_2$ into and out of the adsorbent is critical to the overall efficiency and performance of the capture process at industrial scale mainly because it dictates the throughout and column size. This serves as the motivation of study of Paper II.

## 1.3 THE ZERO LENGTH COLUMN (ZLC) TECHNIQUE

All diffusion time constants reported in this work were acquired by the ZLC technique. First popularized by Eic and Ruthven [58] in 1988, this method, under well-defined conditions, removes extracrystalline resistances and heat transfer limitations that render traditional gravimetric and volumetric analyses unreliable in the derivation of

intracrystalline diffusivities [59–61]. The ZLC method has been thoroughly developed and studied over the years, and has been widely adopted in order to suit a number of different systems, including structured adsorbents [60,62], liquid systems [63], heat and mass effects [64–67], non-linear systems [61,68], and adsorption equilibria [69,70]. The ZLC technique was originally developed as a simple and versatile way for measure the intracrystalline diffusivities of zeolites, but has been further expanded uoon for other adsorbent materials, including MOFs [71], catalyst pellets [72], and aminoadsorbents [73]. A schematic diagram showing a typical ZLC system and ZLC column are shown in Figure 1.1.

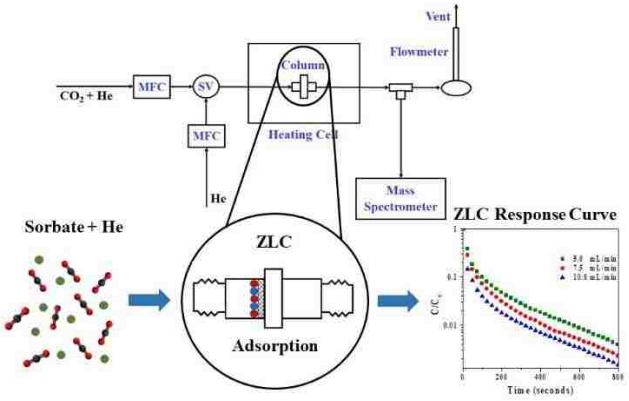


Figure 1.1. Schematic diagram of ZLC system.

In the ZLC method, a small amount of adsorbent (1-5 mg) is pre-equilibrated with a known amount of sorbate at a low enough partial pressure to remain within Henry's Law. The ZLC column consists of only a few adsorbent layers in order to be considered well-mixed. At some known time, the adsorbate is purged with a pure inert gas stream (such as He or Ar) and the effluent gas stream is dynamically monitored by a benchtop quadrouple mass spectrometer. Desorption, rather than adsorption, is monitored in order

to take advantage of enhanced detector sensitivities at the zero baseline. At high purge flow rates, desorption is controlled by diffusion out of the particle and the ZLC response curve will directly yield the diffusion time constant ($D_c/r_c^2$). At low purge rates, desorption is controlled by equilibrium between adsorbed and purge phase, and the response curve will yield the Henry's constant.

Several important criteria must first be recognized when utilizing the ZLC technique. First, when using this method to determine the diffusivity of the adsorbate, the $D_c/r_c^2$ must be significantly longer than the detector response-time. This limits the maximum $D_c/r_c^2$ that can be measured for a particular crystal size. Additionally, determining the diffusivity of weakly adsorbed species can be determined by using a larger sample size. However, larger sample sizes may introduce extracrystalline resistances to heat and mass transfer, reducing the accuracy of the measurements. This method can also break down for strongly adsorbed species, as it may be impossible to achieve purge rates that are high enough to exist in the diffusion-controlled regime. More detailed evaluations on the models utilized in determining the $D_c/r_c^2$ are presented in Paper I and II.

# PAPER

## I. DIFFUSION KINETICS OF ETHANE, ETHYLENE, AND THEIR BINARY MIXTURES IN ETHANE-SELECTIVE ADSORBENTS

Teresa Gelles, Shane Lawson, Harshul Thakkar, Fateme Rezaei

Department of Chemical & Biochemical Engineering, Missouri University of Science and Technology, 1101 N State Street, Rolla, MO, 65409

## ABSTRACT

Sorption kinetics of single component and binary mixtures of ethane and ethylene in powder and pellet samples of paraffin-selective adsorbents Ni(bdc)(ted)$_{0.5}$ and ZIF-7 were investigated by zero-length column (ZLC) technique for the purpose of olefin/paraffin separation. The intracrystalline diffusivities were determined at 25 °C and the results were compared in order to investigate the effects of coadsorption for binary gas mixtures and also diffusion in pelletized adsorbents. The diffusion time constants measured for ethane through ZIF-7 powder for single component and binary mixture were found to be $3.20 \times 10^{-3}$ and $2.77 \times 10^{-3}$ $s^{-1}$, respectively, whereas for Ni(bdc)(ted)$_{0.5}$ the measured values were $3.44 \times 10^{-3}$ and $3.14 \times 10^{-3}$ $s^{-1}$, respectively. Furthermore, diffusion of ethylene for both single component and binary mixture trials revealed the presence of surface resistance due to strong interactions between the C-C double bond and the external crystalline surface of the adsorbents. The findings of this study provide

novel kinetic characterizations on paraffin-selective adsorbents for the separation of ethane and ethylene.

# 1. INTRODUCTION

Light olefins such as ethylene and propylene are the most important chemical feedstocks used in petrochemical industry. Serving as the building blocks for production of many types of chemicals, plastics, polymers, and rubbers, light olefins are produced in larger quantities than any other kind of organic compounds (Eldridge, 1993). The production of olefins requires the separation of the olefin from its corresponding paraffin which is generally done by cryogenic distillation, which is extremely energy-intensive, requiring an energy demand of up to 30% of the total cost of the entire production process (U.S. Department of Energy, 2005)(Ren et al., 2006). Among alternative approaches, adsorption appears to be an attractive cost-effective method for olefin/paraffin separation (Baker, 2002; Chen et al., 2010; Eldridge, 1993; Jiang and Eić, 2003; Okamoto et al., 1999; Pinnau and Toy, 2001; Rungta et al., 2013; Safarik and Eldridge, 1998; Takht Ravanchi et al., 2009).

Traditionally, the investigated adsorbents for olefin/paraffin separations have preferential selectivity to olefins over paraffins due to the π-complexation formed between the olefin and adsorbent. Such adsorbents include zeolite 4A, CMS, and $Ag^+$ exchanged resins (Grande and Rodrigues, 2004; Padin et al., 2000; Padin and Yang, 2000; Rege et al., 1998). While this is an attractive mode of adsorption due to the strong bonds formed by the complexations, these bonds also result in significant energy

requirements upon regeneration. Additionally, the obtained olefin product has low recovery and purity rates (Kroon and Vega, 2009; Ruthven and Reyes, 2007). Recently, significant efforts have been put forth to develop paraffin-selective materials that preferentially adsorb paraffin over its olefin counterpart through weaker van der Waals forces than π-complexation, thus, imposing less energy requirements for adsorbent regeneration (Bloch et al., 2012; Gücüyener et al., 2010; Leclerc et al., 2011; Liang et al., 2016; Van Den Bergh et al., 2011)(Furukawa et al., 2013, 2010; James, 2003; Li et al., 2009; Zhou et al., 2012). Furthermore, with sufficiently high paraffin/olefin selectivity, it is possible to obtain the desired product with high purity and recovery rates directly from the adsorption step.

Among ethane-selective adsorbents, ZIF-7 and Ni(bdc)(ted)$_{0.5}$ (Ni-BT) were shown to exhibit high ethane adsorption capacity and ethane/ethylene selectivity. For instance at 25 °C and 1 bar, ethane uptakes of 3.21 and 5.11 mmol/g and ethane/ethylene selectivities of 1.9 – 11.8 and 1.2 – 2.0 were reported for ZIF-7 and Ni(bdc)(ted)$_{0.5}$, respectively (Gücüyener et al., 2010; Liang et al., 2016; Thakkar et al., 2018). Most recently, we formulated these two adsorbents into monolithic structures and studied their ethylene/ethane adsorption behavior (Thakkar et al., 2018). While adsorption behavior of ZIF-7 and Ni-BT has been investigated in detail (Gücüyener et al., 2010; Liang et al., 2016; Thakkar et al., 2018), the transport properties of ethane and ethylene in these materials is yet to be determined. In cyclic processes where adsorbent is saturated and regenerated, understanding the mass transfer of adsorbate molecules into and out of the adsorbent is critical and has lasting effects on the performance and efficiency of the process, especially when dealing with large industrial operations.

Adsorption kinetics can be measured by various microscopic and macroscopic techniques including frequency response (FR), interference microscopy (IFM), IR micro-imaging (IRM), and zero-length column (ZLC) technique (Kärger et al., 2012).

The ZLC technique, popularized by Eic and Ruthven (Eic and Ruthven, 1988), is a macroscopic technique that has been used extensively for the measurement of diffusion rates in porous adsorbents owing to its simplicity and accuracy (Brandani and Ruthven, 1996; Eic and Ruthven, 1988). According to the ZLC model, under well-defined conditions the extracrystalline resistances to heat and mass transfer are eliminated and thus the kinetics of sorption are completely controlled by intracrystalline diffusion. Traditionally, ZLC was modeled for crystalline diffusivities but has also been expanded to account for adsorbent pellets (Silva et al., 2012; Silva and Rodrigues, 1997, 1996), liquid systems (Brandani and Ruthven, 1995; Rodríguez et al., 1998), heat and mass effects (Brandani et al., 1998; Ruthven and Brandani, 2005; Silva et al., 2001), non-linear systems (Brandani, 1998; Brandani et al., 2000), and adsorption equilibria (Brandani et al., 2003; Brandani and Ruthven, 2003). In a recent investigation by Ruthven and Vidoni (Ruthven and Vidoni, 2012), the combined effect of surface resistance and internal diffusion was considered in sorption kinetics measurements and the new extended ZLC model was validated against experimental data for ethane diffusion in DDR zeolite. In another investigation, Brandani and co-workers (Hu et al., 2018) utilized the ZLC method to evaluate the stability of M/DOBDC $CO_2$ adsorbents in the presence of water, $SO_x$ and $NO_x$. The authors demonstrated the capability of the ZLC technique in providing quantitative information on deactivation of the adsorbents in the presence of flue gas impurities. Most recently, Rodrigues and co-workers (Seabra et al., 2019) applied the

ZLC technique to investigate the sorption kinetics of $CO_2$, $CH_4$ and $N_2$ in binderless 4A zeolite beads. The authors demonstrated the influence of intracrystalline and macropore diffusion in high-density zeolite beads.

In this work, we have expanded upon our previous investigations to measure the sorption kinetics of ethane and ethylene in two ethane-selective adsorbents, namely ZIF-7 and Ni-BT, in both powder and pellet forms utilizing the ZLC technique. Pure and binary gas mixtures were used to determine diffusion time constants for ethane and ethylene gases in powder and pellet samples. The estimated diffusion rates were then compared to determine the effects of gas composition and sorbent pelletization on sorption kinetics of ethane and ethylene.

## 2. EXPERIMENTAL SECTION

### 2.1 MATERIALS PREPARATION

ZIF-7 and Ni-BT powders (denoted as ZIF-7-P and Ni-BT-P, respectively) were synthesized according to the conventional hydrothermal synthesis methods outlined elsewhere (Chen et al., 2014; Liang et al., 2016; Thakkar et al., 2018). The ZIF-7 and Ni-BT pellets (denoted as ZIF-7-Pe and Ni-BT-Pe, respectively) were formed by mixing the powders with silica (85/15 weight ratio) and polyvinyl alcohol (80/20 weight ratio), respectively, followed by the addition of ethanol for the Ni-BT-Pe and methanol for the ZIF-7-Pe to make a viscous paste. The paste was then transferred to a syringe and small pellets were extruded from it. Finally, the pellets were dried at room temperature. Pellets of two different sizes were printed for each MOF material, the smaller are larger pellets

are denoted by a “1” and “2”, respectively. Table 1 summarizes the textural properties of the powders and pellets obtained by N2 physisorption measurements (Thakkar et al., 2018). The pellet porosity ( $\mathcal{E}_P$) was calculated from the ratio of the bulk density and skeletal density of the pellet. The skeletal density was first evaluated from the ratio of the densities of the MOF and binder and bulk density was then determined utilizing the pore volume of the pellet.

Table 1. Textural Properties of Powder and Pellet Samples.

| **Material** | **$S_{BET}$ ($m^2/g$)** | **$V_p$ ($cm^3/g$)** | **$d_p$ (nm)** | **$\varepsilon_P$** | **Pellet diameter (cm)** |
|---|---|---|---|---|---|
| ZIF-7-P | 16 | 0.05 | 1.6 | - | - |
| ZIF-7-Pe-1 | 40 | 0.13 | 10 | 0.16 | 0.15 |
| ZIF-7-Pe-2 | 40 | 0.13 | 10 | 0.16 | 0.30 |
| Ni-BT-P | 1800 | 0.88 | 1.2 | - | - |
| Ni-BT-Pe-1 | 1300 | 0.66 | 1.5 | 0.52 | 0.07 |
| Ni-BT-Pe-2 | 1300 | 0.66 | 1.5 | 0.52 | 0.20 |

## 2.2 ADSORPTION EQUILIBRIUM MEASUREMENTS

The adsorption isotherms of pure $C_2H_6$ and $C_2H_4$ gases were obtained at room temperature over both powder and pellet samples using a volumetric gas analyzer (3Flex, Micromeritics). The samples were first degassed at 150 °C under vacuum for 8 h to remove any pre-adsorbed gases or humidity (Thakkar et al., 2018) prior to analysis.

## 2.3 ZLC EXPERIMENTS

The ZLC apparatus used for kinetic measurements is depicted in Figure 1. It consists of two sections: the gas preparation section and the ZLC column and detection section. In the gas preparation section, ultra-high purity helium used as the inert gas carrier enters the system through two streams (denoted at stream 1 and 2) which are connected by a switching valve. Stream 1 is fed into a mixing cell where it is mixed with either pure $C_2H_4$ or $C_2H_6$ or a pure equimolar mixture of both in order to obtain the desired concentration of the sorbates. Upon mixing, the gas mixture is then passed through a mass flow controller (MFC) to stream 3. Streams 2 and 3 are fed through a three-way switching valve that controls which line enters the ZLC column. All gas streams within the system are controlled by MFCs. The ZLC column consists of a 1/8" Swagelok union with a wire mesh loaded inside to serve as the adsorbent bed. The column is housed inside of a heating cell consisting of HTSAmptek flexible heating tape controlled by an Omega Benchtop controller. At the outlet of the ZLC column, the gas concentration is directly monitored by a BELMass benchtop quadrupole mass spectrometer. Following detection, the effluent gas stream vents through a soap-bubble flowmeter, which allows for both the monitoring of flow rates and the calibration of the MFCs.

For a typical run, a small amount of sample (between 3-5 mg) was loaded inside of the 1/8" Swagelok union and evenly dispersed on the mesh bed. Prior to experiments, both the ZIF-7 and Ni-BT samples were heated to 150 °C and purged with a pure He stream at 2 mL/min for 6 h in order to remove any moisture or any remaining $C_2H_4$ or $C_2H_6$ that may have been introduced from previous run.

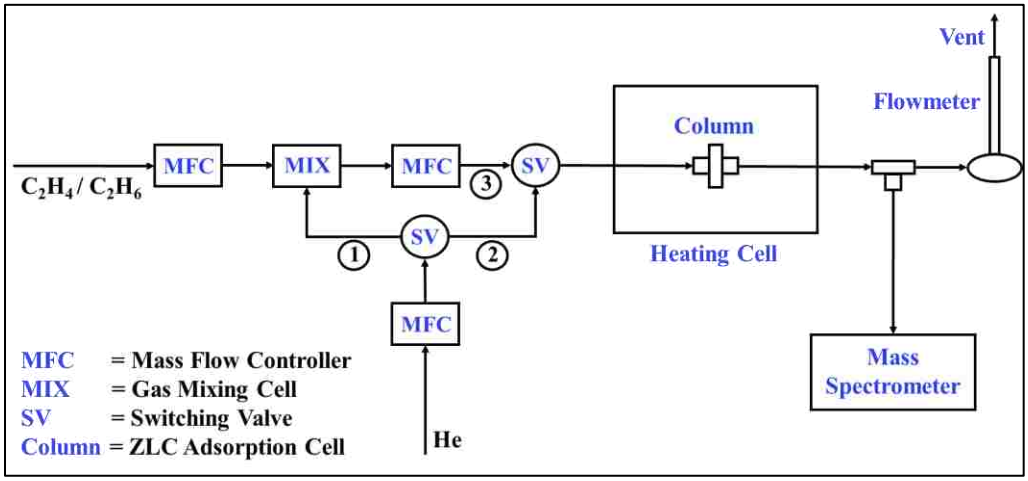


Figure 1. Schematic diagram of ZLC apparatus.

Before time zero, the pre-mixed carrier gas was introduced into the adsorption cell at 2 mL/min and the adsorbent sample was equilibrated with the carrier gas for 1- 2 h. The sorbate concentration was maintained at partial pressures between 0.01 – 0.025 bar in order to remain in the linear region of Henry's Law. Adsorption was continuously monitored via the mass spectrometer in order to ensure that the sample was completely saturated with sorbate prior to the ZLC measurements. The equilibrium time is dependent upon Henry's constant, and therefore varied for both the adsorbent and sorbate being tested. Upon complete saturation, at time zero, the valves were switched, and the cell was exposed to the pure He purge stream. The concentration of the desorbed gases was monitored in the effluent stream for a sufficiently long enough time to ensure complete desorption from the adsorbent.

Prior to ZLC testing, blank runs were performed in order to characterize the dead volume ($V_g$) of the system. $V_g$ represents the sum of the volumes of gas in the cell and piping between the switching valve and detector. For weakly adsorbed species, the determination of $V_g$ is critical and must be accounted for upon analysis of the desorption

curves. Blank testing was also performed in order to determine the optimal operating parameters for the mass spectrometer. The mass spectra for $C_2H_4$ and $C_2H_6$ overlap, therefore, extensive blank testing was done at a range of atomic mass units (amus) in order to find the corresponding amus for $C_2H_4$ and $C_2H_6$ that yielded the strongest individual signals. Figure S1 (Supporting Information) provides an example of the desorption signal acquired for both single components of $C_2H_4$ and $C_2H_6$ in He, as well as a binary $C_2H_4/C_2H_6$ run over ZIF-7-P. Clearly, distinct signals for $C_2H_4$ and $C_2H_6$ can be observed.

## 3. ZLC THEORETICAL MODEL

### 3.1 MICROPORE AND MACROPORE MODEL

In a typical ZLC experiment, a bed of adsorbent is saturated with the sorbate as either a single component or binary mixture species in an inert carrier (such as He) at low concentrations to reside within the linear region of Henry's Law. It is assumed that the ZLC cell is well mixed, with the fluid and adsorbed species at equilibrium with one another at the particle surface. At time zero, pure He (free of sorbate) is used to purge the ZLC and the resulting desorption curve is measured as a function of time. The desorption response curve is derived from Fick's law of diffusion and is modeled as:

$$\frac{C}{C_0} = \sum_{n=1}^{\infty} \frac{2L}{\left[\beta_n^2 + L(L-1)\right]} \exp\left(\frac{-\beta_n^2 D_c}{r_c^2} t\right) \tag{1}$$

For a linear system with uniform spherical particles of radius $r_c$, the diffusion parameters can be extracted from the desorption curves at long times. Only the first summation becomes significant and Fick's law can be reduced to the following equation:

$$\ln\left(\frac{C}{C_0}\right)=\ln\left(\frac{2L}{\beta_1^2+L(L-1)}\right)-\frac{\beta_1^2 D_c}{r_c^2}t \tag{2}$$

where $\beta_1$ is the root of the transcendental equation:

$$\beta_1\cot(\beta_1)+L-1=0 \tag{3}$$

and $L$ is a dimensionless model parameter given by:

$$L=\frac{1}{3}\frac{F}{KV_s}\frac{r_c^2}{D_c} \tag{4}$$

where $F$ is the purge flow rate, $V_s$ is the sample volume, $K$ is the dimensionless Henry's Law constant, and $D_c$ is the crystalline diffusivity. When the purge flow rate is sufficiently large such that $L > 10$, the desorption rate out of the particle is completely controlled by diffusion and $\beta_1 \to \pi$. Thus, a plot of $\ln(C/C_0)$ versus time will yield a long-time asymptote with a slope of $\pi^2 D_c/r_c^2$, from which the diffusion time constant, $D_c/r_c^2$ is easily determined. Altering the purge flow rate within the diffusion-controlled regime

may change the intercept of the curve, but the slope should remain constant. The accuracy and reliability of the long-time asymptotic analysis has been detailed in many previous studies (Brandani and Ruthven, 1996; Eic and Ruthven, 1988; Kärger et al., 2012). However, for weakly adsorbed species, it is often necessary to account for fluid phase hold-up in the system. Therefore, the model described by eq. 2 has been expanded to include extracrystalline hold-up and is represented as (Brandani, 1996; Brandani and Ruthven, 1996):

$$\ln\left(\frac{C}{C_0}\right)=\ln\left(\frac{2L}{\beta_1^2+(L-1-\gamma\beta_1^2)+L-1+\gamma\beta_1^2}\right)-\frac{\beta_1^2 D_c}{r_c^2}t \tag{5}$$

$$\beta_1\cot(\beta_1)+L-1-\gamma\beta_1^2=0 \tag{6}$$

$$\gamma=\frac{V_g}{3KV_s} \tag{7}$$

Clearly, as $\gamma \to 0$ eq. 5 and 6 revert to eq. 2 and 3. Previous studies have shown that for $\gamma < 1$, the difference between the two models becomes negligible. At low flow rates such that $L << 1$, the regime controlling desorption shifts from diffusion to equilibrium control and eq. 2 reduces to a simple exponential form (Brandani et al., 2003):

$$\ln\left(\frac{C}{C_0}\right)=-\frac{F}{KV_s}t \tag{8}$$

In the regime of equilibrium control, diffusion characterization cannot be determined with any sufficient accuracy. The above model is only valid for measuring intracrystalline diffusivities. If it is, however, desired to measure the diffusivities of pellets, then macropore diffusion must be taken into account and the previous equations must be modified slightly to account for the effects of intercrystalline (macropore) diffusion (Brandani, 1996; Ruthven and Xu, 1993; Silva and Rodrigues, 1996) as follows:

$$\ln\left(\frac{C}{C_0}\right)=\ln\left(\frac{2L}{\beta_1^2+L(L-1)}\right)-\beta_1^2\frac{D_P}{R_P^2(1+K_P)}t \tag{9}$$

$$L=\frac{1}{3}\frac{F}{V_s}\frac{R_P^2}{D_P} \tag{10}$$

$$K_P=\frac{\rho_P K}{\varepsilon_P} \tag{11}$$

where $R_P$ is the pellet radius, $D_P$ is the macropore diffusivity, $\rho_P$ is the pellet density, $K_P$ is the pellet dimensionless Henry's Law constant, and $\varepsilon_P$ is the pellet porosity. A plot of *ln(C/C₀)* versus time will yield a long-time asymptote with a slope of $\pi^2 D_P / R_P^2(1+K_P)$, from which the macropore diffusion time constant, $D_P / R_P^2$, is easily determined.

In order to correctly discern between the importance of micropore or macropore diffusion within the pellet samples, it is necessary to test for diffusivity in pellets of different sizes but with the same crystal size (Ahn et al., 2004). Considering the crystal radius is much smaller than radius of the pellet, differences in diffusion lengths between crystal and pellet are comparable to differences of diffusivities. Therefore, the diffusion time constant emerges as an important evaluator of the overall importance of micropore and macropore diffusion. If intracrystalline diffusion is the controlling step for mass transfer out of the pellet, the diffusion time constant will not change with pellet size. If macropore diffusion is the controlling step, the diffusion time constant of the smaller pellet would correspond to the diffusion time constant of the large pellet multiplied by the ratio of the square of the pellet radiuses. If the diffusion time constant of the smaller pellet is not as great as the resultant product, then both macropore and micropore diffusion contributes to the overall diffusion rate (Ahn et al., 2004; Ruthven and Xu, 1993).

## 3.2 EXTENDED SURFACE RESISTANCE MODEL

The above approaches assume that desorption is controlled entirely by micropore diffusion out of the cell (or macropore diffusion in the case of pellets). However, many recent studies have shown that there are cases when desorption can be controlled by surface resistances to mass transfer rather than by diffusion alone (Ruthven and Brandani, 2005; Ruthven and Vidoni, 2012; Vidoni, 2011). In cases of surface resistance control, eq. 2 will remain unchanged except that $L$ will be replaced by $L'$ according to the following expression:

$$\frac{1}{L'}=\frac{1}{L}+\frac{D_c}{kr_c}=\frac{3KV_s}{F}\left(\frac{D_c}{r_c^2}\right)+\frac{D_c}{kr_c} \tag{12}$$

where $k$ is the surface mass transfer coefficient and $L'$ is the apparent $L$. Note that in the case of no surface resistance, $L' = L$. However, when surface resistance is present, if $L' > 10$, diffusion is not affected by surface resistance and the slope of the long-time asymptote can be represented as $\pi^2 D_c / r_c^2$ and the intercept of the asymptote will yield $L'$, from which eq. 12 can be used to determine $L$. When $L' < 10$ the diffusion time constant derived from the long-time asymptote is not independent of flow rate and may be affected by the presence of surface resistance (Kärger et al., 2012).

From eq. 12, a plot of $1/L'$ versus $1/F$ should yield a straight line with slope $3KV_s D_c / Fr_c^2$ and intercept $D_c / kr_c$. The intercept measures the relative importance of surface resistance. An intercept of zero means that there is no significant surface resistance while a large intercept suggests surface resistance control and the calculated diffusion time constant should be considered unaffected only if $L' > 10$ (Kärger et al., 2012; Ruthven and Vidoni, 2012; Vidoni and Ruthven, 2012). Further detailed analyses of the ZLC theory for both micropore and macropore diffusion, as well as surface resistance have been thoroughly described elsewhere (Brandani, 1996; Brandani and Ruthven, 1996; Eic and Ruthven, 1988; Ruthven and Vidoni, 2012; Silva and Rodrigues, 1997, 1996; Vidoni and Ruthven, 2012).

# 4. RESULTS AND DISCUSSION

## 4.1 ADSORPTION ISOTHERMS AND HENRY'S CONSTANTS

The adsorption isotherms of $C_2H_4$ and $C_2H_6$ for both ZIF-7 and Ni-BT were obtained at 25 °C and are shown in Figure 2. The ZIF-7 isotherms (Figure 2a) show a steep uptake in adsorption for both $C_2H_4$ and $C_2H_6$ corresponding to gate opening phenomenon, typical of this adsorbent (Van Den Bergh et al., 2011). The Dual-Site Langmuir-Freundlich adsorption model (DSLF) was used to best fit these S-shaped isotherms. The Ni-BT isotherms (Figure 2b) for both $C_2H_4$ and $C_2H_6$ are essentially linear and are well represented by the traditional Langmuir isotherm model. Overall, the pellets exhibit comparative uptakes to their powder counterparts. Compared to the powdered forms, the pellet capacities are proportional to their MOF loading (85 wt. % and 80 wt. % for ZIF-7 and Ni-BT, respectively).

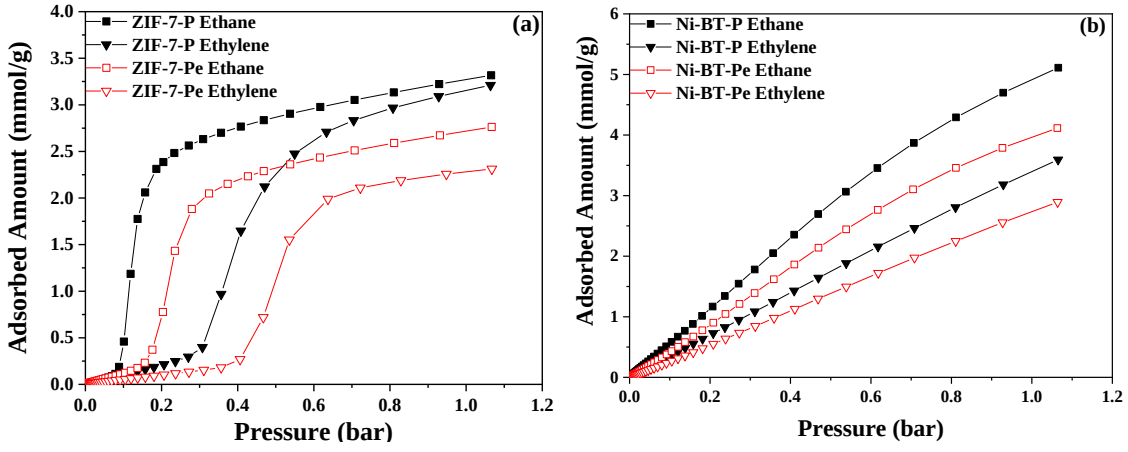


Figure 2. Ethane and ethylene adsorption isotherms of (a) ZIF-7-P and ZIF-7-Pe and (b) Ni-BT-P and Ni-BT-Pe at 1 bar and 25 °C (Thakkar et al., 2018).

From the isotherms, at regions of low loading, the Henry's constants (*H*) were calculated. The experimental data was plotted according to a *Virial* plot:

$$\ln\left(\frac{P}{q}\right) = A_1 q - \ln H \tag{13}$$

where *P* is pressure, *q* is the amount adsorbed and $A_1$ is a virial coefficient. From the plot of ln(*p*/*q*) versus *q*, as *q* and *P* approach zero, the reciprocal of Henry's constant was determined. From Henry's constant, the temperature-dependent dimensionless Henry's law constant (*K*) was directly determined. Both *H* and *K* values are outlined in Table 2.

Table 2. Henry's constant (*H*) and dimensionless Henry's law constant (*K*) for ZIF-7 and Ni-BT powders and pellets.

| **Material** | ***H* (mmol/gbar)** | ***K*** |
|---|---|---|
| **ZIF-7-P** | | |
| **$C_2H_4$** | 1.04 | 26 |
| **$C_2H_6$** | 1.13 | 28 |
| **ZIF-7-Pe** | | |
| **$C_2H_4$** | 0.63 | 15 |
| **$C_2H_6$** | 1.07 | 26 |
| **Ni-BT-P** | | |
| **$C_2H_4$** | 3.56 | 88 |
| **$C_2H_6$** | 5.72 | 142 |
| **Ni-BT-Pe** | | |
| **$C_2H_4$** | 2.55 | 63 |
| **$C_2H_6$** | 4.09 | 102 |

## 4.2 DIFFUSION KINETICS OF $C_2H_4$ AND $C_2H_6$ IN ZIF-7

The ZLC measurements for single and binary component gas mixtures of $C_2H_4$ and $C_2H_6$ were performed on ZIF-7-P and ZIF-7-Pe. The diffusivity values ($D_c/r_c^2$) were determined from various measurements at different purge flow rates. The purge flow rates of $C_2H_6$ for the ZIF-7-P samples varied from 5.0 – 16.5 mL/min, whereas the purge flow rates of $C_2H_4$ for these samples varied from 10.5 – 30 mL/min. The ZIF-7-Pe samples were purged at flow rates ranging 16.5 – 30 mL/min. Higher purge rates were required for the pellets in order to remain in the diffusion-controlled regime. Referring to eq. 4, pellet sizing resulted in larger $V_s$ values, requiring larger purge flow rates for diffusion control. Additionally, due to the low Henry's law constants (outlined in Table 2), accumulation in the fluid phase could not be neglected and the desorption data was extracted and evaluated from the long-time region using eq. 5-7 and is represented in Tables 2-3. Blank testing found $V_g$ = 0.35 mL.

As can be clearly observed in in Figure 3, the slopes of the long-time asymptotes measured at different flow rates for $C_2H_6$ for both single and binary component gas mixtures for ZIF-7-P and ZIF-7-Pe are essentially equal and independent of flow rate, indicating that the measurements were taken in the region of complete diffusion control ($L$ > 10). Kinetic control was further confirmed via the consistency check $C/C_0$ *vs. Ft* (Figure S2, Supporting Information) (Brandani, 2016). Therefore, using eq. 5 and allowing $\sqrt{\beta_1} \to \pi$, the diffusion time constants were easily calculated and are presented in Table 3. The $L$ parameter was determined from the $C/C_0$ intercept of the long-time asymptote.

The curves shown in Figure 3 have been fit against the ZLC model equation (eq. 1) in order to demonstrate the degree of fit between the experimental curves and theoretical model. Slight deviations between data and the model in the initial desorption region may be due to dead-volume effects that were not fully captured by the theoretical model. However, there is excellent agreement between the theoretical and experimental curves in the long-time region, demonstrating accurate $D_c/r_c^2$ values have been interpolated at long times.

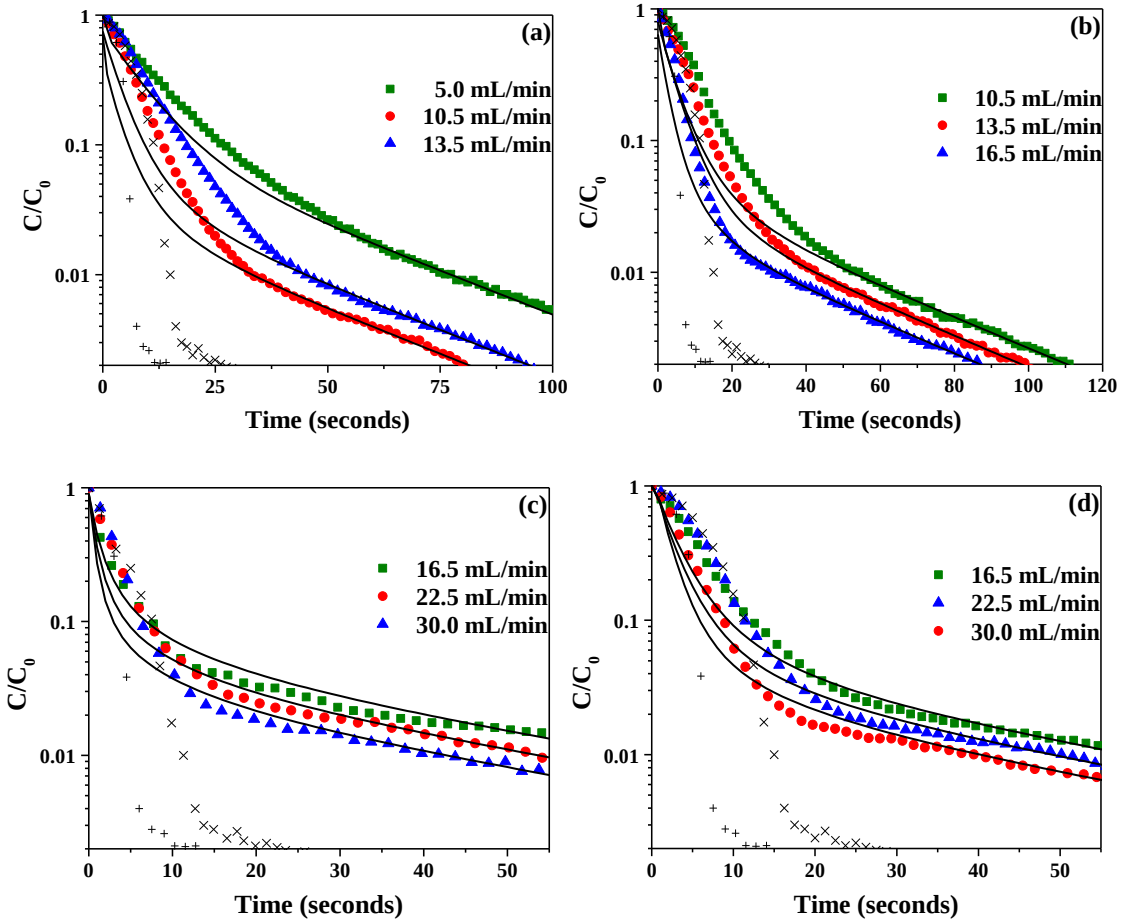


Figure 3. ZLC desorption curves of $C_2H_6$ at 25 °C for (a) ZIF-7-P single component system, (b) ZIF-7-P binary system, (c) ZIF-7-Pe-1 binary system, and (d) ZIF-7-Pe-2 binary system fit against ZLC model curves and blank responses: (×) at 5.0 mL/min and (+) at 10.5 mL/min.

$C_2H_6$ diffused quickly through ZIF-7-P in both single and binary component runs, where $C/C_0$ = 0.001 of the desorption curve was reached in under 2 min. These fast kinetics agree with work done by Gucuyener et al. (Gücüyener et al., 2010), who studied the desorption behavior of $C_2H_6$ and $C_2H_4$ in ZIF-7 powder. In reference to the sharp step in the adsorption isotherms for ZIF-7 shown in Figure 2a, as the partial pressure of $C_2H_6$ in the gas stream decreases, the kinetics of desorption are accelerated, resulting in a desorption step that occurs on the same time scale as its adsorption step. This is relatively uncommon for many adsorbent materials which generally favor faster adsorption and slower desorption kinetics.

The diffusion time constants of $C_2H_6$ in single and binary component mixtures for ZIF-7-P were found to be $3.20 \times 10^{-3}$ and $2.77 \times 10^{-3}$ $s^{-1}$, respectively. The diffusivity of $C_2H_6$ dropped by about 14% between single and binary gas trials, indicating that the diffusion of $C_2H_6$ is slowed in the presence of $C_2H_4$. From our investigations of the diffusivity of $C_2H_4$ in ZIF-7-P, shown in Table 4, it was found that $C_2H_4$ moves more slowly through the ZIF-7 channels. Therefore, it is expected that the $C_2H_4$ molecules would act as barriers to the motion of the co-adsorbed $C_2H_6$ molecules within the pores, resulting in slower diffusion rates for $C_2H_6$. The binary diffusion of $C_2H_6$ in both ZIF-7-Pe-1 and ZIF-7-Pe-2 was found to be $2.68 \times 10^{-3}$ $s^{-1}$. The diffusion of $C_2H_6$ in the presence of $C_2H_4$ is slightly lessened by about 2% between powder and pellet samples, indicating that the diffusion of $C_2H_6$ through ZIF-7 in a binary gas mixture is not significantly affected by intercrystalline (macropore) resistances in the pellet. Additionally, due to the consistency in the diffusion time constants obtained at different pellet sizes, resistance to mass transfer is occurring at the crystalline level and that

intracrystalline diffusion is controlling diffusion of $C_2H_6$ out of the pellets. For ZLC experiments, Brandani and co-workers have both theoretically and experimentally demonstrated that diffusion is independent of sorbate loading and corresponds with the limiting transport diffusivity (Brandani, 1998; Brandani et al., 2000). Therefore, even at low binary mixture concentrations (0.025 bar), the competing behavior of $C_2H_4$ and $C_2H_6$ outlined above can be thoroughly characterized.

Table 3. Diffusivity data for $C_2H_6$ in ZIF-7-P and ZIF-7-Pe.

| **Material** | **Sorbate** | **Flow Rate (mL/min)** | **-Slope × $10^2$ ($s^{-1}$)** | ***$D_c/r_c^2$* × $10^3$ ($s^{-1}$)** | ***L*** |
|---|---|---|---|---|---|
| **ZIF-7-P** | $C_2H_6$ | 5.0 | 3.12 | 3.16 | 31 |
| | | 10.5 | 3.17 | 3.21 | 64 |
| | | 13.5 | 3.18 | 3.22 | 88 |
| **Avg.** | | | | 3.20 | |
| **ZIF-7-P** | $C_2H_6$ / $C_2H_4$ | 10.5 | 2.70 | 2.74 | 65 |
| | | 13.5 | 2.76 | 2.80 | 84 |
| | | 16.5 | 2.73 | 2.77 | 97 |
| **Avg.** | | | | 2.77 | |
| **ZIF-7-Pe-1** | $C_2H_6$ / $C_2H_4$ | 16.5 | 2.63 | 2.67 | 37 |
| | | 22.5 | 2.64 | 2.68 | 49 |
| | | 30.0 | 2.62 | 2.66 | 66 |
| Avg. | | | | 2.67 | |
| **ZIF-7-Pe-2** | $C_2H_6$ / $C_2H_4$ | 16.5 | 2.64 | 2.68 | 53 |
| | | 22.5 | 2.62 | 2.66 | 66 |
| | | 30.0 | 2.65 | 2.70 | 82 |
| **Avg.** | | | | 2.68 | |

The desorption (Figure 4a-c) of $C_2H_4$ through ZIF-7-P and ZIF-7-Pe for both single and binary gas mixtures revealed consistent but anomalously shaped response curves. Traditionally, the ZLC model assumes that desorption is completely controlled by diffusion effects. However, some recent studies have revealed that there can exist significant mass transfer resistances at the surface of adsorbent crystals, causing sorption rates to be controlled by a combination of intracrystalline diffusion and surface resistance. This has been confirmed to occur at the surface of zeolites (Heinke et al., 2007; Kortunov et al., 2005) but has not before been reported for ZIF-7. A detailed analysis of the desorption curves shown in Figure 4 suggests the intrusion of significant mass transfer resistances for ZIF-7-P and ZIF-7-Pe, and eq. 12 was used to better describe the desorption response. The potential influence of heat effects was also investigated and was found to be negligible utilizing the theoretical model introduced by Brandani et al. (Brandani et al., 1998). The ZLC model fit against the response curves in Figure 4 models the data relatively well, despite observed fluctuations.

Vidoni and Ruthven (Vidoni and Ruthven, 2012) reported mass transfer resistances occurring with the diffusion of $C_2H_4$ in DDR zeolites and also reported issues with obtaining consistent data between replicate measurements. The high surface resistance is best explained by the intrusion of CH-H and CH-$\pi$ interactions at the external surface of the ZIF between its $Zn^{+2}$ metal ions and the $C_2H_4$ double bonds. Electrons become shared between the *d* orbital of the $Zn^{+2}$ and the empty $\pi^*$ orbital of $C_2H_4$, resulting in strong external adsorption on the surface of the ZIF-7 at pore entrances (Jorge et al., 2010; Lamia et al., 2009). This results in the partial obstruction of the pore entrances, resulting in a higher energy barrier at the crystalline surface as sorbent is

blocked from diffusion out of the pores (Kärger et al., 2012). For ZIF-7, the strong external adsorption also causes significant geometric distortion to its cage entrances, resulting in further blockage (Van Den Bergh et al., 2011).

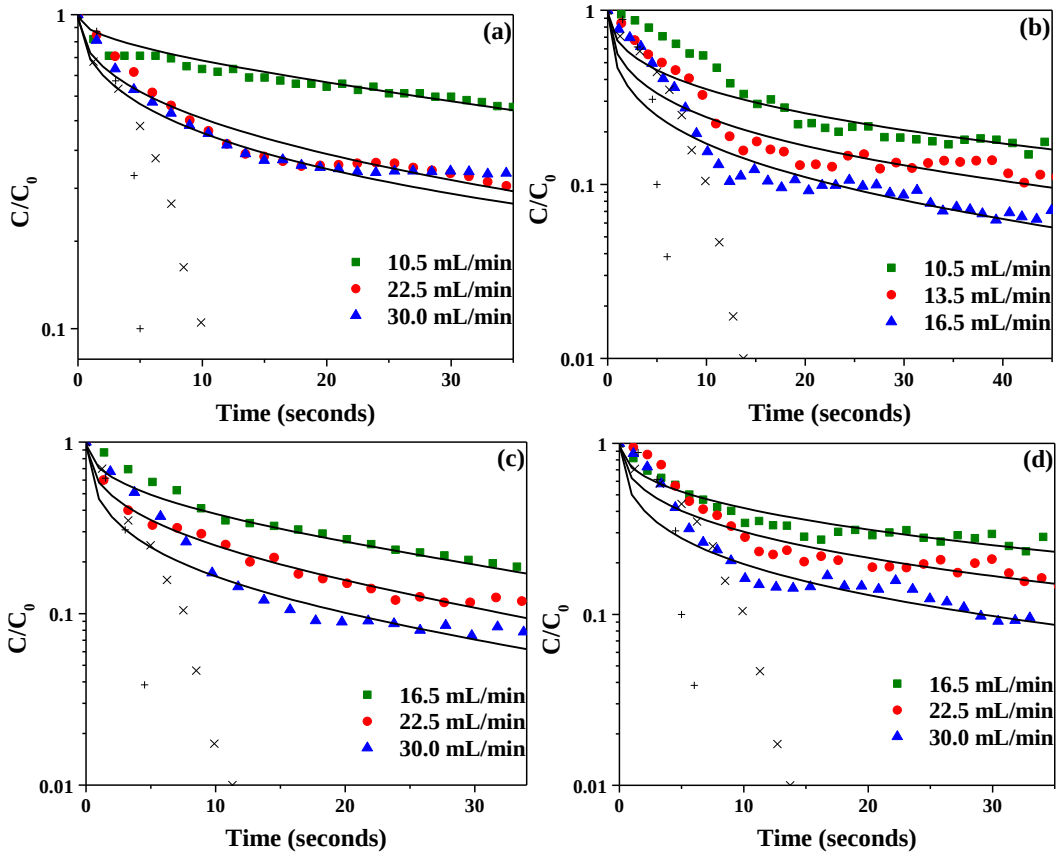


Figure 4. ZLC desorption curves for $C_2H_4$ at 25 °C for (a) ZIF-7-P single component (b) ZIF-7-P binary system (c) ZIF-7-Pe-1 binary system, and (d) ZIF-7-Pe-2 binary system fit against ZLC model curves and blank responses: (×) at 5.0 and (+) at 10.5 mL/min.

The $L'$ parameter was extrapolated from the intercept of the $C/C_0$ axis and $D_c/r_c^2$ was determined from the slope of the long-time region. Both parameters are listed in Table 4. Due to the low $L'$ values, the system could not be assumed to be in the diffusion-controlled regime and $\beta_1$ had to be determined. Additionally, curves

overlapping was displayed when plotting $C/C_0$ *vs. Ft* for consistency check (Figure S3, Supporting Information) which implied an equilibrium-controlled process and a deviation of response curves indicative of kinetic control, demonstrating that no obvious conclusion regarding system control can be drawn from the data. In order to determine the magnitude of surface resistance present, utilizing eq. 12, $1/L'$ versus $1/F$ was plotted and $D_c/kr_c$ was derived from the intercept (Figures S6 and S7, Supporting Information). For single and binary component runs, ZIF-7-P exhibited $D_c/kr_c$ values of 0.19 and 0.03, respectively, whereas ZIF-7-Pe-1 and ZIF-7-Pe-2 yielded $D_c/kr_c$ values of 0.08 and 0.04, respectively. The single component $C_2H_4$ diffusion exhibited the highest surface resistance. Moreover, for both ZIF-7-P and ZIF-7-Pe samples, the binary desorption curves for $C_2H_4$ in the presence of $C_2H_6$ also demonstrated the presence of mass transfer resistances. However, for the binary trials we can see that the magnitude of surface resistance is less significant. This can best be explained by the presence of co-adsorbed $C_2H_6$ on the surface of the ZIF-7 crystals. The $C_2H_6$ occupied adsorption sites that had previously belonged to $C_2H_4$ in the single component trials, resulting in less pore blockage and geometric distortion of the ZIF-7 lattice. Interestingly, the surface resistance of ZIF-7-P for single component trials was almost 5 times greater than the ZIF-7-Pe. This is best described by the larger pore volume and pore diameter of the pellet (Table 1), which enabled greater accessibility and motion of $C_2H_4$ within the pores.

When compared to the $D_c/kr_c$ values of ZIF-7-P for single and binary component trials and of ZIF-7-Pe for $C_2H_6$ (0.0002, 0.0009, and 0.004, respectively), it can be concluded that surface resistance is insignificant for $C_2H_6$ but significant for $C_2H_4$.

Considering both the low $L'$ and high $D_c/kr_c$ values, the diffusivities estimated in Table 4 should be read with caution.

Table 4. Diffusivity data for $C_2H_4$ in ZIF-7-P and ZIF-7-Pe.

| **Material** | **Sorbate** | **Flow Rate (mL/min)** | **-Slope × $10^2$ ($s^{-1}$)** | **$D_c/r_c^2$ × $10^3$ ($s^{-1}$)** | **$\beta_1$** | **$L'$** | **$L$** |
|---|---|---|---|---|---|---|---|
| **ZIF-7-P** | $C_2H_4$ | 10.5 | 1.26 | 4.36* | 1.7 | 1.2 | 1.6 |
| | | 22.5 | 1.07 | 1.71 | 2.5 | 4.4 | 27 |
| | | 30.0 | 1.02 | 1.01 | 2.5 | 5.1 | 160 |
| **Avg.** | | | | 1.35 | | | |
| **ZIF-7-P** | $C_2H_4/C_2H_6$ | 10.5 | 1.03 | 1.37 | 2.7 | 7.6 | 9.8 |
| | | 13.5 | 1.27 | 1.57 | 2.8 | 11 | 16 |
| | | 16.5 | 1.72 | 1.81 | 3.1 | 14 | 25 |
| **Avg.** | | | | 1.58 | | | |
| **ZIF-7-Pe-1** | $C_2H_4/C_2H_6$ | 16.5 | 2.84 | 4.97 | 2.4 | 3.9 | 5.7 |
| | | 22.5 | 2.86 | 3.84 | 2.9 | 7.2 | 15 |
| | | 30.0 | 2.25 | 3.39 | 2.9 | 11 | 91 |
| **Avg.** | | | | 4.07 | | | |
| **ZIF-7-Pe-2** | $C_2H_4/C_2H_6$ | 16.5 | 1.20 | 1.77 | 2.6 | 5.0 | 6.3 |
| | | 22.5 | 1.32 | 1.77 | 2.7 | 7.8 | 11 |
| | | 30.0 | 1.50 | 1.83 | 2.9 | 8.8 | 14 |
| **Avg.** | | | | 1.80 | | | |

**Value excluded from Avg.*

Larger flow rates were required to derive a consistent diffusion time constant for ZIF-7-P. The diffusion time constants, $D_c/r_c^2$, for $C_2H_4$ for single and binary gas runs were found to be $1.35 \times 10^{-3}$ $s^{-1}$ and $1.58 \times 10^{-3}$ $s^{-1}$, respectively. The diffusion rate slightly increased for $C_2H_4$ in the presence of $C_2H_6$ for both powder and pellet samples.

This could be attributed to the interference of surface resistances in the pellet. Overall however, the diffusivity values were relatively consistent between both single and binary runs. Investigations of the diffusivity relationships in different binary gas systems have revealed that while the diffusion of faster moving species ($C_2H_6$) are greatly reduced in the presence of slower diffusing species ($C_2H_4$), the transport of slower species are not considerably affected by the faster species (Jiang and Eić, 2003; Kärger et al., 2012). Our results show a general agreement with these findings. In the work conducted by Gucuyener et al. (Gücüyener et al., 2010), the authors reported that $C_2H_4$ completely desorbs from ZIF-7 more quickly than $C_2H_6$. This was also observed in our findings. Following the region of general linearity shown in the desorption profiles in Figure 4, the concentration ratio of $C_2H_4$ steeply drops to 0 before 100 seconds after the start of experiment for all three trials.

The diffusion time constant derived from ZIF-7-Pe-1 is over twice as fast as the rate derived for the larger pellet, ZIF-7-Pe-2, indicating the presence of macropore diffusional resistances. Evaluation of the diffusion time constant multiplied by the square of the pellet ratios revealed to be greater than the time constant of ZIF-7-Pe-1. This means that for a $C_2H_4$ and ZIF-7-Pe system, both micropore and macropore diffusion contribute to the overall diffusion rate of the pellet.

### 4.3 DIFFUSION KINETICS OF $C_2H_4$ AND $C_2H_6$ IN NI-BT

ZLC measurements for the single and binary component diffusion of $C_2H_4$ and $C_2H_6$ were also carried out over Ni-BT-P and Ni-BT-Pe samples. The purge flow rates used for measuring diffusivity values of $C_2H_6$ ranged from 10.5 – 16.5 mL/min, whereas

the purge rates used for measuring $C_2H_4$ ranged from 10.5 – 22.5 mL/min. Moreover, the Ni-BT-Pe was purged at higher flow rates ranging 22.5 – 30 mL/min for both $C_2H_6$ and $C_2H_4$ trials. Eq. 7 was utilized in order to ascertain the importance of fluid-phase hold-up. $\gamma < 0.1$ was obtained for both $C_2H_6$ and $C_2H_4$ trials, and desorption data was evaluated using eq. 2-4. Kinetic control was confirmed via the consistency check $C/C_0$ *vs.* $Ft$ (Figure S4, Supporting Information).

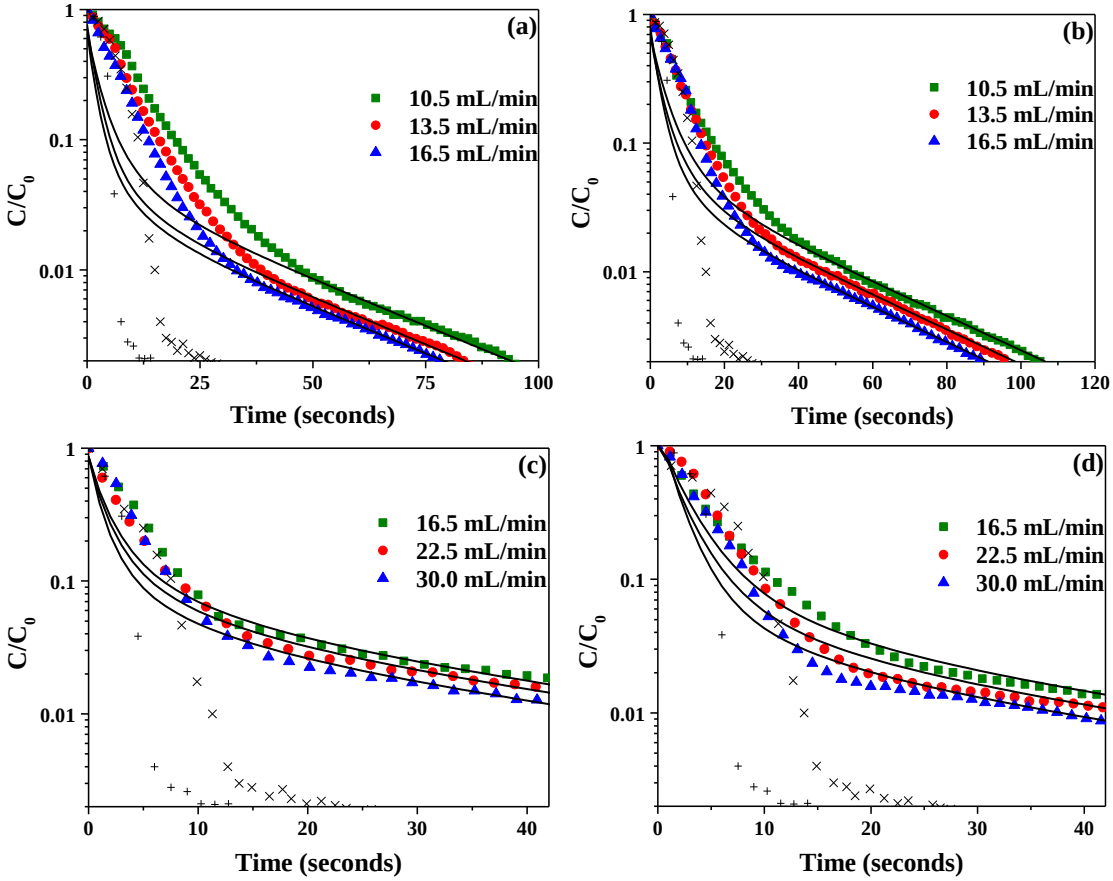


Figure 5. ZLC desorption curves for $C_2H_6$ at 25 °C for (a) Ni-BT-P single component (b) Ni-BT-P binary system (c) Ni-BT-Pe-1 binary system, and (d) Ni-BT-Pe-2 binary system fit against ZLC model curves and blank responses: (×) at 5.0 mL/min and (+) at 10.5 mL/min.

The obtained desorption curves for Ni-BT samples are illustrated in Figure 5 and the corresponding diffusivity data for $C_2H_6$ and $C_2H_4$ are provided in Table 4 and Table 5, respectively. The ZLC model fit against the experimental data in Figure 5 shows excellent agreement in the long-time region for all curves. From Figure 5, it is evident that the slopes of $C_2H_6$ diffusion curves are equal for both Ni-BT-P and Ni-BT-Pe, confirming the existence of a diffusion-control regime. For the Ni-BT-P trials, $C/C_0$ = 0.001 was reached on the desorption curve in under 2 min for both single and binary gas trials, implying that the rate of desorption is on the same time scale as the rate of adsorption. The single component and binary gas mixtures for $C_2H_6$ in Ni-BT-P were found to have diffusion time constants of $3.34 \times 10^{-3}$ and $3.14 \times 10^{-3}$ $s^{-1}$, respectively. We observed a decrease of about 6% in the $D_c/r_c^2$ between single component and binary trials, which implied that the diffusion of $C_2H_6$ is slowed in the presence of $C_2H_4$. Investigating the diffusivity time constants presented in Table 6 revealed that $C_2H_4$ moves more slowly through the Ni-BT-P channels and therefore would act as a barrier of transport to the co-adsorbed $C_2H_6$ species. For the diffusion of $C_2H_6$ through both Ni-BT-Pe-1 and Ni-BT-Pe-2, the $D_c/r_c^2$ was estimated to be $2.86 \times 10^{-3}$ $s^{-1}$. The diffusion of $C_2H_6$ in the presence of $C_2H_4$ dropped by about 9% between powder and pellet samples, indicating that the intercrystalline diffusional resistances become pronounced for $C_2H_6$ through Ni-BT pellets. However, the diffusion time constant was unchanged at two different pellet sizes, indicating micropore diffusion to be the rate limiting step to mass transfer and, thus, the controlling factor for diffusion for $C_2H_6$ through the pellets. The ZLC desorption curves of $C_2H_4$ in the presence of $C_2H_6$ from Ni-BT (Figure 8) indicated the presence of mass transfer resistances. Such trend could be explained by the intrusion

of CH-H and CH- $\pi$ interactions at the external surface of the MOF between its $Ni^{+2}$ metal ions and the $C_2H_4$ double bonds.

Table 5. Diffusivity data for $C_2H_6$ in Ni-BT-P and Ni-BT-Pe.

| **Material** | **Sorbate** | **Flow Rate (mL/min)** | **-Slope × $10^2$ ($s^{-1}$)** | **$D_c/r_c^2$ × $10^3$ ($s^{-1}$)** | ***L*** |
|---|---|---|---|---|---|
| **Ni-BT-P** | $C_2H_6$ | 10.5 | 3.29 | 3.33 | 46 |
| | | 13.5 | 3.31 | 3.35 | 75 |
| | | 16.5 | 3.31 | 3.35 | 74 |
| **Avg.** | | | | 3.34 | |
| **Ni-BT-P** | $C_2H_6$ / $C_2H_4$ | 10.5 | 3.07 | 3.11 | 39 |
| | | 13.5 | 3.11 | 3.15 | 48 |
| | | 16.5 | 3.13 | 3.17 | 58 |
| **Avg.** | | | | 3.14 | |
| **Ni-BT-Pe-1** | $C_2H_6$ / $C_2H_4$ | 16.5 | 2.82 | 2.86 | 33 |
| | | 22.5 | 2.81 | 2.85 | 42 |
| | | 30.0 | 2.83 | 2.87 | 58 |
| **Avg.** | | | | 2.86 | |
| **Ni-BT-Pe-2** | $C_2H_6$ / $C_2H_4$ | 16.5 | 2.84 | 2.88 | 46 |
| | | 22.5 | 2.82 | 2.86 | 68 |
| | | 30.0 | 2.80 | 2.84 | 71 |
| **Avg.** | | | | 2.86 | |

This results in strong external adsorption on the surface of the Ni-BT pore entrances (Jorge et al., 2010; Lamia et al., 2009). The plots of *1/L´* versus *1/F* (Figures S8 and S9, Supporting Information) resulted in $D_c/kr_c$ values of 0.18, 0.03, 0.03, and 0.04 for Ni-BT-

P single and binary gas mixtures and Ni-BT-Pe, respectively. The single-component $C_2H_4$ diffusion yielded the highest measurement of surface resistance, however, it can be observed that the magnitude of surface resistance was decreased for the binary component gas trials of Ni-BT-P, which could be correlated with the co-adsorption of $C_2H_4$ and $C_2H_6$ on the surface of Ni-BT.

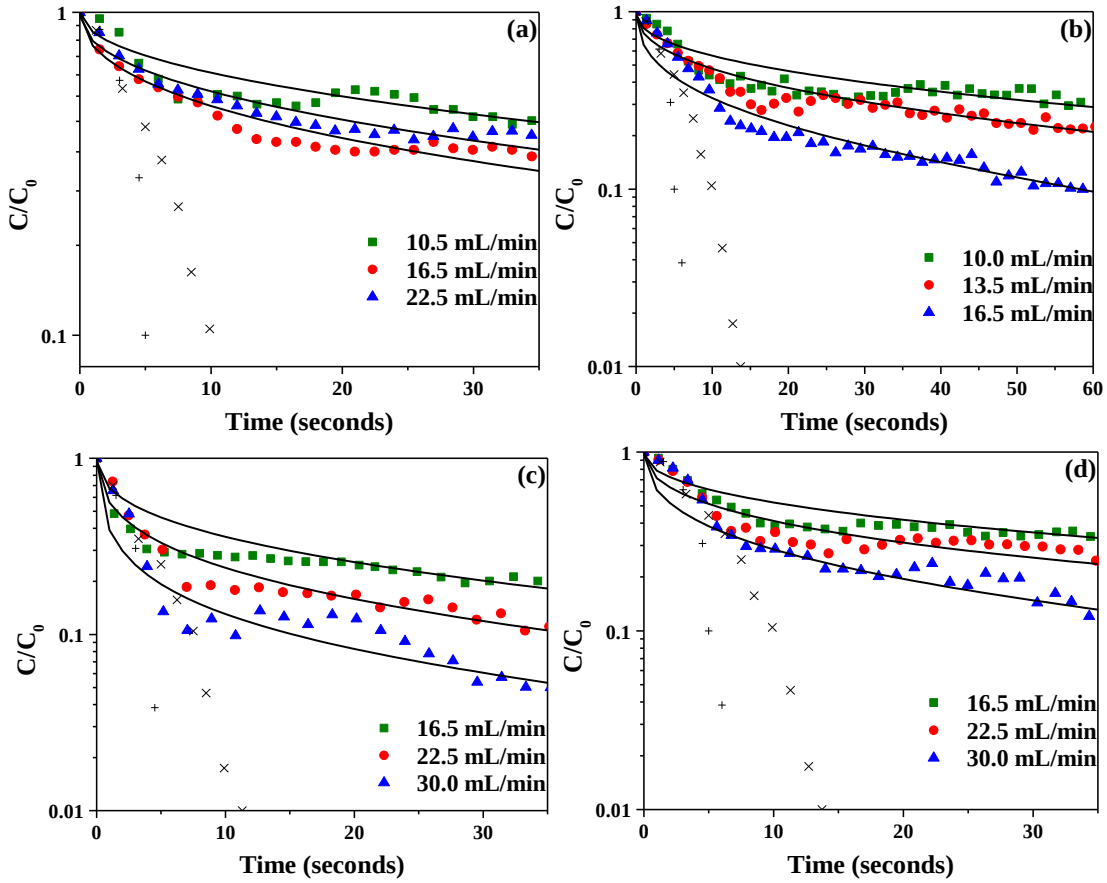


Figure 6. ZLC desorption curves for $C_2H_4$ in the presence of $C_2H_6$ at 25 °C for (a) Ni-BT-P single and (b) Ni-BT-P binary system (c) Ni-BT-Pe-1 binary system, and (d) Ni-BT-Pe-2 binary system fit against ZLC model curves and blank responses: (×) at 5.0 mL/min and (+) at 10.5 mL/min.

The diffusivity values of $C_2H_4$ for Ni-BT-P and Ni-BT-Pe were both found to increase in the presence of $C_2H_6$, but only slightly. This is contradictory to the diffusivity

behavior that we would expect to see both for binary diffusion in powder and pellet forms. Referring to Figure 6a-c, this could be the result of uncertainties arising from deviations in data-points in the long-time region of the desorption curve. Investigation of the pellet samples found that the diffusion of $C_2H_4$ through the smaller pellet size, Ni-BT-Pe-1, was larger than that of Ni-BT-Pe-2, indicating of the presence of macropore diffusional effects.

Table 6. Diffusivity data for $C_2H_4$ in Ni-BT-P and Ni-BT-Pe.

| **Material** | **Sorbate** | **Flow Rate (mL/min)** | **-Slope × $10^2$ ($s^{-1}$)** | $D_c/r_c^2 \times 10^3$ ($s^{-1}$) | $\beta_1$ | $L'$ | $L$ |
|---|---|---|---|---|---|---|---|
| **Ni-BT-P** | $C_2H_4$ | 10.5 | 0.64 | 1.48 | 2.2 | 2.5 | 4.5 |
| | | 16.5 | 0.74 | 1.28 | 2.4 | 2.7 | 5.3 |
| | | 22.5 | 0.75 | 1.27 | 2.4 | 3.8 | 12 |
| **Avg.** | | | | 1.34 | | | |
| **Ni-BT-P** | $C_2H_4$ / $C_2H_6$ | 10.5 | 0.63 | 1.01 | 2.5 | 4.0 | 4.5 |
| | | 13.5 | 0.82 | 1.23 | 2.6 | 5.1 | 6.0 |
| | | 16.5 | 1.73 | 2.36 | 2.7 | 6.9 | 8.7 |
| **Avg.** | | | | 1.53 | | | |
| **Ni-BT-Pe-1** | $C_2H_4$ / $C_2H_6$ | 16.5 | 1.51 | 2.14 | 2.7 | 6.1 | 7.4 |
| | | 22.5 | 1.87 | 2.38 | 2.8 | 8.8 | 12 |
| | | 30.0 | 1.91 | 2.26 | 2.9 | 13 | 21 |
| **Avg.** | | | | 2.26 | | | |
| **Ni-BT-Pe-2** | $C_2H_4$ / $C_2H_6$ | 16.5 | 1.13 | 1.18 | 2.5 | 4.0 | 4.8 |
| | | 22.5 | 0.71 | 1.05 | 2.6 | 5.3 | 6.7 |
| | | 30.0 | 1.84 | 2.56 | 2.7 | 6.4 | 8.6 |
| **Avg.** | | | | 1.60 | | | |

However, further examination revealed the diffusion time constant of Ni-BT-Pe-1 is not as great as the product of the time constant of Ni-BT-Pe-2 multiplied by the ratio of the pellet radii, illustrating that for $C_2H_4$, both micropore and macropore diffusions contribute to the overall diffusion rate. However, the diffusivity values obtained for the binary diffusion of Ni-BT-P and Ni-BT-Pe were essentially equivalent, indicating that the diffusion of $C_2H_4$ through Ni-BT in the presence of $C_2H_6$ is not significantly affected by intercrystalline resistances. However, extracting diffusion values outside of the diffusion-controlled regime ($L' > 10$) are subject to uncertainty. The $C/C_0$ *vs. Ft* plots for these curves (Figure S5, Supporting Information) show an overlap of the response curves, indicating that they are not in a region of complete kinetic control. This is further supported by the low $L$ values tabulated in Table 6. Therefore, the diffusivity values should again be read with caution.

The most common studied adsorbents for olefin/paraffin separation include zeolite 4A, $Ag^+$-exchanged resins, carbon molecular sieves (CMS), and more recently Mg-MOF-74. While these four materials are preferentially selective to olefins over paraffins, which is outside the scope of this work, the diffusion kinetics of these materials have been studied extensively and the following $D_c/r_c^2$ values at 25 °C have been tabulated in Table 7 in order to prove a general comparison to the diffusion time constant values outlined here. ZIF-7-P, Ni-BT-P, $Ag^+$-resin, and Mg-MOF-74 all exhibit higher $D_c/r_c^2$ values for $C_2H_6$ over $C_2H_4$.

Table 7. Comparison of diffusion time constants of ethane and ethylene in zeolite 4A, $Ag^+$-exchanged resins, and other adsorbents at 25 °C.

| **Material** | **Sorbate** | $\boldsymbol{D_c/r_c^2 \times 10^3}$ **($s^{-1}$)** | **Ref.** |
|---|---|---|---|
| **ZIF-7-P** | $C_2H_6$ | 3.22 | This work |
| **ZIF-7-P** | $C_2H_4$ | 1.67 | This work |
| **Ni-BT-P** | $C_2H_6$ | 3.34 | This work |
| **Ni-BT-P** | $C_2H_4$ | 1.38 | This work |
| **Zeolite 4A** | $C_2H_6$ | 0.164 | (Rege et al., 1998) |
| **Zeolite 4A** | $C_2H_4$ | 5.12 | (Rege et al., 1998) |
| **$Ag^+$ -resin** | $C_2H_6$ | 0.107 | (Rege et al., 1998) |
| **$Ag^+$ -resin** | $C_2H_4$ | 0.103 | (Rege et al., 1998) |
| **CMS** | $C_2H_6$ | - | (Rege et al., 1998) |
| **CMS** | $C_2H_4$ | 0.00189 | (Rege et al., 1998) |
| **Mg-MOF-74** | $C_2H_6$ | 13.9 | (Bao et al., 2011) |
| **Mg-MOF-74** | $C_2H_4$ | 7.12 | (Bao et al., 2011) |

For all the materials investigated here, $C_2H_6$ exhibited higher $D_c/r_c^2$ values than $C_2H_4$ for single and binary gas trials. Considering the kinetic diameters of $C_2H_6$ and $C_2H_4$ alone (0.44 nm and 0.42 nm, respectively), one would initially expect that $C_2H_4$ would display faster kinetics within the pores of the adsorbents due to its smaller size. The pores of ZIF-7 and Ni-BT samples, found to be larger than 1.2 nm, (Thakkar et al., 2018), are large enough that the transport of the sorbate in both single and binary gas trials was not inhibited by pore size. Therefore, the slower kinetics of $C_2H_4$ is best described as a result of the CH-H interactions formed between the sorbate molecules and the adsorbent. Our ZLC measurement results suggested that there exists substantial mass transfer resistances

at the surface of adsorbent crystals, affecting the sorption rate of $C_2H_4$ and inhibiting its motion out of the pores (Bao et al., 2011; Rege et al., 1998).

## 5. CONCLUSION

In this investigation, diffusion of ethylene and ethane in two ethane-selective adsorbents, namely, ZIF-7 and Ni-BT were investigated via ZLC method and intracrystalline diffusivity of the gases through powder and pellet forms of the adsorbents were determined at 25 °C. Both single and binary component gas mixtures were used to assess the effect of coadsorption. Our experimental results indicated that in binary system, the diffusion time constants measured were slightly lower than those in single component system. It was also found that ethylene diffusion was affected by the surface resistance due to strong interactions between the C-C double bond at surface of the adsorbents. Finally, our investigation highlighted the effect of intercrystalline resistances on the diffusion of ethane and ethylene in the pellets. The diffusion of ethane in pellet samples of both ZIF-7 and Ni-BT revealed intracrystalline diffusion to be the controlling mass transfer regime, while diffusion of ethylene revealed contributing effects of crystalline and macropore diffusion.

## REFERENCES

Baker, R.W., 2002. Future directions of membrane gas separation technology. Ind. Eng. Chem. Res. 41, 1393–1411. https://doi.org/10.1021/ie0108088

Bao, Z., Alnemrat, S., Yu, L., Vasiliev, I., Ren, Q., Lu, X., Deng, S., 2011. Adsorption of ethane, ethylene, propane, and propylene on a magnesium-based metal-organic framework. Langmuir 27, 13554–13562. https://doi.org/10.1021/la2030473

Bloch, E., Queen, W., Krishna, R., Zadrozny, J., Brown, C., Long, J., 2012. Hydrocarbon Separations in a Metal-Organic Framework with Open Iron(II) Coordination Sites. Science (80-. ). 335, 1606–1610.

Brandani, F., Ruthven, D., 2003. Measurement of Adsorption Equilibria by the Zero Length Column (ZLC) Technique Part 2: Binary Systems. Ind. Eng. Chem. Res. 42, 1462–1469. https://doi.org/10.1021/ie020573f

Brandani, F., Ruthven, D., Coe, C.G., 2003. Measurement of adsorption equilibrium by the zero length column (ZLC) technique part 1: Single-component systems. Ind. Eng. Chem. Res. 42, 1451–1461. https://doi.org/10.1021/ie020572n

Brandani, S., 2016. A Simple Graphical Check of Consistency for Zero Length Column Desorption Curves. Chem. Eng. Technol. 39, 1194–1198. https://doi.org/10.1002/ceat.201500634

Brandani, S., 1998. Effects of nonlinear equilibrium on zero length column experiments. Chem. Eng. Sci. 53, 2791–2798. https://doi.org/10.1016/S0009-2509(98)00075-X

Brandani, S., 1996. Analytical solution for ZLC desorption curves with bi-porous adsorbent particles. Chem. Eng. Sci. 51, 3283–3288. https://doi.org/10.1016/0009-2509(95)00399-1

Brandani, S., Cavalcante, C., Guimaraes, A., Ruthven, D.M., 1998. Heat Effects in ZLC Experiments. Adsorption 4, 275–285. https://doi.org/Doi 10.1023/A:1008837801299

Brandani, S., Jama, M.A., Ruthven, D.M., 2000. ZLC measurements under non-linear conditions. Chem. Eng. Sci. 55, 1205–1212. https://doi.org/10.1016/S0009-2509(99)00411-X

Brandani, S., Ruthven, D.M., 1996. Analysis of ZLC desorption curves for gaseous systems. Adsorption 2, 133–143. https://doi.org/10.1007/BF00127043

Brandani, S., Ruthven, D.M., 1995. Analysis of ZLC desorption curves for liquid systems. Adsorption 50, 2055–2059. https://doi.org/10.1007/BF00127043

Chen, D.L., Wang, N., Wang, F.F., Xie, J., Zhong, Y., Zhu, W., Johnson, J.K., Krishna, R., 2014. Utilizing the gate-opening mechanism in ZIF-7 for adsorption discrimination between N2O and CO2. J. Phys. Chem. C 118, 17831–17837. https://doi.org/10.1021/jp5056733

Chen, J., Eldridge, B., Rosen, E., Bielawski, C., 2010. A Study of Cu(I)-Ethylene Complexatiopn for Olefin-Paraffin Separation. AIChE J. 57, 630–644. https://doi.org/10.1002/aic

Eic, M., Ruthven, D.M., 1988. A new experimental technique for measurement of intracrystalline diffusivity. Zeolites 8, 40–45. https://doi.org/10.1016/S0144-2449(88)80028-9

Eldridge, R.B., 1993. Olefin/Paraffin Separation Technology: A Review. Ind. Eng. Chem. Res. 32, 2208–2212. https://doi.org/10.1021/ie00022a002

Furukawa, H., Cordova, K.E., O'Keeffe, M., Yaghi, O.M., 2013. The chemistry and applications of metal-organic frameworks. Science (80-. ). 341. https://doi.org/10.1126/science.1230444

Furukawa, H., Ko, N., Go, Y.B., Aratani, N., Choi, S.B., Choi, E., Yazaydin, a O., Snurr, R.Q., O'Keeffe, M., Kim, J., Yaghi, O.M., 2010. Ultrahigh Porosity in Meta-Organic Frameworks. Science (80-. ). 329, 424. https://doi.org/10.1126/science.1192160

Grande, C.A., Rodrigues, A.E., 2004. Adsorption Kinetics of Propane and Propylene in Zeolite 4A. Chem. Eng. Res. Des. 82, 1604–1612. https://doi.org/10.1205/cerd.82.12.1604.58029

Gücüyener, C., Van Den Bergh, J., Gascon, J., Kapteijn, F., 2010. Ethane/ethene separation turned on its head: Selective ethane adsorption on the metal-organic framework ZIF-7 through a gate-opening mechanism. J. Am. Chem. Soc. 132, 17704–17706. https://doi.org/10.1021/ja1089765

Heinke, L., Kortunov, P., Tzoulaki, D., Kärger, J., 2007. The options of interference microscopy to explore the significance of intracrystalline diffusion and surface permeation for overall mass transfer on nanoporous materials. Adsorption 13, 215–223. https://doi.org/10.1007/s10450-007-9048-y

Hu, X., Brandani, S., Benin, A.I., Willis, R.R., 2018. Testing the stability of novel adsorbents for carbon capture applications using the zero length column technique. Chem. Eng. Res. Des. 131, 406–413. https://doi.org/10.1016/j.cherd.2018.01.023

James, S.L., 2003. Metal-organic frameworks. Chem. Soc. Rev. 32, 276–288. https://doi.org/10.1039/b200393g

Jiang, M., Eić, M., 2003. Transport properties of ethane, butanes and their binary mixtures in MFI-type zeolite and zeolite-membrane samples. Adsorption 9, 225–234. https://doi.org/10.1023/A:1024797716739

Jorge, M., Lamia, N., Rodrigues, A.E., 2010. Molecular simulation of propane/propylene separation on the metal-organic framework CuBTC. Colloids Surfaces A Physicochem. Eng. Asp. 357, 27–34. https://doi.org/10.1016/j.colsurfa.2009.08.025

Kärger, J., Ruthven, D.M., Theodorou, D.N., 2012. Diffusion in Nanoporous Materials, Diffusion in Nanoporous Materials. https://doi.org/10.1002/9783527651276

Kortunov, P., Chmelik, C., Kärger, J., Rakoczy, R.A., Ruthven, D.M., Traa, Y., Vasenkov, S., Weitkamp, J., 2005. Sorption kinetics and intracrystalline diffusion of methanol in ferrierite: An example of disguised kinetics. Adsorption 11, 235–244. https://doi.org/10.1007/s10450-005-5396-7

Kroon, M.C., Vega, L.F., 2009. Selective paraffin removal from ethane/ethylene mixtures by adsorption into aluminum methylphosphonate-α: A molecular simulation study. Langmuir 25, 2148–2152. https://doi.org/10.1021/la803042z

Lamia, N., Jorge, M., Granato, M.A., Almeida Paz, F.A., Chevreau, H., Rodrigues, A.E., 2009. Adsorption of propane, propylene and isobutane on a metal-organic framework: Molecular simulation and experiment. Chem. Eng. Sci. 64, 3246–3259. https://doi.org/10.1016/j.ces.2009.04.010

Leclerc, H., Vimont, A., Lavalley, J.C., Daturi, M., Wiersum, A.D., Llwellyn, P.L., Horcajada, P., Férey, G., Serre, C., 2011. Infrared study of the influence of reducible iron(III) metal sites on the adsorption of CO, CO2, propane, propene and propyne in the mesoporous metalorganic framework MIL-100. Phys. Chem. Chem. Phys. 13, 11748–11756. https://doi.org/10.1039/c1cp20502a

Li, J.R., Kuppler, R.J., Zhou, H.C., 2009. Selective gas adsorption and separation in metal-organic frameworks. Chem. Soc. Rev. 38, 1477–1504. https://doi.org/10.1039/b802426j

Liang, W., Xu, F., Zhou, X., Xiao, J., Xia, Q., Li, Y., Li, Z., 2016. Ethane selective adsorbent Ni ( bdc )( ted ) 0 . 5 with high uptake and its signi fi cance in adsorption separation of ethane and ethylene. Chem. Eng. Sci. 148, 275–281. https://doi.org/10.1016/j.ces.2016.04.016

Okamoto, K. ichi, Kawamura, S., Yoshino, M., Kita, H., Hirayama, Y., Tanihara, N., Kusuki, Y., 1999. Olefin/paraffin separation through carbonized membranes derived from an asymmetric polyimide hollow fiber membrane. Ind. Eng. Chem. Res. 38, 4424–4432. https://doi.org/10.1021/ie990209p

Padin, J., Rege, S.U., Yang, R.T., Cheng, L.S., 2000. Molecular sieve sorbents for kinetic separation of propane/propylene. Chem. Eng. Sci. 55, 4525–4535. https://doi.org/10.1016/S0009-2509(00)00099-3

Padin, J., Yang, R.T., 2000. New sorbents for olefin / paraffon separations by adsorption via pi-complexation : synthesis and effects of substrates. Chem. Eng. Sci. 55, 2607–2616.

Pinnau, I., Toy, L.G., 2001. Solid polymer electrolyte composite membranes for olefin / paraffin separation. J. Memb. Sci. 184, 39–48.

Rege, S.U., Padin, J., Yang, R.T., 1998. Olefin/Paraffin Separations by Adsorption: π-Complexation vs. Kinetic Separation. AIChE J. 44, 799–809. https://doi.org/10.1002/aic.690440405

Ren, T., Patel, M., Blok, K., 2006. Olefins from conventional and heavy feedstocks: Energy use in steam cracking and alternative processes. Energy 31, 425–451. https://doi.org/10.1016/j.energy.2005.04.001

Rodríguez, J.F., Valverde, J.L., Rodrigues, A.E., 1998. Measurements of Effective Self-diffusion Coefficients in a Gel-Type Cation Exchanger by the Zero-Length-Column Method. Ind. Eng. Chem. Res. https://doi.org/10.1021/ie970684s

Rungta, M., Zhang, C., Koros, W.J., Xu, L., 2013. Membrane-based ethylene/ethane separation: The upper bound and beyond. AIChE J. https://doi.org/10.1002/aic.14105

Ruthven, D., Brandani, F., 2005. ZLC response for systems with surface resistance control. Adsorption 11, 31–34. https://doi.org/10.1007/s10450-005-1090-z

Ruthven, D.M., Reyes, S.C., 2007. Adsorptive separation of light olefins from paraffins. Microporous Mesoporous Mater. 104, 59–66. https://doi.org/10.1016/j.micromeso.2007.01.005

Ruthven, D.M., Vidoni, A., 2012. ZLC diffusion measurements: Combined effect of surface resistance and internal diffusion. Chem. Eng. Sci. 71, 1–4. https://doi.org/10.1016/j.ces.2011.11.040

Ruthven, D.M., Xu, Z., 1993. Diffusion of oxygen and nitrogen in 5A zeolite crystals and commercial 5A pellets. Chem. Eng. Sci. https://doi.org/10.1016/0009-2509(93)80214-B

Safarik, D.J., Eldridge, R.B., 1998. Olefin/paraffin separations by reactive absorption: a review. Ind. Eng. Chem. Res. 37, 2571–2581. https://doi.org/10.1021/ie970897h

Seabra, R., Ribeiro, A.M., Gleichmann, K., Ferreira, A.F.P., Rodrigues, A.E., 2019. Adsorption equilibrium and kinetics of carbon dioxide, methane and nitrogen on binderless zeolite 4A adsorbents. Microporous Mesoporous Mater. 277, 105–114. https://doi.org/10.1016/j.micromeso.2018.10.024

Silva, J.A.C., Rodrigues, A.E., 1997. Equilibrium and Kinetics of n-Hexane Sorption in Pellets of 5A Zeolite. AIChE J. 43, 2524–2534. https://doi.org/10.1002/aic.690431014

Silva, J.A.C., Rodrigues, A.E., 1996. Analysis of ZLC technique for diffusivity measurements in bidisperse porous adsorbent pellets. Gas Sep. Purif. https://doi.org/10.1016/S0950-4214(96)00021-7

Silva, J.A.C., Schumann, K., Rodrigues, A.E., 2012. Sorption and kinetics of CO2and CH4in binderless beads of 13X zeolite. Microporous Mesoporous Mater. 158, 219–228. https://doi.org/10.1016/j.micromeso.2012.03.042

Silva, J.C.A., da Silva, F.A., Rodrigues, A.E., 2001. An analytical solution for the analysis of zero-length-column experiments with heat effects. Ind. Eng. Chem. Res. 40, 3697–3702. https://doi.org/10.1021/ie001045b

Takht Ravanchi, M., Kaghazchi, T., Kargari, A., 2009. Application of membrane separation processes in petrochemical industry: a review. Desalination 235, 199–244. https://doi.org/10.1016/j.desal.2007.10.042

Thakkar, H., Al-Naddaf, Q., Legion, N., Hovis, M., Krishnamurthy, A., Rownaghi, A.A., Rezaei, F., 2018. Adsorption of Ethane and Ethylene over 3D-Printed Ethane-Selective Monoliths. ACS Sustain. Chem. Eng. in press.

U.S. Department of Energy, 2005. Materials for separation technologies: energy and emission reduction opportunities v. https://doi.org/10.2172/1218755

Van Den Bergh, J., Gücüyener, C., Pidko, E.A., Hensen, E.J.M., Gascon, J., Kapteijn, F., 2011. Understanding the anomalous alkane selectivity of ZIF-7 in the separation of light alkane/alkene mixtures. Chem. - A Eur. J. 17, 8832–8840. https://doi.org/10.1002/chem.201100958

Vidoni, A., 2011. Adsorption and Diffusion of Light Hydrocarbons in DDR Zeolite. University of Maine.

Vidoni, A., Ruthven, D.M., 2012. Diffusion of $C_2H_6$ and $C_2H_4$ in DDR Zeolite. Ind. Eng. Chem. Res. 51, 1383–1390. https://doi.org/10.1021/ie202449q

Zhou, H.C., Long, J.R., Yaghi, O.M., 2012. Introduction to metal-organic frameworks. Chem. Rev. 112, 673–674. https://doi.org/10.1021/cr300014x

## SUPPORTING INFORMATION

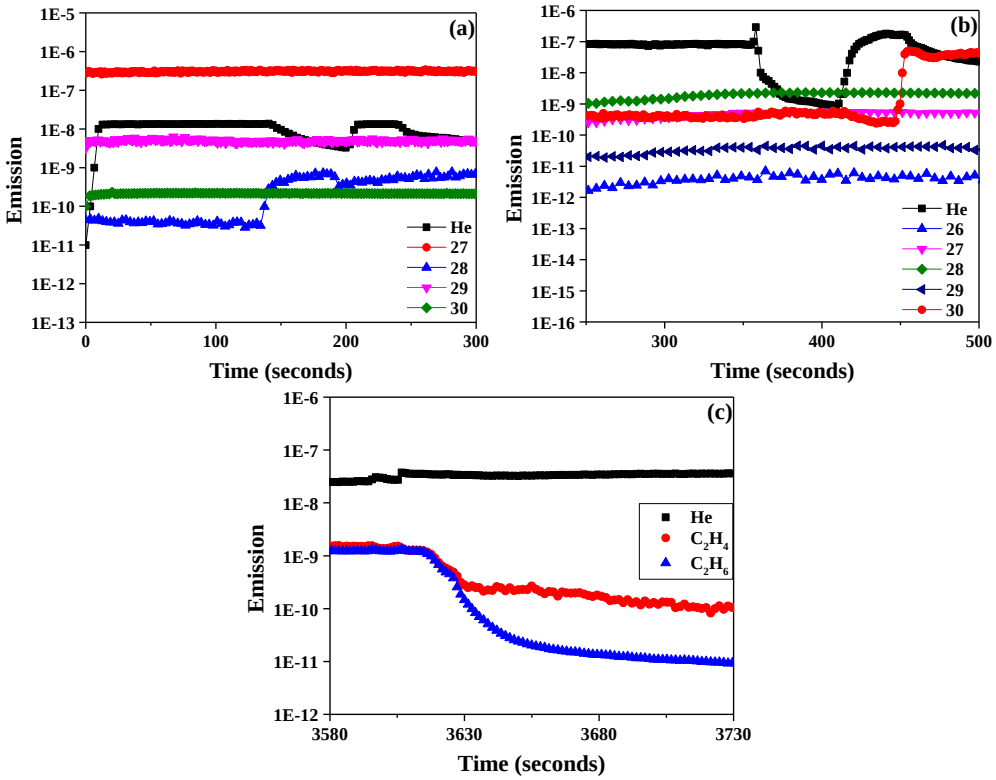


Figure S1. Raw emission data of (a) breakthrough curve for $C_2H_4$ mixed in a He stream tested at a range of amus, (b) breakthrough curve of $C_2H_6$ mixed in a He stream tested at a range of amus, and (c) a binary $C_2H_4$ – $C_2H_6$ run over ZIF-7-P.

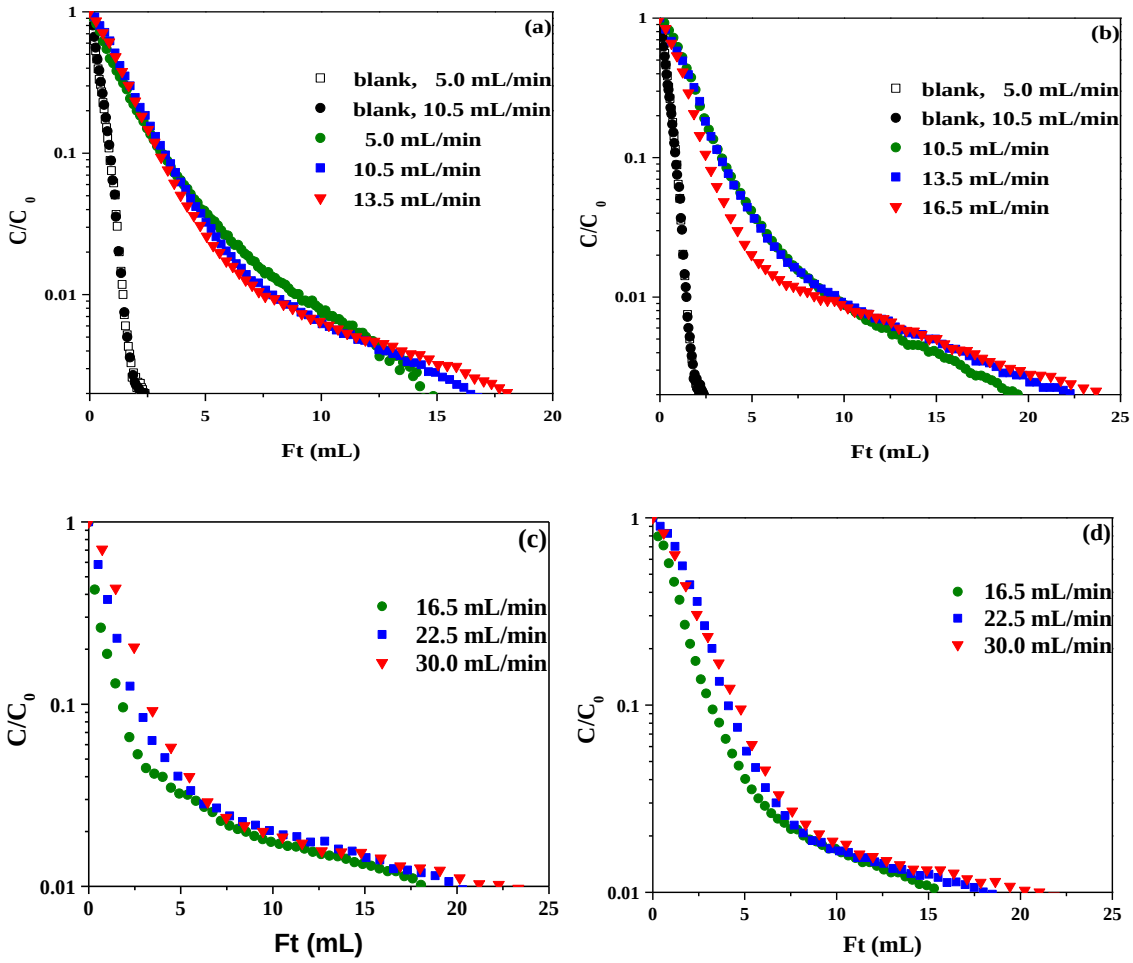


Figure S2. Ft (mL) plot demonstrating kinetically controlled experiments of $C_2H_6$ at 25 °C for (a) ZIF-7-P for single component system, (b) ZIF-7-P binary system, and (c) ZIF-7-Pe-1 binary system, and (d) ZIF-7-Pe-2 binary system.

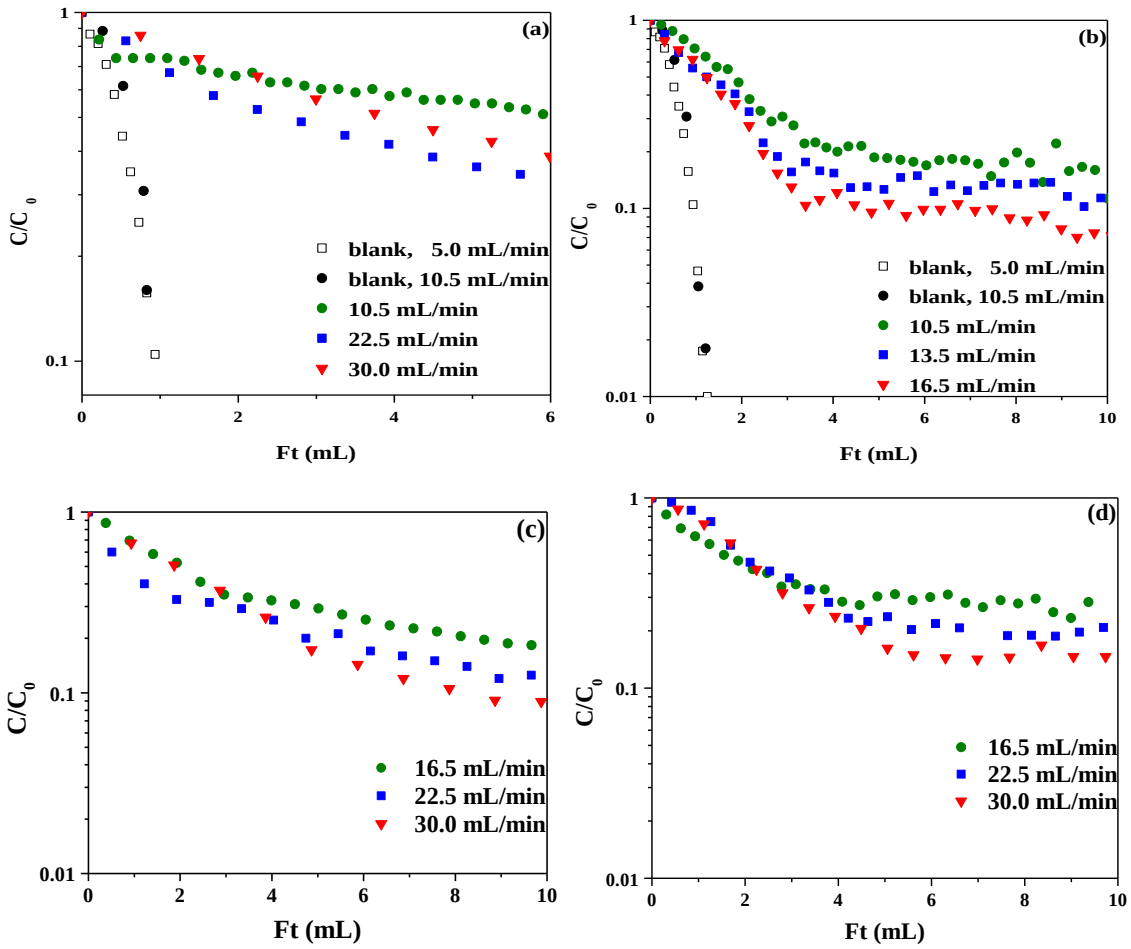


Figure S3. Ft (mL) plot demonstrating kinetically controlled experiments of $C_2H_4$ at 25 °C for (a) ZIF-7-P for single component system, (b) ZIF-7-P binary system, (c) ZIF-7-Pe-1 binary system, and (d) ZIF-7-Pe-2 binary system.

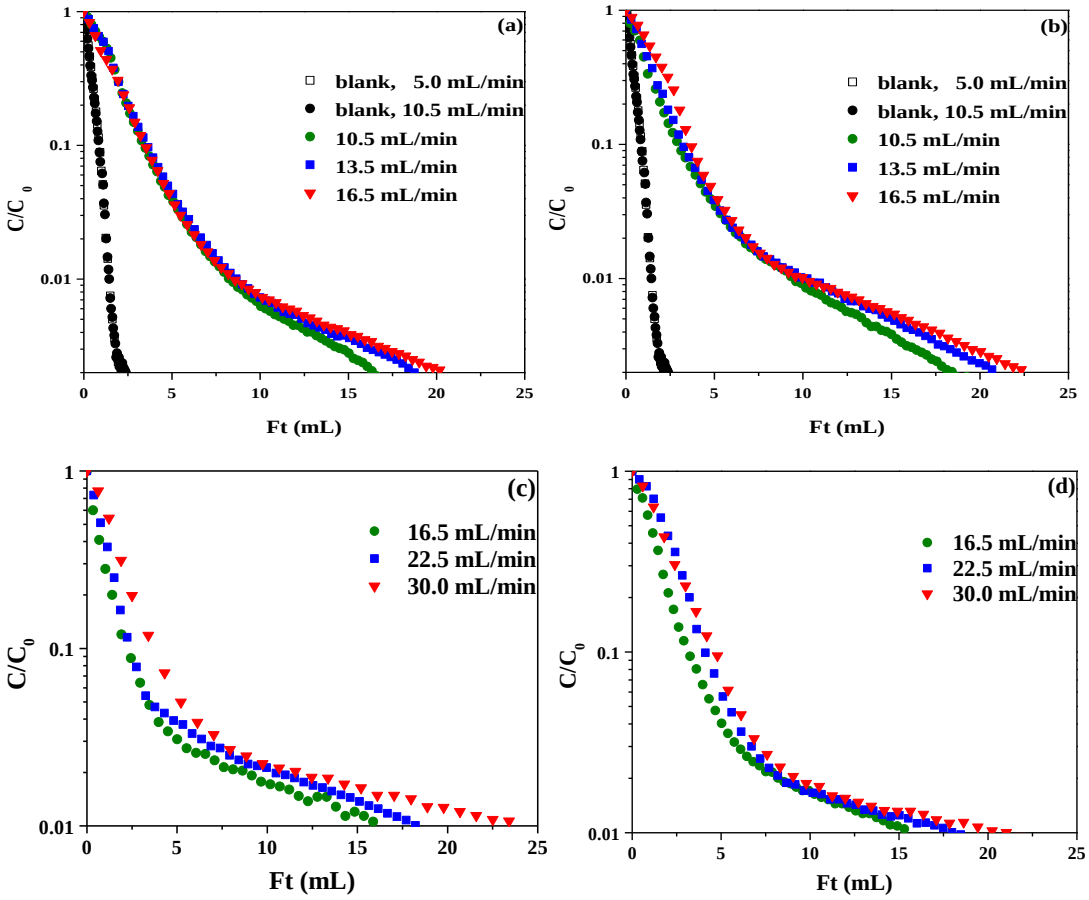


Figure S4. Ft (mL) plot demonstrating kinetically controlled experiments of $C_2H_6$ at 25 °C for (a) Ni-BT-P for single component system, (b) Ni-BT-P binary system, and (c) Ni-BT-Pe-1 binary system, and (d) Ni-BT-Pe-2 binary system.

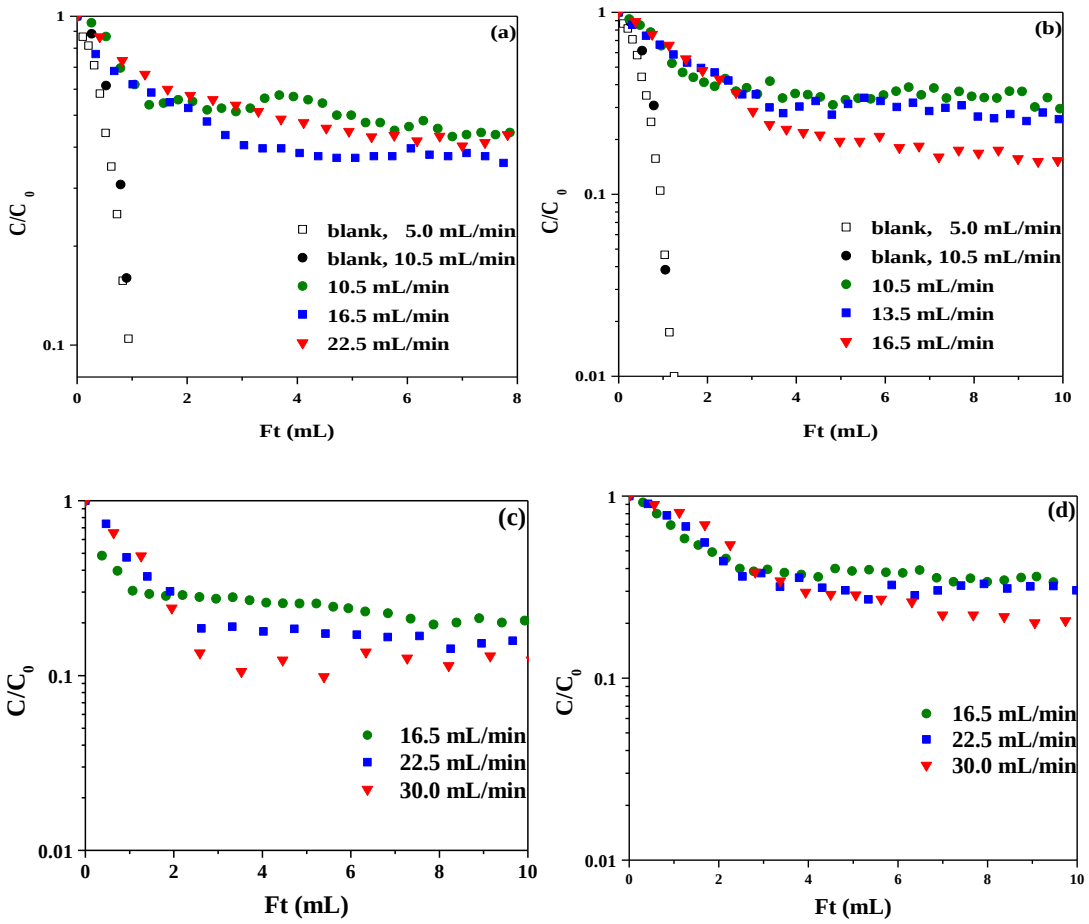


Figure S5. Ft (mL) plot demonstrating kinetically controlled experiments of $C_2H_4$ at 25 °C for (a) Ni-BT-P for single component system, (b) Ni-BT-P binary system, (c) Ni-BT-Pe-1 binary system, and (d) Ni-BT-Pe-2 binary system.

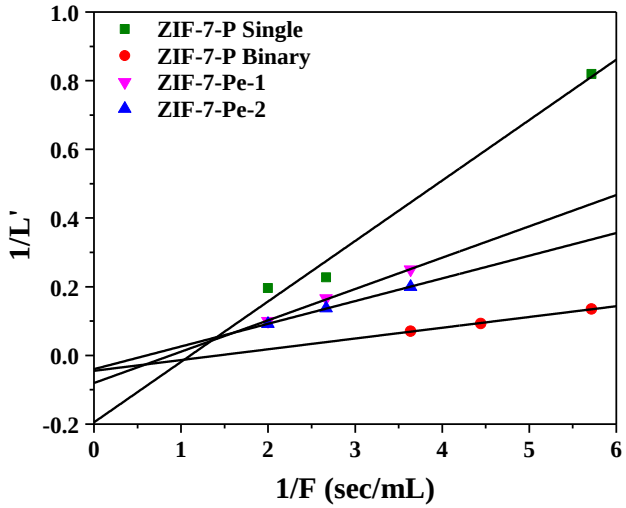


Figure S6. Plot of 1/*L´* vs. reciprocal purge rate for $C_2H_4$ in ZIF-7 at 25 °C for ZIF-7-P single gas component trials, ZIF-7-P binary gas trials, ZIF-7-Pe-1, and ZIF-7-Pe-2.

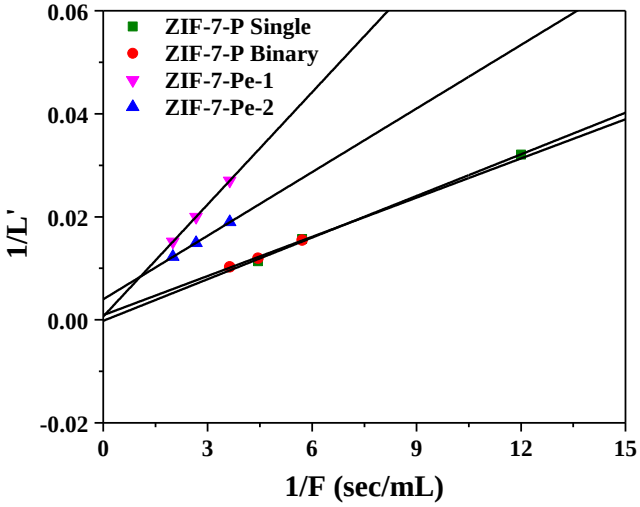


Figure S7. Plot of 1/*L´* vs. reciprocal purge rate for $C_2H_6$ in ZIF-7 at 25 °C for ZIF-7-P single gas component trials, ZIF-7-P binary gas trials, ZIF-7-Pe-1, and ZIF-7-Pe-2.

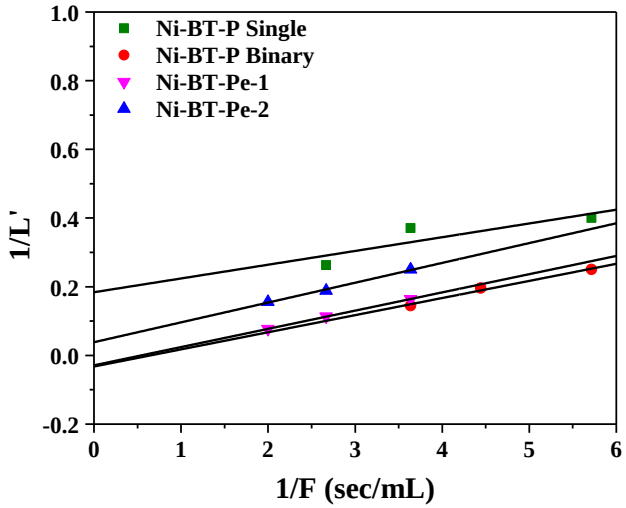


Figure S8. Plot of $1/L'$ vs. reciprocal purge rate for $C_2H_4$ in Ni-BT at 25 °C for Ni-BT-P single gas component trials, Ni-BT-P binary gas trials, Ni-BT-Pe-1, and Ni-BT-Pe-2.

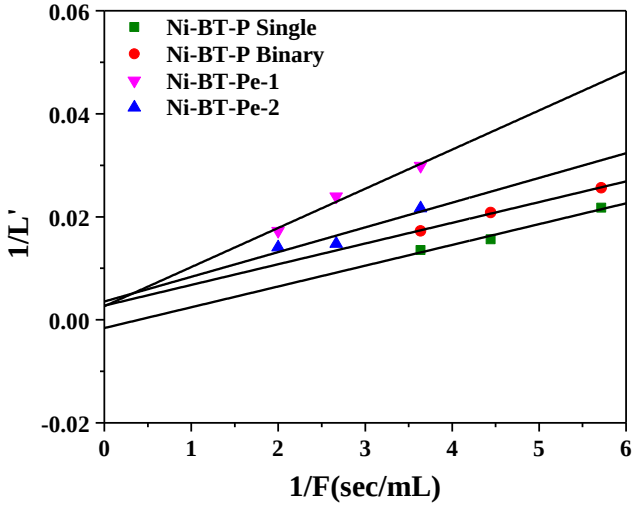


Figure S9. Plot of $1/L'$ vs. reciprocal purge rate for $C_2H_6$ in Ni-BT at 25 °C for Ni-BT-P single gas component trials, Ni-BT-P binary gas trials, Ni-BT-Pe-1, and Ni-BT-Pe-2.

# II. DIFFUSION KINETICS OF $CO_2$ IN AMINE-IMPREGNATED MIL-101, ALUMINA, AND SILICA ADSORBENTS

Teresa Gelles, Fateme Rezaei

Department of Chemical and Biochemical Engineering, Missouri University of Science and Technology, Rolla, MO 65409

## ABSTRACT

$CO_2$ sorption kinetics of poly(ethylenimine) (PEI)-impregnated MIL-101, γ-alumina, and UVM-7 silica were investigated by the zero-length column (ZLC) technique for the purpose of understanding the effect of amine-content, adsorbent porosity, and adsorption temperature on $CO_2$ sorption rates. Each of the adsorbents was impregnated with three different amine contents (20, 35, and 50 wt. %) and the effective diffusion time constants were determined at 25 °C. For each respective adsorbent, it was found that increasing the amine content results in diminished diffusion rates. Additionally, it was found that the porosity of the support has a profound effect on diffusional kinetics, where microporous MIL-101 yielded substantially slow desorption rates upon amine-functionalization compared to mesoposorrous γ-alumina. PEI-impregnated UVM-7 silica was further investigated at 50 and 75 °C in order to provide insight into the effect of temperature on sorption kinetics. The results indicated that PEI-impregnated UVM-7 exhibits faster sorption kinetics at higher temperatures. Upon desorption, PEI-UVM-7 silica exhibited two distinct regions of mass transfer control that occur at different

sorption times. This is best explained by first the occurrence of surface diffusion followed by diffusion out of the PEI. The findings of this study provide novel kinetic characterizations on promising amino-adsorbents for carbon capture applications.

## 1. INTRODUCTION

The rapid rise of anthropogenic $CO_2$ emissions resulting from fossil fuel combustion has been widely identified as the primary cause to the increase in global temperatures, due to the deleterious effects of this greenhouse gas [1]. Hence, development of cost-effective carbon capture processes are essential for mitigation of $CO_2$ emissions [2–5]. Aqueous monoethanol amine (MEA) absorption is regarded as the benchmark technology for post-combustion $CO_2$ capture, but suffers from high-energy penalties upon solvent regeneration [6,7]. Alternatively, the direct removal of $CO_2$ from ambient air has arisen as an attractive option in recent years that could be implemented in residential areas to mitigate emissions resulting from transportation sources [8,9]. Therefore, solid-state adsorbents have been intensively studied as a viable, cost-effective alternative to absorption-based amine scrubbing for practical carbon capture applications.

Solid adsorbents, traditionally including zeolites, carbon molecular sieves, activated carbons, activated alumina, and metal-organic frameworks (MOFs), are physical adsorbents and have been extensively studied due to their low capture costs, low regeneration requirements, and long-term stability [10]. However, these adsorbents suffer from inferior capture capacities compared to aqueous amine-scrubbing, as well as reduced working capacities in humidified conditions [3,11]. Therefore, recent research has

focused on the incorporation of amine moieties onto the adsorbents aiming at enhancing the $CO_2$ capture capacity and selectivity of these materials [12–15].

Mesoporous oxides such as silica and γ-alumina, have been studied as support materials for incorporation of amines due to large surface areas, pore volumes, and narrow pore size distributions that eliminate the limitations imposed by microporous adsorbents on achieving dispersed amine-loadings within the material and promoting more efficient diffusion of $CO_2$ onto adsorption sites [16,17]. These supports have shown that high loadings of amine functional groups can be achieved within the pores and that, up to a certain amine content, the $CO_2$ adsorption capacity will increase with amine loading. More recently, MOFs have arisen as potential supports for amine-based $CO_2$ capture. In particular, MIL-101(Cr) displays large surface area and pore volume and has exceptional chemical and thermal stability, rendering it a suitable candidate for amine functionalization [18–20].

"Molecular basket" sorbents, first coined by Xu et al. [21], is the confinement of a polymer containing many amine groups inside the pores of a mesoporous support where synergistic effects between support and polymer result in enhanced $CO_2$ capture capacities. Branched polyethyleneimine (PEI) has been well-established as a preferred aminopolymer for amino-adsorbent functionalization due to long polymer chains that promote van der Waal's adhesion and cyclic stability within adsorbent pores. PEI-functionalization has been the focus of considerable investigations due to its a convenient and scalable synthesis procedure that renders it practical for a myriad of $CO_2$ capture applications [16,17,21–23]. PEI-impregnated MIL-101 was investigated for $CO_2$ post combustion capture by Lin et al. [24], who found that the enhanced pore volume of MIL-

101 could accommodate the loading of large quantities of amines. More recently, Durante et al. [25] examined PEI-impregnated MIL-101 for direct air capture applications, reporting uptakes of 1.3 mmol/g at 400 ppm $CO_2$ and ambient conditions. PEI has also been impregnated onto mesoporous γ-alumina and investigated for $CO_2$ capture performance. Jones and co-workers [26,27] have reported γ-alumina to be a promising adsorbent support that can capture large quantities of $CO_2$ in dilute gas streams and can withstand simulated flue gas conditions with minute decreases in working capacities. Most commonly, PEI is impregnated onto silica supports and tested for capacity and durability. Many silicas have arisen over the years to be facile supports for $CO_2$ capture, including SBA-15, MCM-41, and KIT-6 [17,28–30]. Recently, a relatively new class of bimodal mesoporous silica named UVM-7 has attracted a great deal of interest for utilization in a variety of applications[31,32].

While many investigations of amine-functionalized adsorbents focus on the improvement of the equilibrium or dynamic adsorption capacities, the characterization of the transport properties of $CO_2$ through PEI-impregnated adsorbents is lacking. Understanding the mass transfer characteristics of $CO_2$ into and out of the adsorbent is critical to the overall efficiency and performance of the capture process at industrial scale mainly because it dictates the throughout and column size. Diffusion kinetics can be measured by a variety of macroscopic and microscopic techniques, including interference microscopy (IFM), frequency response (FR), IT micro-imaging (IRM), or the zero-length column (ZLC) technique [33].

ZLC is a macroscopic technique that was popularized by Eic and Ruthven [34] and has been extensively used for the diffusion characterization of a variety of porous materials. Under well-defined conditions, the extracrystalline resistances to heat and mass

transfer are neglected and sorption kinetics are completely controlled by intracrystalline diffusion out of the pores. The ZLC model has been thoroughly characterized and expanded in order to account for structured adsorbents [35,36], liquid systems [37], heat effects [38], nonlinear systems [39,40], adsorption equilibria [41,42], and surface resistances [43,44]. However, utilizing the ZLC method to characterize the diffusion kinetics of $CO_2$ from amino-materials has been widely unexplored. Gargiulo et al. [28] applied the ZLC technique in order to measure the diffusion of $CO_2$ in PEI-impregnated SBA-15 silica at different amine-contents and temperature ranges. The authors found that diffusion is slowed upon increasing amine content, and that diffusion is enhanced at higher adsorption temperatures. To our knowledge, this is the only instance of the ZLC technique used to characterize the sorption kinetics of amino-adsorbents. More recently, Brandani and coworkers [45–47] utilized the ZLC method to measure irreversibly adsorbed $CO_2$ on the surface of amine-grafted silicas and amine-impregnated mesoporous carbons. The authors demonstrated that ZLC desorption curves can provide results comparable to calorimetric techniques for determining $CO_2$ uptakes.

In this present work, we have expanded upon previous investigations to measure the sorption kinetics of $CO_2$ in three PEI-impregnated adsorbents, namely, PEI-impregnated MIL-101, γ-alumina, and UVM-7 silica. Each adsorbent was functionalized with three different amine weights and the subsequent diffusion time constants were compared in order to provide insight into the effects of amine content on the sorption kinetics of $CO_2$. Additionally, the PEI-impregnated silica was tested at different temperatures and the sorption kinetics were compared in order to provide insight into the effect of temperature dependence on $CO_2$ diffusion in amino-adsorbents.

# 2. EXPERIMENTAL SECTION

## 2.1 MATERIAL SYNTHESIS

The MIL-101 was synthesized according to a modified hydrothermal synthesis reported in our previous work [48], the γ-alumina was synthesized according to a sol-gel procedure reported elsewhere [49], and the UVM-7 silica that was synthesized following a modified procedure reported in our previous work [50]. The materials were then functionalized with PEI ($M_W$ = 800) using a conventional wet-impregnation method. Briefly, the MIL-101, γ-alumina, and silica supports were first activated at 120 °C for 24 h under vacuum in order to remove any gaseous impurities. Next, a PEI and methanol solution was prepared using a desired amount of PEI dissolved in methanol (10 mL methanol per 5 wt. % PEI), and left to stir for 2 h. Following, a desired quantity of dried support was added to the solution and stirred under a $N_2$ atmosphere overnight. The methanol was removed by rotary evaporation and the amino-materials were dried under vacuum for 2 h at 80 °C. Each support was impregnated with 20, 35, and 50 wt. % PEI and are denoted as MIL-101-n, Alumina-n, and Silica-n (n = 20, 35, and 50 wt. %). Additionally, the bare materials are denoted as MIL-101, alumina, and silica, throughout the paper.

## 2.2 MATERIAL CHARACTERIZATION

$N_2$ physisorption measurements were obtained using a Micromeritics 3Flex gas analyzer at 77 K. Surface area was determined using Brunauer-Emmett-Teller (BET) and pore volume was estimated at $P/P_0 = 0.9$. Nonlocal density functional theory (NLDFT)

was used to determine pore sizing. Elemental analysis was performed using an Exeter CE-440 Elemental Analyzer to determine C, H, and N contents of the bare supports and amine-impregnated samples. The N content was used to quantify amine loadings for each PEI-impregnated sample.

$CO_2$ Adsorption isotherms over adsorbent materials were obtained at 25 °C using 3Flex gas analyzer. Additionally, the isotherms at 50 and 75 °C were measured for silica-supported amine adsorbents. Prior to measurement, MIL-101, γ-alumina, and silica were degassed in a Micromeritics Prevac at 150, 250, and 250 °C, respectively, for 6 h. All PEI-impregnated adsorbents were degassed at 110 °C for 1 h.

## 2.3 ZLC EXPERIMENTS

The ZLC apparatus is depicted in Figure 1. Measurements were carried out using a pre-mixed 5% $CO_2$/He carrier stream and an ultra-high purity He purge stream. Both streams were fed through mass flow controllers (MFCs) and a three-way switching valve in order to control which gas line entered the ZLC column. The ZLC column consisted of a 1/8" Swagelok union loaded with a wire mesh serving as the adsorbent bed. The ZLC was housed inside of a heating cell comprised of HTSAmptek heating tape controlled by an Omega CSi32K benchtop controller. Following the ZLC column, the effluent gas was directly monitored by a BELMass benchtop quadrouple mass spectrometer and vented through a soap-bubble flowmeter.

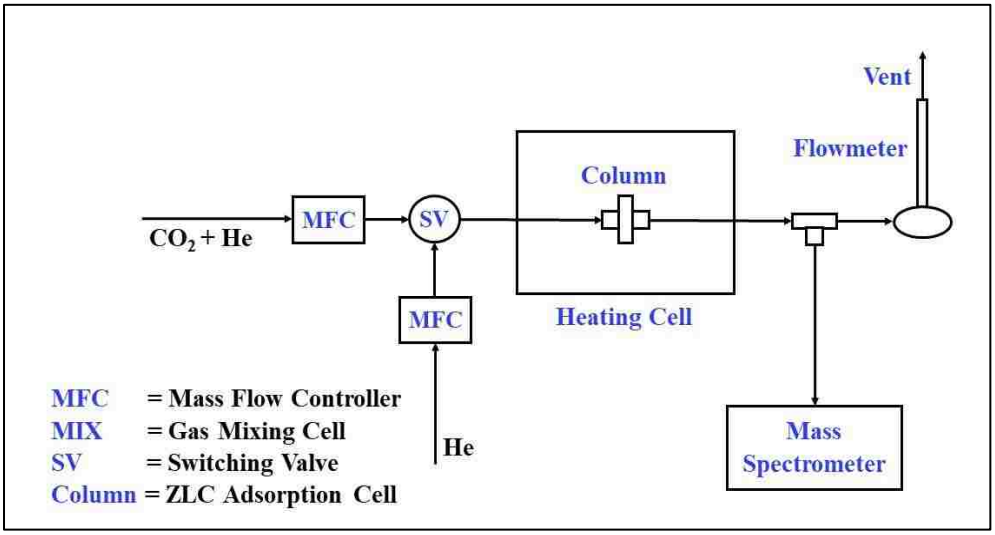


Figure 1. Schematic diagram of ZLC apparatus.

In a typical run, a small sample (between 1 - 3 mg) was loaded inside of the 1/8" Swagelok union and distributed evenly on the wire mesh. The MIL-101, γ-alumina, and silica were degassed at 150, 250, and 250 °C, respectively, for 6 h, and the amino-materials were degassed at 110 °C for 1 h under a 2 mL/min He stream. Before time zero, the pre-mixed gas carrier was introduced into the adsorption cell and the adsorbent sample was equilibrated for 1 – 2 h. Adsorption was monitored via the mass spectrometer to ensure complete sample saturation before desorption. At time zero, the valve was switched and the adsorbent sample was exposed to the He purge. The effluent gas stream was monitored for a sufficiently long time to assure complete $CO_2$ desorption from the adsorbent. Prior to material testing, blank runs were conducted in order to measure the response-time of the system at different flow rates. Blank tests are shown in Figure S1, Supporting Information.

# 3. ZLC THEORETICAL MODEL

In the ZLC experiments, a bed of adsorbent was saturated with $CO_2$ in He at a low concentration in order to reside within the linear region of Henry's law. It is assumed that the ZLC cell is well mixed, with the fluid and adsorbed species in equilibrium on the adsorbent surface. Assuming spherical particles of radius $r_c^2$ and intracrystalline diffusion $D_c$ as the rate limiting step to mass transfer, upon desorption, the response curve is derived from Fick's law of diffusion and is modeled as:

$$\frac{C}{C_0} = \sum_{n=1}^{\infty} \frac{2L}{\left[\beta_n^2 + L(L-1)\right]} \exp\left(\frac{-\beta_n^2 D_c}{r_c^2} t\right) \tag{1}$$

Studies [51,52] have shown that for $CO_2$ desorption from PEI-immobilized adsorbents, initial desorption is complex and involves the combination of several diffusion mechanisms However, beyond the initial desorption period, the rate of mass transfer is limited by the chemical reaction between $CO_2$ and the primary amine groups of the PEI as $CO_2$ diffuses out of the PEI multilayers [51–55]. Therefore, for the PEI materials, $D_c / r_c^2$ should instead be expressed by an effective diffusion time constant, $D_e / R^2$, which can be extracted from the desorption curves at long times. Under such conditions, only the first summation of eq. 1 becomes significant and Fick's law can be reduced to:

$$\ln\left(\frac{C}{C_0}\right)=\ln\left(\frac{2L}{\beta_1^2+L(L-1)}\right)-\frac{\beta_1^2 D_e}{R^2}t \tag{2}$$

where $\beta_1$ is the root of the transcendental equation:

$$\beta_1\cot(\beta_1)+L-1=0 \tag{3}$$

and $L$ is the dimensionless model parameter:

$$L=\frac{1}{3}\frac{F}{KV_s}\frac{R^2}{D_e} \tag{4}$$

where $F$ is the purge flow rate, $V_s$ is the sample volume, and $K$ is the dimensionless Henry's law constant. When the purge flow rate is sufficiently large such that $L > 10$, the resultant desorption curve is kinetically controlled and provides reliable values for diffusion. Thus, from eq. 3, $\beta_1 \to \pi$ and a plot of $ln(C/C_0)$ vs. $t$ yields a long-time asymptote with a slope of $\pi^2 D_e / R^2$. As long as $L > 10$, altering the purge flow rate may change the intercept of the curve but the slope should remain constant. For consistency, all diffusion time constants reported in this paper are referred to as $D_e/R^2$. The accuracy and reliability of ZLC theory has been thoroughly detailed in many previous studies, and further analyses can be found elsewhere [34,40–42,56,57].

# 4. RESULTS AND DISCUSSIONS

## 4.1 PHYSICAL PROPERTIES OF MATERIALS

To determine the degree of porosity loss upon PEI impregnation, the $N_2$ physisorption isotherms were measured and displayed in Figure 2. For all materials, the PEI incorporation significantly affected the $N_2$ adsorption, resulting in sequentially diminished uptakes as amine loading increased. As shown in Figure 2a, all MIL-101 adsorbents exhibited type I isotherm, indicated by a sharp initial uptake of $N_2$ at low pressure, followed by a gradual increase at higher relative pressures, characteristic of microporous materials. The obtained isotherms are consistent with literature results reported for bare MIL-101 and PEI-MIL-101 [25,48]. For alumina samples on the other hand (Figure 2b), a typical type IV isotherm showing significant $N_2$ uptake at relative pressures greater than 0.8 was observed, which indicated the predominant mesoporous nature of alumina with H1 hysteresis loop. [58] Upon PEI-impregnation, $N_2$ physisorption decreases with amine loading, indicating successful impregnation of PEI into the mesopores. The mesoporosity of the PEI-alumina was maintained, indicated by the H1 hysteresis present in all PEI-alumina isotherms. These isotherms are consistent with literature at comparable amine loadings [27,59]. Shown in Figure 2c, the UVM-7 silica curve shows two defined adsorption steps, confirming bimodal porosity [31,32]. The first adsorption step, at intermediate relative pressure, is characteristic of a type IV isotherm and is due to capillary condensation of $N_2$ inside of homogenous intra-nanoparticle mesopores. The second adsorption step corresponds to the filling of large mesopores. The H4 hysteresis shown upon desorption at moderate relative pressures further indicates the presence of

bimodal pores. After PEI functionalization, this region is significantly reduced, indicating a loss in bimodal porosity upon amine impregnation as the isotherms take on a more typical type IV shape representative of many mesoporous silicas [60–62].

The textural properties of the bare and amine-functionalized adsorbents determined from the $N_2$ isotherms, along with the amine loadings of the materials, are presented in Table 1. As expected, the incorporation of amines reduced the surface areas and pore volumes of the materials, indicating the successful loading of PEI into the pores. Upon 20, 35, and 50 wt. % PEI impregnation, amine loadings of 2.9, 4.1, and 8.2 mmol N/g were achieved for PEI-MIL-101, respectively, 3.2, 4.1, 7.0 mmol N/g were achieved for PEI-Alumina, respectively, and 3.9, 5.9, 8.0 mmol N/g were achieved for PEI-Silica, respectively.

These loadings are concordant, allowing for direct comparisons between PEI-adsorbents. Upon impregnation of the bare MIL-101, the surface area decreased significantly from 2400 to 900, 800, and 600 $m^2/g$, respectively, for MIL-101-20, MIL-101-35, and MIL-101-50, and the pore volume dropped from 1.20 to 0.60, 0.47, and 0.40 $cm^3/g$, respectively, due to increased amine loadings. Alumina saw a decrease in surface area from 250 to 170, 140, and 65 $m^2/g$, respectively, for Alumina, Alumina-20, Alumina-35, and Alumina-50, and a decrease in pore volume from 1.20 to 0.31 $cm^3/g$. For UVM-7 silica, a decrease in surface area from 1200 to 640, 500, and 120 $m^2/g$, respectively, was noted for Silica, Silica-20, Silica-35, and Silica-50 and a decrease from 1.15 to 0.64 $cm^3/g$ in pore volume.

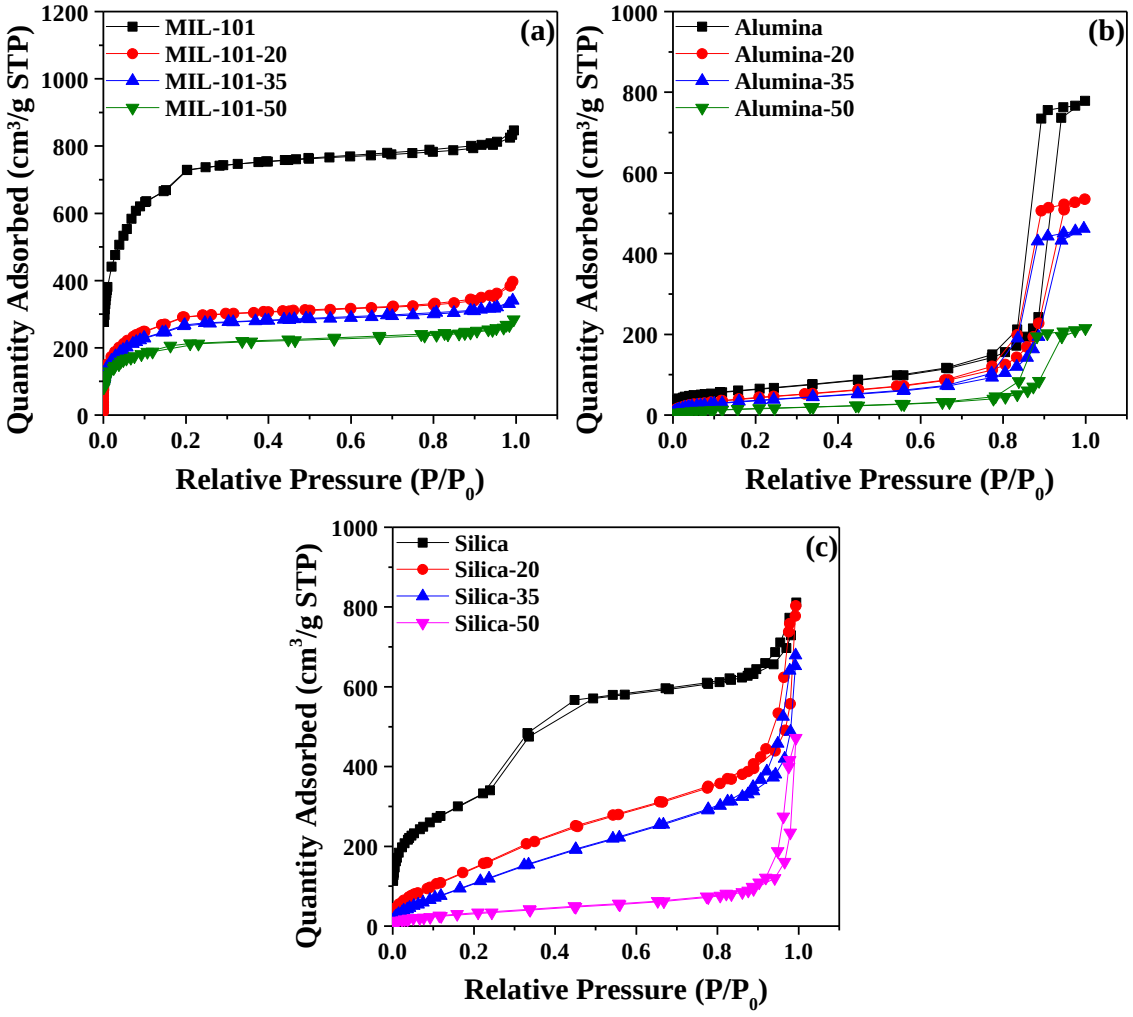


Figure 2. $N_2$ physisorption isotherms for (a) MIL-101, (b) alumina, and (c) silica based adsorbents.

Upon examination of the textural properties of Silica-35 to Silica-50, we see a large drop in the surface area from 500 to 120 $m^2/g$ but a smaller decrease in pore volume (0.86 to 0.64 $cm^3/g$). This could be the result of complete filling of small mesopores but incomplete filling of the large mesopores, as supported by the type IV shape of the Silica-50 isotherm (Figure 2c), which exhibited a substantial $N_2$ uptake at $P/P_0 > 0.9$ and a hysteresis upon desorption that is consistent with the presence of these large mesopores[58].

Table 1. Physical Properties of Bare and Amine-Functionalized Adsorbents.

| **Material** | **$S_{BET}$ ($m^3$/g)** | **$V_P$ ($cm^3$/g)** | **$d_P$ (nm)** | **Amine Loading (mmol N/g)** |
|---|---|---|---|---|
| MIL-101 | 2400 | 1.20 | 2.3 | - |
| MIL-101-20 | 900 | 0.60 | 1.3 | 2.9 |
| MIL-101-35 | 800 | 0.47 | 1.9 | 4.1 |
| MIL-101-50 | 600 | 0.40 | 1.9 | 8.2 |
| Alumina | 250 | 1.20 | 14 | - |
| Alumina-20 | 170 | 0.84 | 13 | 3.2 |
| Alumina-35 | 140 | 0.70 | 13 | 4.1 |
| Alumina-50 | 65 | 0.31 | 13 | 7.0 |
| Silica | 1200 | 1.15 | 2.9 | - |
| Silica-20 | 640 | 1.10 | 2.6 | 3.9 |
| Silica-35 | 500 | 0.86 | 2.6 | 5.9 |
| Silica-50 | 120 | 0.64 | 3.0 | 8.0 |

## 4.2 ADSORPTION ISOTHERM MEASUREMENTS

For MIL-101 and alumina based materials, the maximum $CO_2$ uptake at 25 °C and 1 bar were extracted from the equilibrium adsorption isotherms and are shown in Table 2. The silica adsorbents were tested at a range of temperatures (25-75 °C) and are recorded in Table 3. The $CO_2$ adsorption isotherms for the MIL-101 and PEI-impregnated MIL-101 adsorbents (Figure 3a) exhibit comparable uptakes to those found in literature at similar amine loadings [48,63]. At 1 bar, the bare MIL-101 reached a capacity of 1.60 mmol/g. Upon the addition of PEI, the maximum adsorption capacity of MIL-101-20 and MIL-101-35 increased by 25 % and 94 %, respectively, over that of the bare support. In regions of low loadings (0.10 bar $CO_2$), we observe up to a five-fold increase in uptake for these materials due the influence of strong interactions between $CO_2$ and the amine groups within the MOF pores. Interestingly, the maximum uptake of $CO_2$ between

MIL-101-35 and MIL-101-50 decreased by 10 %. This is likely due to blockages occurring within the micropores, resulting in diffusional resistances and limitations towards the accessibility of adsorption active sites. This trend agrees with our other work which shows that MIL-101 loaded with 85 wt. % PEI exhibits a further diminished capacity of 2.1 mmol/g at 1 bar [48].

The adsorption isotherms for the alumina and PEI-alumina adsorbents are shown in Figure 3b. The bare alumina used in this study does not exhibit an affinity for $CO_2$, but rather serves as a durable support that can facilitate the impregnation and even dispersion of large quantities of PEI into its mesoporous network due to its large pore diameter (14 nm). The resultant $CO_2$ isotherms for these PEI-Alumina adsorbents, exhibiting high initial uptakes for each isotherm in the region of low loading, exemplify $CO_2$ capture solely by chemical adsorption. At 1 bar, the maximum $CO_2$ uptake for Alumina-20, Alumina-35, and Alumina-50 was 0.41 mmol/g, 0.90 mmol/g, and 1.42 mmol/g, respectively.

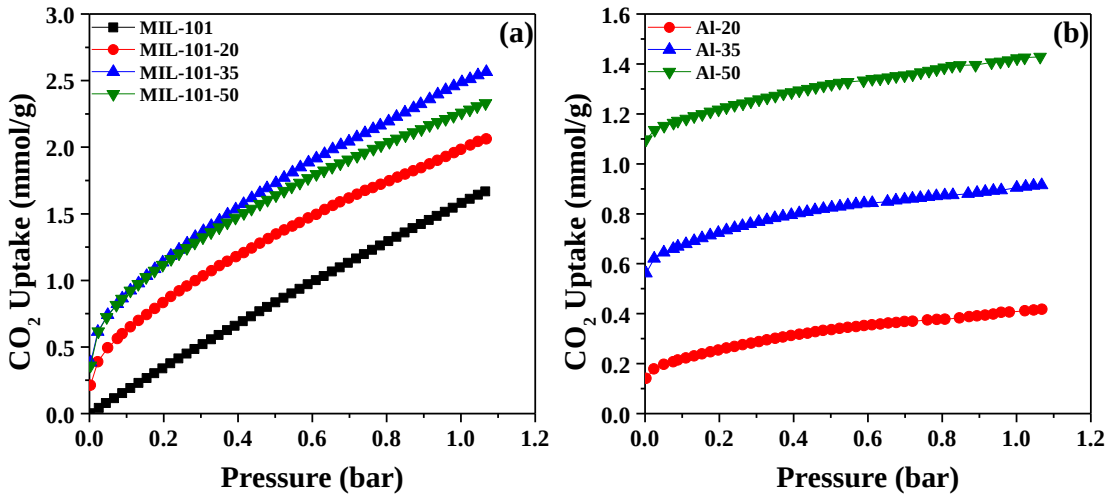


Figure 3. $CO_2$ adsorption isotherms of (a) MIL-101, MIL-101-20, MIL-101-35, and MIL-101-50 and (b) Alumina-20, Alumina-35, and Alumina-50 at 25 °C and 1 bar.

The $CO_2$ adsorption isotherms for the silica and PEI-impregnated silica adsorbents were taken at 25 °C, 50 °C, and 75 °C and are shown in Figure 4. To our knowledge, this is the first time this silica type has been functionalized with PEI and tested for $CO_2$ uptake over a range of temperatures. As expected, the adsorption capacity of the bare silica support decreased with increasing temperature (Table 3 and Figure 4a) and the PEI-silica capacities exhibited the following trend: Silica < Silica-20 < Silica-35 < Silica-50 at each temperature profile (Figure S2, Supplementary Information). From examination of Figure S2, Supplementary Information, it is clear that these isotherms exhibit contributing effects of chemical and physical adsorption mechanisms. In the low loadings regions, chemical adsorption is pronounced, and, as expected, shows a greater initial uptake (Figure S2c, Supplementary Information) at 75 °C as opposed to that observed at 25 °C (Figure S2a, Supplementary Information) [17]. However, as the partial pressure of $CO_2$ is increased, physical adsorption becomes more pronounced [64,65].

However, several interesting trends were revealed upon the comparison of $CO_2$ uptakes of the individual PEI-silica adsorbents (Figure 4). Examination of Figure 4b shows that for Silica-20, $CO_2$ uptake successively decreased at temperature increases. Initially, this appears to be in contrast with other investigations that have shown PEI-silica adsorbents exhibiting enhanced capacities at higher temperatures [17]. However, from the observed surface area and pore volume (640 $m^2/g$ and 1.10 $cm^3/g$, respectively), we know this trend is due to thermodynamic effects resulting from the low coverage of PEI in the mesopores. Surface sites on the silica support are more accessible in the pores, resulting in less $CO_2$ diffusion into the PEI [13,25]. Figure 4c shows that the adsorption capacities at 1 bar are essentially equivalent at all temperatures for Silica-35. From this,

we see the competing regimes of chemical and physical adsorption. Figure 4d shows enhanced capacities as the temperature is increased for Silica-50. This is in line other PEI-silica studies. The available actives sites on the silica surface are reduced at higher PEI loadings, and, as temperature increases, the PEI polymer becomes more flexible and exposes more active sites for $CO_2$ capture. This shows an important dependency on the effect of PEI-loadings for UVM-7 silica, and the effects of thermodynamic versus kinetic control on $CO_2$ adsorption.

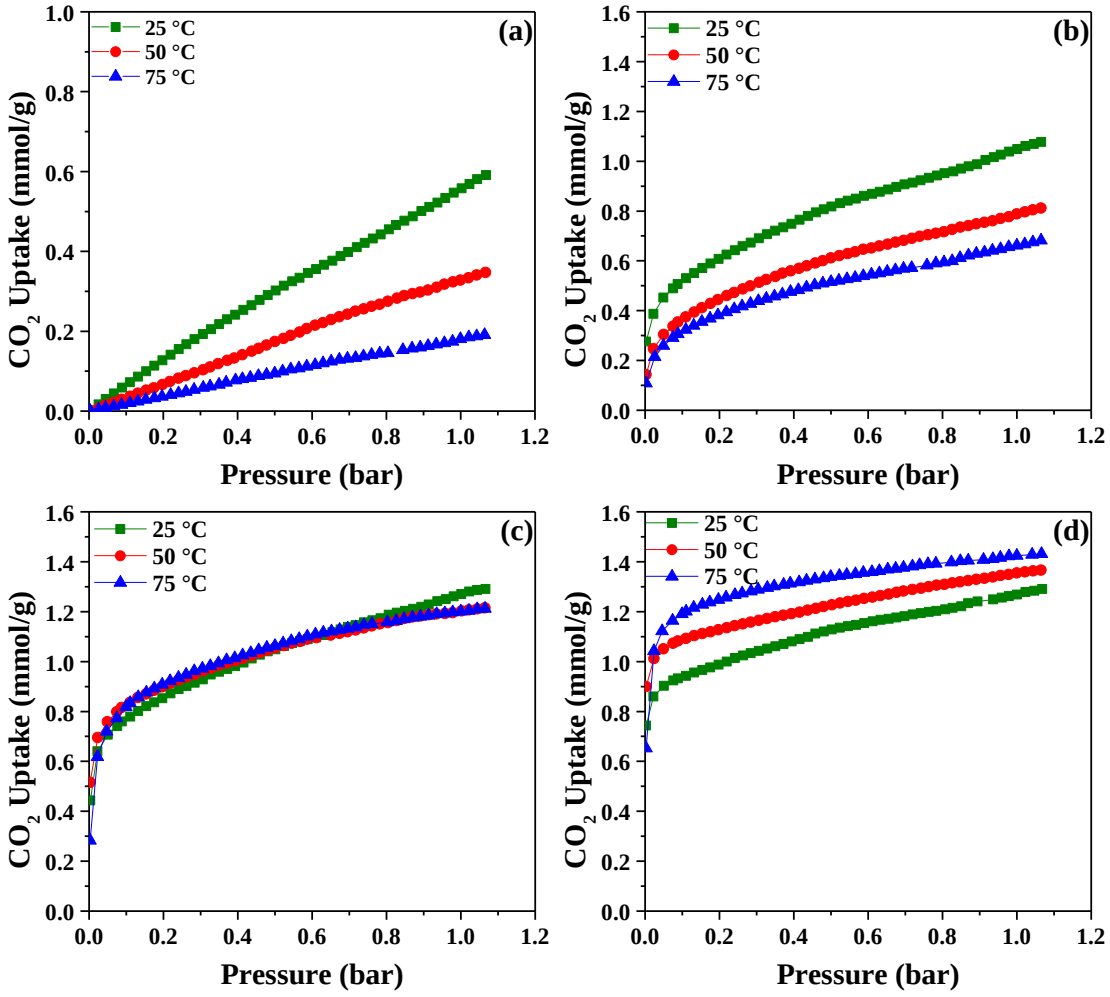


Figure 4. $CO_2$ adsorption isotherms at 25 °C, 50 °C, and 75 °C and 1 bar for (a) Silica, (b) Silica-20, (c) Silica-35, and (d) Silica-50.

From the Silica and PEI-Silica isotherms, the isosteric heats of adsorption, $-\Delta H$, were calculated by applying the Clausius-Clapeyron Equation:

$$\left[\frac{\partial \ln P}{\partial (1/T)}\right]_q = \frac{-\Delta H}{R} \tag{6}$$

where $P$ is the pressure, $T$ is the temperature, $q$ is the amount adsorbed, and $R$ is the universal gas constant. At zero coverage, the heats of adsorption values for silica, Silica-20, Silica-35, and Silica-50 were found to be 21, 48, 54, and 64 kJ/mol, respectively. As expected, $-\Delta H$ increased with amine loadings and exhibits values comparable to other PEI-functionalized mesoporous silicas outlined in literature [66,67]. The high heats of adsorption at the onset of $CO_2$ uptake further demonstrates the presence of chemical adsorption between $CO_2$ and amine active sites [64].

Table 2. $CO_2$ uptake and PEI amine efficiency at 25 °C and 1 bar, and Henry's Constant at 25 °C.

| **Material** | **$CO_2$ Uptake (mmol/g)** | **Amine Efficiency (mol $CO_2$ /mol N)** | ***H*** **(mmol/gbar)** |
|---|---|---|---|
| MIL-101 | 1.58 | - | 1.7 |
| MIL-101-20 | 1.98 | 0.68 | 5.0 |
| MIL-101-35 | 2.50 | 0.61 | 9.0 |
| MIL-101-50 | 2.25 | 0.27 | 8.6 |
| Alumina | - | - | - |
| Alumina-20 | 0.41 | 0.13 | 8.6 |
| Alumina-35 | 0.90 | 0.22 | 900 |
| Alumina-50 | 1.42 | 0.20 | 26,000 |

Amine efficiencies were further calculated at 1 bar for all PEI-impregnated materials. Amine efficiency is defined as the number of moles of $CO_2$ captured per mole of amine and, for PEI, has a maximum theoretical efficiency of 0.5. The branched PEI used here consists of 44 % primary amine groups, 33 % secondary, and 23 % tertiary. Under dry conditions, tertiary amines cannot react with $CO_2$, reducing the maximum amine efficiency for these materials to 0.385 [26,68]. The amine efficiencies of the PEI-MIL-101 composites revealed unexpected results. MIL-101-20 and MIL-101-35 achieved amine efficiencies of 0.68 and 0.61, respectively. This same phenomena has been reported elsewhere for PEI-MIL-101 composites [63]. Recently, Planas et al. [69] reported a new mechanism for $CO_2$ adsorption onto amine groups, suggesting that two amine groups can simultaneously capture two $CO_2$ molecules. This would increase the theoretical amine efficiency to 1.0, and we believe that our experimental results collaborate with this new finding. Alumina-35 yielded the highest amine efficiency at 1 bar (0.22 mol $CO_2$/mol N), demonstrating that Alumina-35 provided the easiest accessibility of available amine sites for $CO_2$ adsorption. As expected, PEI-Silica saw a general increase in amine efficiency with temperature. This is best explained by the re-arrangement of PEI within the pores at higher temperatures, resulting in easier $CO_2$ accessibility to amine active sites [21,70]. Similar to PEI-Alumina, Silica-35 exhibited the highest amine efficiencies at all three temperatures.

Moreover, at regions of low loadings the Henry's constants, *H*, were calculated according to a *Virial* Plot:

$$\left[\frac{\partial \ln P}{\partial (1/T)}\right]_q = \frac{-\Delta H}{R} \quad (5)$$

where $P$ is the pressure, $q$ is the amount adsorbed, and $A_1$ is a virial constant. $H$ provides important characterization of the intrinsic affinity between sorbent and adsorbent, and is commonly used to provide qualitative comparisons of adsorbent affinities.

Table 3. $CO_2$ uptake, PEI amine efficiency, and Henry's Constant at 25 °C, 50 °C, and 75 °C and 1 bar.

| **Material** | **Temp (°C)** | **$CO_2$ Uptake (mmol/g)** | **Amine Efficiency (mol $CO_2$ /mol N)** | ***H* (mmol/gbar)** |
|---|---|---|---|---|
| Silica | 25 | 0.56 | - | 0.7 |
| Silica-20 | | 1.05 | 0.14 | 12 |
| Silica-35 | | 1.27 | 0.18 | 61 |
| Silica-50 | | 1.27 | 0.16 | 740 |
| Silica | 50 | 0.33 | - | 0.3 |
| Silica-20 | | 0.79 | 0.20 | 30 |
| Silica-35 | | 1.20 | 0.21 | 3,300 |
| Silica-50 | | 1.35 | 0.17 | 730,000 |
| Silica | 75 | 0.18 | - | 0.2 |
| Silica-20 | | 0.66 | 0.17 | 42 |
| Silica-35 | | 1.20 | 0.20 | 1,200 |
| Silica-50 | | 1.42 | 0.18 | 1,400,000 |

From examination of the $H$ values for MIL-101 and PEI-MIL-101 (Table 2), we observe that even upon the addition of PEI, the Henry's constants are still considerably less than those found for the benchmark materials zeolite 5A or 13X [71], indicating PEI-MIL-101 exhibits a weaker affinity towards $CO_2$ at low surface coverage. PEI-alumina materials, however, show a one hundred-fold increase in $H$ with each additional PEI

loading (Table 2), representing them as promising adsorbents for direct air capture applications. PEI-Silica exhibited enhanced *H* values at higher temperatures and, like PEI-Alumina, shows a one hundred-fold increase in *H* with each amine loadings at 50 and 75 °C (Table 3). Silica-50 demonstrated exceptional *H* values at all temperature profiles, illustrating the effect of PEI-functionalization on the initial adsorption uptake (Figure 4d).

### 4.3 DIFFUSION KINETICS OF $CO_2$ IN MIL-101 BASED ADSORBENTS

ZLC technique was used in order to determine for the diffusion kinetics for MIL-101 and PEI-MIL-101 at 25 °C. Three flow rates (5.0 mL/min, 7.5 mL/min, and 10 mL/min) were used in order to characterize $D_e/R^2$ for each adsorbent, and *L* was optimized in order to ensure each run was kinetically controlled. Figure 5 illustrates the resultant desorption curves, and Table 4 provides the average $D_c/r_c^2$ for the bare MIL-101 and the average $D_e/R^2$ of each PEI-MIL-101 material, as well as the *L* parameters. The individual diffusion time constants derived at each flow rate are provided in Table S1, Supporting Information.

Desorption of $CO_2$ from the bare MIL-101 (Figure 5a) was relatively quick, exhibiting a $D_c/r_c^2 = 0.00227\ s^{-1}$, and reaching $C/C_0 = 0.001$ in under 200 s at 5 mL/min. To our knowledge, this is the first time $D_c/r_c^2$ has been reported for $CO_2$ in this material. Zhang et al. [72] characterized diffusion values of $CO_2$ through MIL-101, however, MIL-101 can express a variety of crystalline radius sizes, making comparison between these works inappropriate. Additionally, the desorption time for MIL-101 exhibited the same time-scale as adsorption. This is rather uncommon for many adsorption processes which

generally exhibit faster adsorption and slower desorption kinetics [73], making this a promising material for a myriad of cyclic processes.

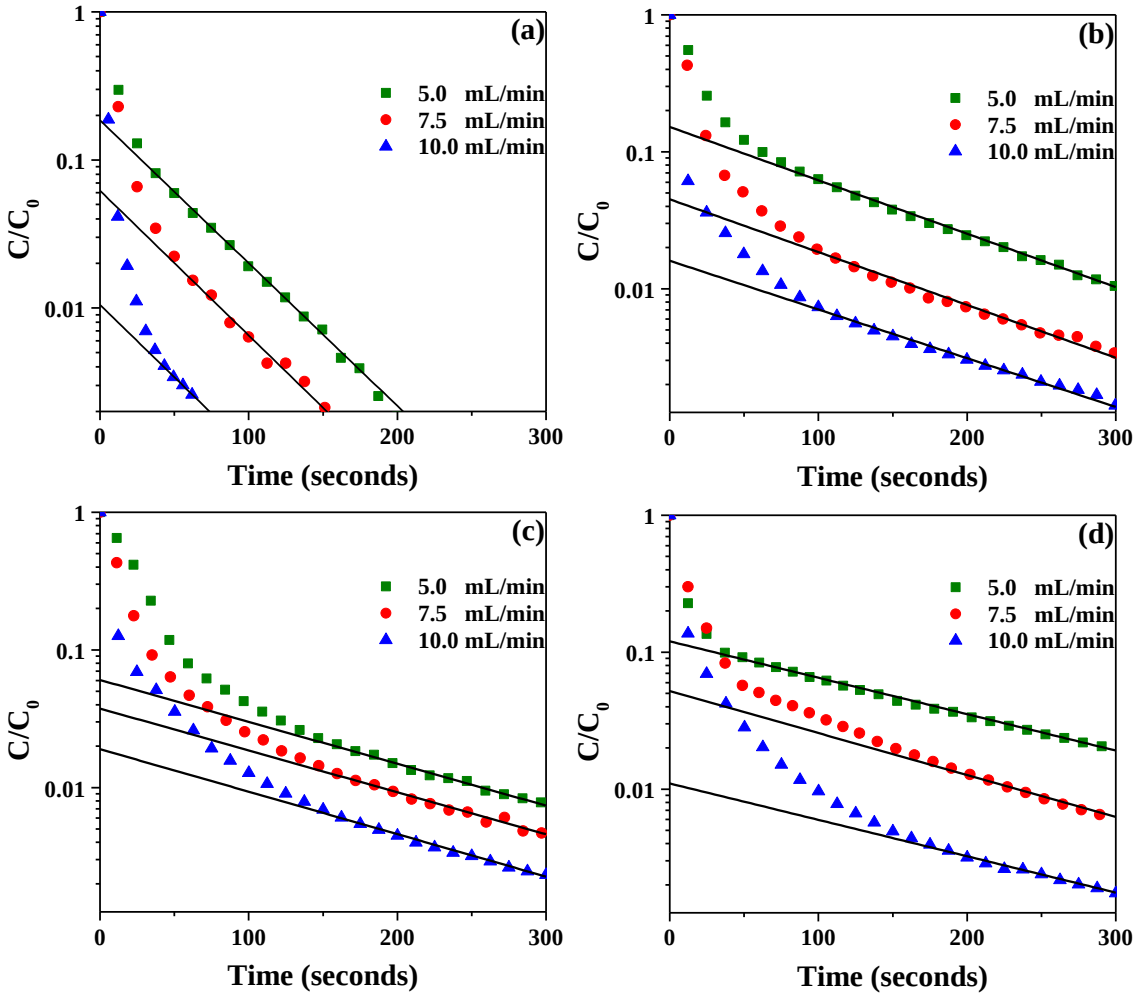


Figure 5. ZLC desorption curves of $CO_2$ at 25 °C for (a) MIL-101, (b) MIL-101-20, (c) MIL-101-35, and (d) MIL-101-50.

Figures 5b-d illustrate desorption of $CO_2$ from MIL-101 upon the addition of PEI into the micropores. From the diffusivity values tabulated in Table 4, the $D_e/R^2$ of MIL-101-20, MIL-101-35, and MIL-101-50 decreased by 62 %, 69%, and 73 %, respectively, to the $D_c/r_c^2$ of the MIL-101 support. The dramatic decrease in diffusivity upon the

addition of 20 wt. % PEI illustrates the introduction of diffusional resistances upon the loading of bulky PEI into the MOF micropores. The PEI branches both chemically interact with the $CO_2$ and, at low temperatures (25 °C) bars movement out of the pores, resulting in slower kinetics and increased desorption times. As PEI loadings were increased to 35 and 50 wt. %, the diffusivity values further decreased due to additional blockages by PEI within the pores.

Table 4. Diffusivity values for MIL-101 and PEI-MIL-101 at 25 °C.

| **Material** | **$D_c/r_c^2 \times 10^3$ ($s^{-1}$)** | **$D_e/R^2 \times 10^3$ ($s^{-1}$)** | **L** |
|---|---|---|---|
| MIL-101 | 2.27 | - | 11-190 |
| MIL-101-20 | - | 0.87 | 12-120 |
| MIL-101-35 | - | 0.71 | 34-100 |
| MIL-101-50 | - | 0.62 | 17-170 |

The ZLC desorption curves for the PEI-MIL-101 adsorbents are uniquely different from the bare MOF support, and illustrate the complex diffusional kinetics of PEI-impregnated materials [51]. Upon examination of Figures 5b-d, we see that flow rate plays a crucial role at the beginning stages of desorption. Increasing the purge rate results in a longer region of non-linearity, and, this becomes more pronounced as the amine loading is increased. This is likely a consequence of the differing rate-limiting mechanisms for mass transfer between physical and chemical adsorption. Physical and chemical sorption mechanisms operate independently and thus would influence the observed desorption curve. Bare MIL-101 exhibits a substantial $CO_2$ uptake, signifying that for PEI-MIL-101 materials, $CO_2$ would adsorb on both physical and chemical active

sites. Upon desorption, due to its weaker affinity, the physically-adsorbed $CO_2$ species would diffuse first from the adsorbent, and, dependent upon the magnitude of the purge flow rate, would result in initial desorption curves of varying shapes [55,74].

## 4.4 DIFFUSION KINETICS OF $CO_2$ IN γ-ALUMINA-BASED ADSORBENTS

The Alumina and PEI-Alumina diffusion kinetics for $CO_2$ were examined at 25 °C. ZLC desorption curves are illustrated in Figure 6 and the $D_e/R^2$ averages are shown in Table 5 (diffusivities gathered at each run are tabulated in Table S2, Supporting Information). Three different purge flow rates were investigated in regions of kinetic control (L > 10) in order to ensure the acquirement of accurate diffusion time constants for each material. The resultant desorption curves for the PEI-Alumina materials exhibit similar profiles as those shown by PEI-MIL-101, further demonstrating $CO_2$ diffusion out of the branched PEI as the rate-limiting mass transfer mechanism upon $CO_2$ desorption for these materials.

The alumina support (Figure 6a) exhibited a $D_c/r_c^2$ of 0.00125 $s^{-1}$. While the alumina used in this study does not itself possess an intrinsic affinity for $CO_2$, ZLC desorption was used to in order to map the path of diffusivity of $CO_2$ through the mesopores. Figure 6b-d illustrate desorption curves for Alumina-20, Alumina-35, and Alumina-50, which yielded $D_e/R^2$ values of 0.00079 $s^{-1}$, 0.00074 $s^{-1}$, and 0.00069 $s^{-1}$, respectively. As expected, the diffusion time constants for each PEI-Alumina decreased by 37 %, 41 %, and 45 %, respectively, compared to the alumina support due to the introduction of kinetic barriers to mass transfer in the mesopores resulting from the impregnation of branched PEI. Additionally, the reduction in $D_e/R^2$ values across the

PEI-Alumina is quite consistent, showing a decrease of 5 x $10^{-5}$ $s^{-1}$ upon 15 wt. % loadings. This quite nicely demonstrates that, for mesoporous supports that do not exhibit an intrinsic affinity for $CO_2$, there exists a linear relationship between diffusivity and PEI loading. This trend could be used to effectively approximate the diffusivity of PEI-Alumina over a range of amine loadings, provided that the pores are not overfilled.

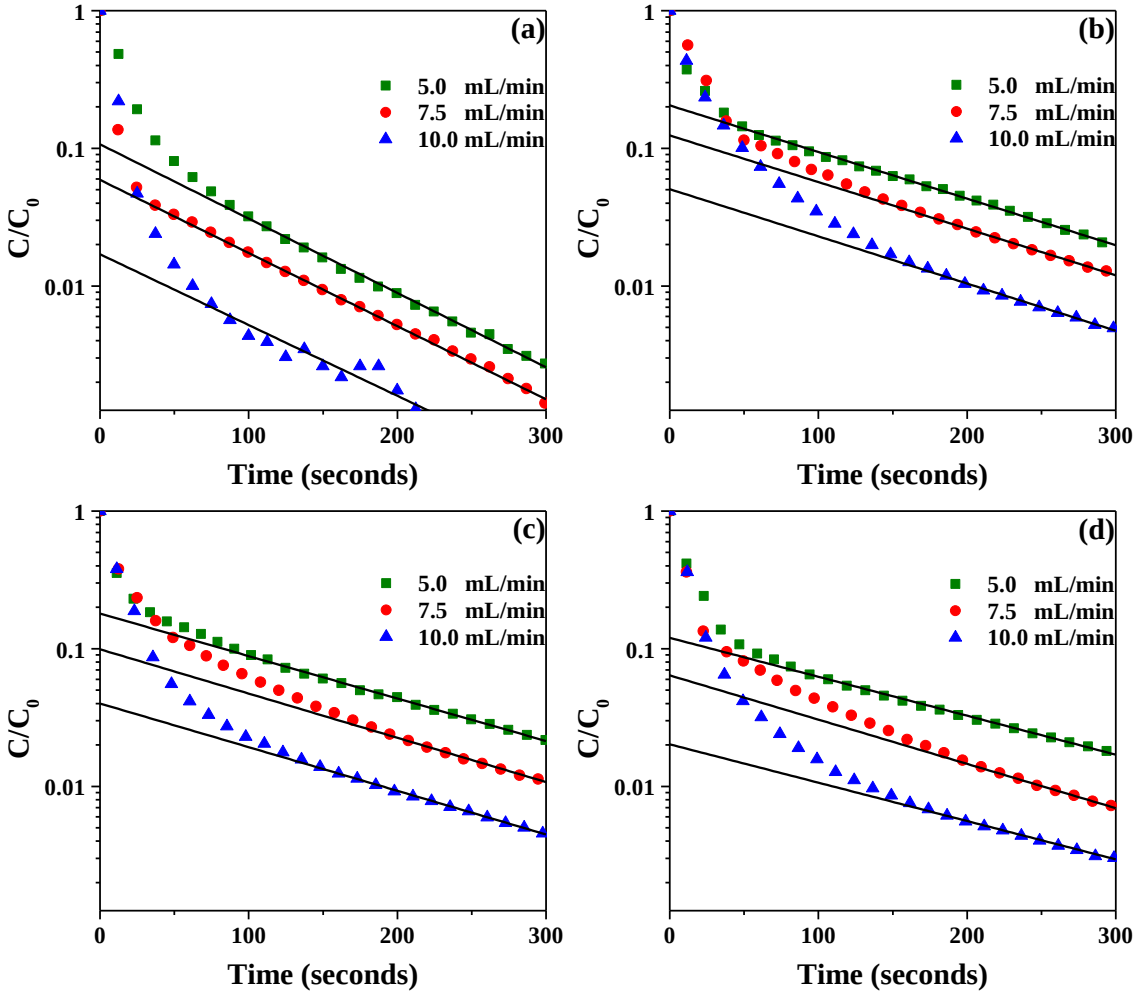


Figure 6. ZLC desorption curves of $CO_2$ at 25 °C for (a) Alumina, (b) Alumina-20, (c) Alumina-35, and (d) Alumina-50.

Comparison of the decrease in diffusivity between the support and PEI-functionalized adsorbents of MIL-101 and alumina demonstrates the important effect of mesoporous versus microporous support structures on $CO_2$ diffusional resistances. At 20 wt. % PEI loading, the diffusivity of MIL-101-20 and Alumina-20 decreased by 62 % and 37 %, respectively. The pore diameter of the support has been identified as the most important factor regarding optimization of $CO_2$ uptake and kinetics [17]. The mesoporous alumina support exhibits a superior pore diameter (14 nm) over that of the MIL-101 (2.3 nm) and can accommodate the impregnation of larger quantities of amines and allow for a more even distribution of PEI within the pore network, resulting in improved diffusion kinetics [30,75–78].

Table 5. Diffusivity values for Alumina and PEI-Alumina at 25 °C.

| **Material** | **$D_c/r_c^2$ x $10^3$ ($s^{-1}$)** | **$D_e/R^2$ x $10^3$ ($s^{-1}$)** | **L** |
|---|---|---|---|
| Alumina | 1.25 | - | 19-100 |
| Alumina-20 | - | 0.79 | 12-120 |
| Alumina-35 | - | 0.74 | 34-100 |
| Alumina-50 | - | 0.69 | 17-170 |

## 4.5 DIFFUSION KINETICS OF $CO_2$ IN SILICA-BASED ADSORBENTS

The $CO_2$ diffusion time constants were examined for silica and PEI-silica materials at 25, 50, and 75 °C. The desorption curves for these materials at these temperatures are illustrated in Figures 7-9, respectively, and are tabulated in Table 6 in order to provide comparisons between the kinetic rates taken for each material at the different temperature conditions. Three purge flow rates were investigated and held

constant to those used for the MIL-101 and alumina materials in order to ensure consistency amongst all tested adsorbents.

The observed ZLC desorption curves for these PEI-impregnated silicas revealed an interesting trend that is not observable in the ZLC curves of the silica support. It is clear from the desorption curves (Figures 7-9) that there exist two distinct regions of mass transfer control occurring at different sorption times. The first region occurs following the immediate region of desorption and yielded a linear long-time asymptote that lasted between 200 – 300 s depending on amine-loading and the temperature of the trial. Upon examination of Figures 7-9, this region is most pronounced at 25 °C and lessens in longevity at higher temperatures. The second region of mass transfer control occurs at a longer sorption time (> 300 s) and remains the controlling mass transfer rate until complete desorption was achieved for all PEI-Silica trials. In Figures 7-9, the linear fit for $D_s/R^2$ is denoted as a dotted line and the fit for $D_e/R^2$ is denoted as a solid line.

Previous studies have found that $CO_2$ adsorption over PEI-impregnated mesoporous silicas is a two-step rate-limiting process [51,52,54]. The first rate-limiting step is surface uptake where adsorption occurs dominantly on the support active sites or near the surface layers of the PEI. Upon saturation, the second step then becomes rate-limiting and involves $CO_2$ diffusion into the bulk of the PEI. From this, upon desorption, we assume the initial rate limiting step is surface diffusion, which has been denoted in Table 6 as $D_s/R^2$, and the second is the diffusion of $CO_2$ out of the PEI, or effective diffusion ($D_e/R^2$), of the aminosilicas. Due to its much longer sorption time, $D_e/R^2$ is the primary rate limiting step to mass transfer and therefore is the focus of these materials.

The $D_s/R^2$ and $D_e/R^2$ derived for each individual trial at 25, 50, and 75 °C are listed in Tables S3-S5, Supporting Information.

Table 6. Surface and effective diffusivity values for Silica and PEI-Silica at 25, 50, and 75 °C.

| **Material** | **25 °C** | | **50 °C** | | **75 °C** | | |
|---|---|---|---|---|---|---|---|
| | **$D_s/R^2$ ($s^{-1}$)** | **$D_e/R^2$ ($s^{-1}$)** | **$D_s/R^2$ ($s^{-1}$)** | **$D_e/R^2$ ($s^{-1}$)** | **$D_s/R^2$ ($s^{-1}$)** | **$D_e/R^2$ ($s^{-1}$)** | **$E_a$ (kJ/mol)** |
| Silica | - | 1.31 | - | 1.69 | - | 1.84 | 5.9 |
| Silica-20 | 0.78 | 0.31 | 0.85 | 0.40 | 0.91 | 0.49 | 7.3 |
| Silica-35 | 0.76 | 0.27 | 0.78 | 0.38 | 0.90 | 0.45 | 8.9 |
| Silica-50 | 0.73 | 0.20 | 0.74 | 0.34 | 0.87 | 0.40 | 12 |

As expected, a higher $D_e/R^2$ is observed for each PEI-silica as the temperature is increased. This agrees well with work reported by Gargiulo et al. [28], which, using the ZLC technique, observed an enhancement in the diffusion time constant with temperature over PEI-impregnated SBA-15 silica. The $D_e/R^2$ for Silica-20 increased by 0.00031 $s^{-1}$, 0.00040 $s^{-1}$, and 0.00049 $s^{-1}$, the $D_e/R^2$ for Silica-35 increased by 0.00027 $s^{-1}$, 0.00038 $s^{-1}$, and 0.00045 $s^{-1}$, and $D_e/R^2$ for Silica-50 increased by 0.00020 $s^{-1}$, 0.00034 $s^{-1}$, and 0.00040 $s^{-1}$ at 25, 50, and 75 °C, respectively. This is attributed to the enhancement of the molecular flexibility of PEI at higher temperatures. The PEI branches open and rearrange within the pores, exposing more active sites and removing barriers to diffusion, which in turn enhances the diffusivity of $CO_2$ within the amine bulk and results in higher sorption rates [21,52,54]. Additionally, the enhancement in $D_e/R^2$ for each aminosilica is relatively constant. Therefore, the activation energy, $E_a$, for each material, including the bare silica support, was determined by the Arrhenius equation from the slope of a plot of $ln\ D_e/R^2$

*vs. 1/T* (Figure S3, Supporting Information). The $E_a$ for each material is listed in Table 6. As expected, $E_a$ is lowest for the bare silica and increases sequentially with amine loading. Chemical adsorption requires a higher activation energy than physical adsorption in order to overcome the potential energy barrier [79,80]. Additionally, the low $E_a$ displayed by Silica-20, Silica-35, and Silica-50 agrees with those displayed by PEI-impregnated SBA-15 silica and indicates sorption is primarily occurring in the support mesopores [28].

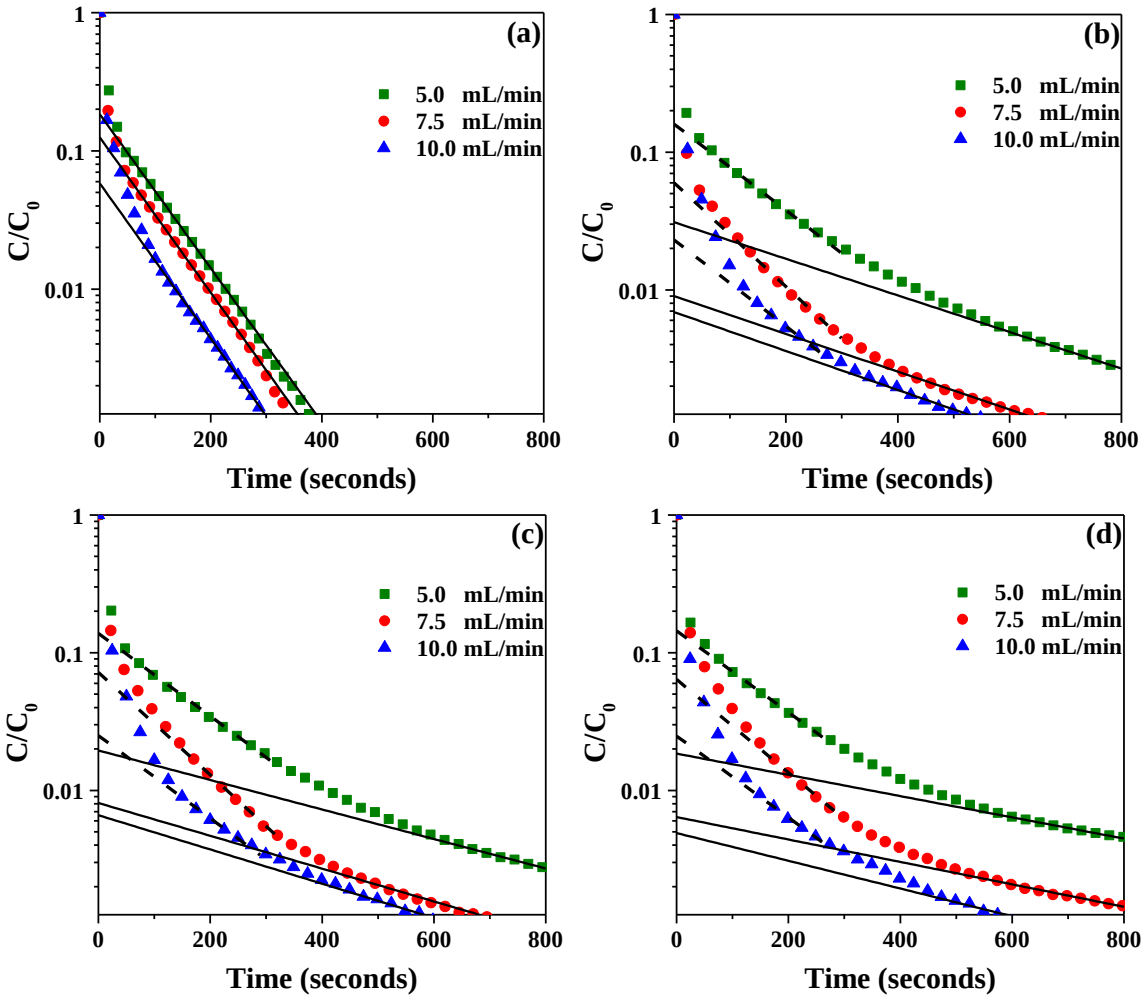


Figure 7. ZLC desorption curves of $CO_2$ at 25 °C for (a) Silica, (b) Silica-20, (c) Silica-35, and (d) Silica-50.

It has been well established that surface diffusion is a thermodynamically driven process that can be well-explained from examination of the adsorption isotherms [33]. From Table 6, we clearly see that $D_s/R^2$ increases with temperature for all three PEI-silica composites. We know that for Silica-20, from the isotherms, adsorption is controlled by thermodynamic effects (Figure 4b). Less $CO_2$ is adsorbed to Silica-20 at high temperatures which would mean that upon desorption, surface diffusion occurs more quickly as there are fewer $CO_2$ molecules occupying adsorption sites [17]. For Silica-35, while we do see an influence of chemical adsorption in the isotherms, ultimately, lower capacities are achieved at higher temperatures (Figure 4c) which would result in enhanced surface diffusion characteristics. For Silica-50, this trend be best explained from the silica support isotherms (Figure 4a). Physical and chemical adsorption are independent sorptive processes. While the capacities for Silica-50 increase overall with temperature due to chemical adsorption (Figure 4a), the physical adsorption uptake reduced. Therefore, less $CO_2$ is physically adsorbed to the silica at higher temperatures, resulting in faster surface diffusion kinetics.

At 25 °C, as expected, both $D_s/R^2$ and $D_e/R^2$ decrease with increased amine loadings. From Table 1, we know higher PEI loadings resulted in reduced pore volumes which increases the diffusion barrier of $CO_2$ out of the PEI multilayers. The bare silica showed a $D_c/r_c^2$ of 0.00131 $s^{-1}$ and reached $C/C_0 = 0.001$ in under 500 s. To our knowledge, this is the first time the diffusion time constant for $CO_2$ has been reported for UVM-7 silica. Upon the addition of 20, 35, and 50 wt. % PEI into the mesopores, the $D_e/R^2$ was reduced by 76 %, 79 %, and 85 %, respectively, compared to the bare support.

This suggests the intrusion of significant mass transfer resistances as $CO_2$ diffuses from the multilayers.

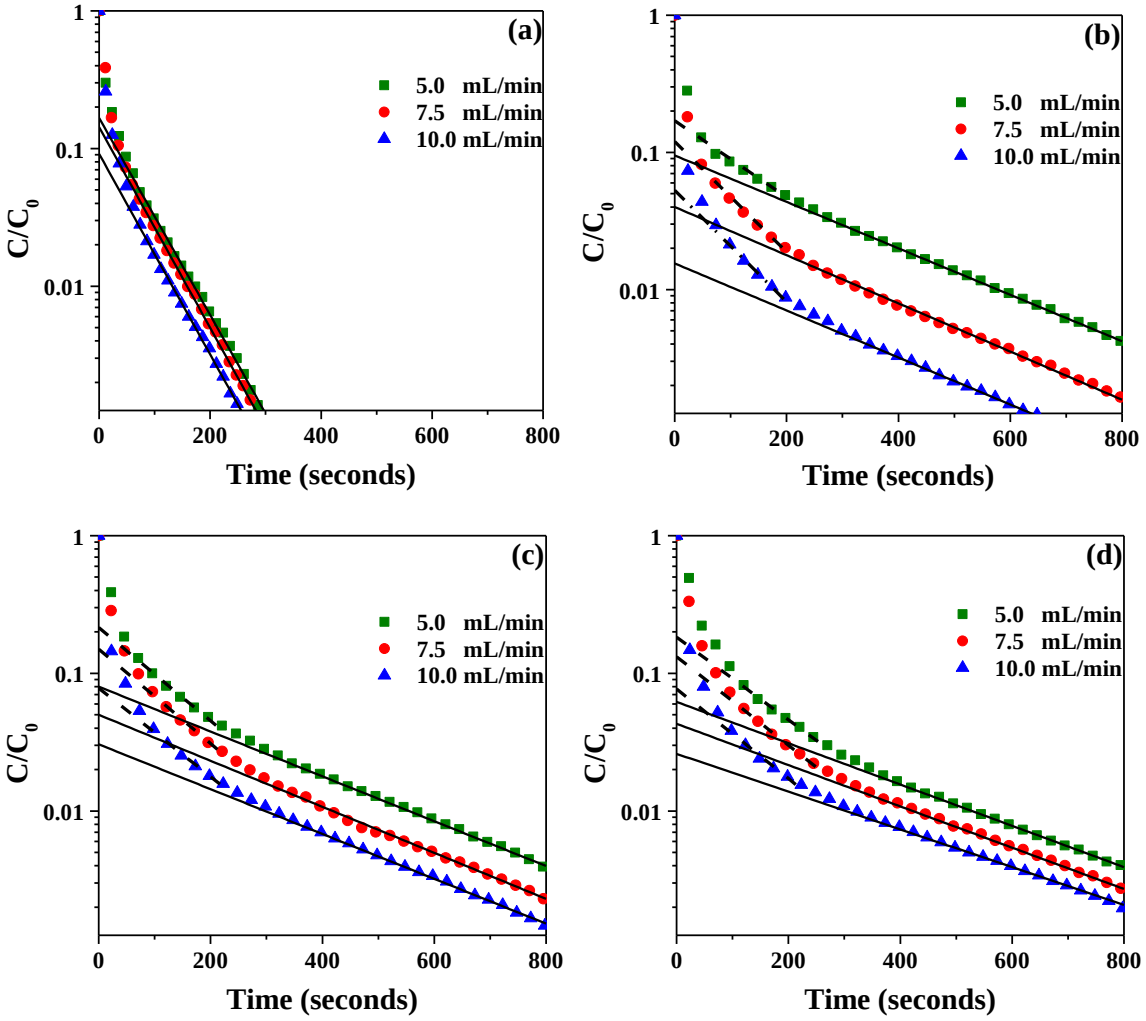


Figure 8. ZLC desorption curves of $CO_2$ at 50 °C for (a) Silica, (b) Silica-20, (c) Silica-35, and (d) Silica-50.

Additionally, upon examination of Figures 7b-d, we observe that $D_s/R^2$ is the rate-controlling mechanism for up to 300 s. This is a longer sorption time than what was observed at 50 and 75 °C. UVM-7 exhibits an intrinsic affinity for $CO_2$; in addition to

$CO_2$ residing in the multilayers, $CO_2$ is also adsorbed onto actives sites on the silica surface.

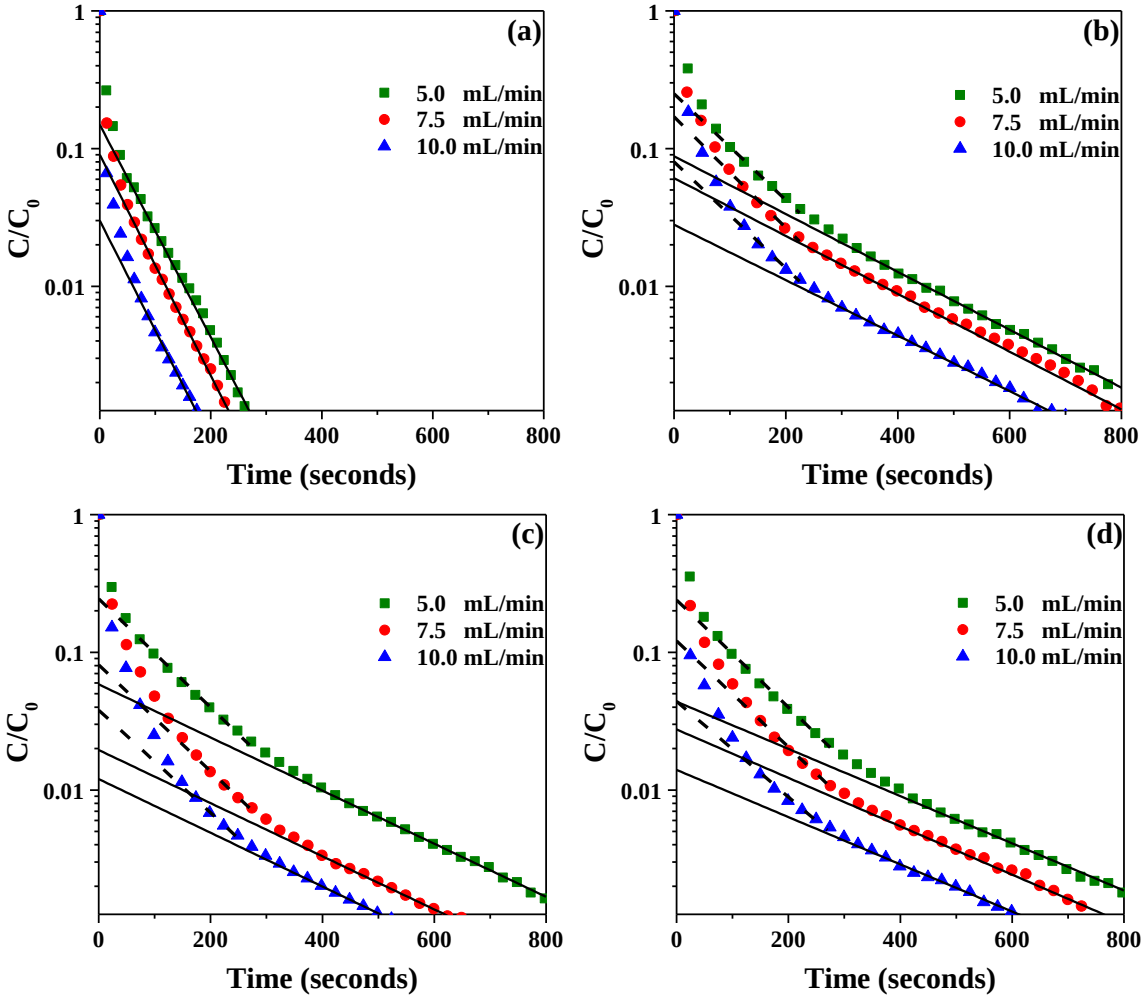


Figure 9. ZLC desorption curves of $CO_2$ at 75 °C for (a) Silica, (b) Silica-20, (c) Silica-35, and (d) Silica-50.

This would result in a longer region of surface diffusion, especially at low temperatures when physical adsorption is thermodynamically favored [81,82]. At 50 and 75 °C, again, as expected, both $D_s/R^2$ and $D_e/R^2$ decrease with increased amine loadings. The $D_e/R^2$ of the bare silica exhibited an enhancement in temperature to $D_e/R^2$ = 0.00169

$s^{-1}$ and $D_e/R^2 = 0.00169\ s^{-1}$, respectively, at 50 and 75 °C. This agrees well with established findings that diffusivity increases with temperature [28,52,54,83]. Upon the loading of PEI, at 50 °C the $D_e/R^2$ for Silica-20, Silica-35, and Silica-50 decreased by 76 %, 78 %, and 80 %, respectively, and at 75 °C $D_e/R^2$ decreased by 73 %, 76 %, and 78 %, respectively, compared to the bare silica. Upon comparison to the decreases observed at 25 °C, we see, as expected, reduced diffusional resistances at higher temperatures.

## 5. CONCLUSION

In this investigation, the diffusion of $CO_2$ was investigated in three PEI-impregnated adsorbents, namely, PEI-impregnated MIL-101, γ-alumina, and UVM-7 silica, at three different amine contents via the ZLC method at 25 °C. Experimental results indicate that for all three materials tested, as the PEI content is increased, diffusion rates are reduced. Moreover, it was found that the porosity of the support is instrumental in mitigating diffusional losses upon amine-functionalization. Microporous PEI-MIL-101 exhibited greater diffusional limitations upon amine loading compared to the mesoporous PEI- γ-alumina. PEI-impregnated UVM-7 silica was further investigated at 50 and 75 °C, where it was revealed both that PEI-impregnated mesoporous silicas exhibit two different mass transfer regimes that occur at different sorption times, and that as the temperature is increased, diffusion is enhanced. This is in accordance with molecular-basket adsorbents that see a rearrangement of bulky aminopolymers in the pores at higher temperatures, exposing more active sites and reducing diffusional

barriers. The findings of this study highlight the importance in selecting PEI-adsorbents that allow for both high working capacities and fast desorption kinetics.

## REFERENCES


1. Bindoff NL, Durack PJ, Slater A, et al. Near-term climate change: Projections and predictability. In: *Climate Change 2013 the Physical Science Basis: Working Group I Contribution to the Fifth Assessment Report of the Intergovernmental Panel on Climate Change*. Vol 9781107057. ; 2013:953-1028. doi:10.1017/CBO9781107415324.023

2. Karl TR, Trenberth KE. Modern Global Climate Change. *Science (80- )*. 2003;302(5651):1719-1723. doi:10.1126/science.1090228

3. Yang H, Xu Z, Fan M, et al. Progress in carbon dioxide separation and capture: A review. *J Environ Sci*. 2008;20(1):14-27. doi:10.1016/S1001-0742(08)60002-9

4. Al-Mamoori A, Krishnamurthy A, Rownaghi A a., Rezaei F. Carbon Capture and Utilization Update. *Energy Technol*. 2017;5(6):834-849. doi:10.1002/ente.201600747

5. Stuart Haszeldine R. Carbon capture and storage: how green can black be? *Science (80- )*. 2009;325(5948):1647-1652. doi:10.1126/science.1172246

6. Rochelle GT. Amine Scrubbing for CO2 Capture. *Science (80- )*. 2009;325(September 2009):1652-1655. doi:10.1126/science.1176731

7. Leung DYC, Caramanna G, Maroto-Valer MM. An overview of current status of carbon dioxide capture and storage technologies. *Renew Sustain Energy Rev*. 2014;39:426-443. doi:10.1016/j.rser.2014.07.093

8. Keith DW. Why capture CO2 from the atmosphere? *Science (80- )*. 2009;325(5948):1654-1655. doi:10.1126/science.1175680

9. Lackner KS. Capture of carbon dioxide from ambient air. *Eur Phys J Spec Top*. 2009;176(1):93-106. doi:10.1140/epjst/e2009-01150-3

10. Choi S, Drese JH, Jones CW. Adsorbent materials for carbon dioxide capture from large anthropogenic point sources. *ChemSusChem*. 2009. doi:10.1002/cssc.200900036

11. Bae YS, Snurr RQ. Development and evaluation of porous materials for carbon dioxide separation and capture. *Angew Chemie - Int Ed*. 2011;50(49):11586-11596. doi:10.1002/anie.201101891

12. Yu C, Huang C, Tan C. A Review of CO 2 Capture by Absorption and Adsorption. *Aerosol Air Qual Res*. 2012;(12):745-769. doi:10.4209/aaqr.2012.05.0132

13. Darunte LA, Walton KS, Sholl DS, Jones CW. CO2capture via adsorption in amine-functionalized sorbents. *Curr Opin Chem Eng*. 2016;12:82-90. doi:10.1016/j.coche.2016.03.002

14. Chen C, Kim J, Ahn WS. CO2 Capture by amine-functionalized nanoporous materials: A review. *Korean J Chem Eng*. 2014;31(11):1919-1934. doi:10.1007/s11814-014-0257-2

15. Qi G, Wang Y, Estevez L, et al. High efficiency nanocomposite sorbents for CO 2 capture based on amine-functionalized mesoporous capsules †. 2011:444-452. doi:10.1039/c0ee00213e

16. Khatri RA, Chuang SSC, Soong Y, Gray M. Thermal and chemical stability of regenerable solid amine sorbent for CO2capture. *Energy and Fuels*. 2006. doi:10.1021/ef050402y

17. Son WJ, Choi JS, Ahn WS. Adsorptive removal of carbon dioxide using polyethyleneimine-loaded mesoporous silica materials. *Microporous Mesoporous Mater*. 2008;113(1-3):31-40. doi:10.1016/j.micromeso.2007.10.049

18. Furukawa H, Ko N, Go YB, et al. Ultrahigh Porosity in Meta-Organic Frameworks. *Science (80- )*. 2010;329(5990):424. doi:10.1126/science.1192160

19. Gaikwad S, Kim SJ, Han S. CO2 capture using amine-functionalized bimetallic MIL-101 MOFs and their stability on exposure to humid air and acid gases. *Microporous Mesoporous Mater*. 2019;277(August 2018):253-260. doi:10.1016/j.micromeso.2018.11.001

20. Slater AG, Cooper AI. Function-led design of new porous materials. *Science (80- )*. 2015;348(6238):aaa8075. doi:10.1126/science.aaa8075

21. Xu X, Song C, Andrésen JM, Miller BG, Scaroni AW. Preparation and characterization of novel CO2"molecular basket" adsorbents based on polymer-modified mesoporous molecular sieve MCM-41. *Microporous Mesoporous Mater*. 2003;62(1-2):29-45. doi:10.1016/S1387-1811(03)00388-3

22. Huang HY, Yang RT, Chinn D, Munson CL. Amine-grafted MCM-48 and silica xerogel as superior sorbents for acidic gas removal from natural gas. *Ind Eng Chem Res*. 2003. doi:10.1021/ie020440u

23. Labreche Y, Fan Y, Rezaei F, Lively RP, Jones CW, Koros WJ. Poly(amide-imide)/silica supported PEI hollow fiber sorbents for postcombustion $CO_2$ capture by RTSA. *ACS Appl Mater Interfaces*. 2014;6(21):19336-19346. doi:10.1021/am505419w

24. Lin Y, Yan Q, Kong C, Chen L. Polyethyleneimine incorporated metal-organic frameworks adsorbent for highly selective CO2 capture. *Nat Sci Reports*. 2013;3:14-16. doi:10.1038/srep01859

25. Darunte LA, Oetomo AD, Walton KS, Sholl DS, Jones CW. Direct Air Capture of CO2Using Amine Functionalized MIL-101(Cr). *ACS Sustain Chem Eng*. 2016;4(10):5761-5768. doi:10.1021/acssuschemeng.6b01692

26. Chaikittisilp W, Kim HJ, Jones CW. Mesoporous alumina-supported amines as potential steam-stable adsorbents for capturing CO2 from simulated flue gas and ambient air. *Energy and Fuels*. 2011;25(11):5528-5537. doi:10.1021/ef201224v

27. Sakwa-Novak MA, Jones CW. Steam induced structural changes of a poly(ethylenimine) impregnated γ-alumina sorbent for CO2 extraction from ambient air. *ACS Appl Mater Interfaces*. 2014;6(12):9245-9255. doi:10.1021/am501500q

28. Gargiulo N, Aprea P, Caputo D, Eic M, Huang Q, Colella C. Adsorption and Diffusion of Carbon Dioxide in Polyethylenimine-Modified SBA-15 Silicas. In: *Spec. Top. Mater. Sci. Technol., [Sel. Pap. Natl. Conf.], 9th*. ; 2008:213-220. doi:10.1163/ej.9789004172241.i-420.158

29. Mello MR, Phanon D, Silveira GQ, Llewellyn PL, Ronconi CM. Amine-modified MCM-41 mesoporous silica for carbon dioxide capture. *Microporous Mesoporous Mater*. 2011;143(1):174-179. doi:10.1016/j.micromeso.2011.02.022

30. Sanz R, Calleja G, Arencibia A, Sanz-Pérez ES. CO2 adsorption on branched polyethyleneimine-impregnated mesoporous silica SBA-15. *Appl Surf Sci*. 2010;256(17):5323-5328. doi:10.1016/j.apsusc.2009.12.070

31. Pérez-Cabero M, Hungría AB, Morales JM, et al. Interconnected mesopores and high accessibility in UVM-7-like silicas. *J Nanoparticle Res*. 2012;14(8). doi:10.1007/s11051-012-1045-8

32. El Haskouri J, de Zárate DO, Guillem C, et al. Silica-based powders and monoliths with bimodal pore systems. *Chem Commun*. 2002;2(4):330-331. doi:10.1039/b110883b

33. Kärger J, Ruthven DM, Theodorou DN. *Diffusion in Nanoporous Materials.*; 2012. doi:10.1002/9783527651276

34. Eic M, Ruthven DM. A new experimental technique for measurement of intracrystalline diffusivity. *Zeolites*. 1988;8(1):40-45. doi:10.1016/S0144-2449(88)80028-9

35. Silva JAC, Rodrigues AE. Analysis of ZLC technique for diffusivity measurements in bidisperse porous adsorbent pellets. *Gas Sep Purif*. 1996. doi:10.1016/S0950-4214(96)00021-7

36. Silva JAC, Rodrigues AE. Equilibrium and Kinetics of n-Hexane Sorption in Pellets of 5A Zeolite. *AIChE J*. 1997;43(10):2524-2534. doi:10.1002/aic.690431014

37. Brandani S, Ruthven DM. Analysis of ZLC desorption curves for liquid systems. *Adsorption*. 1995;50(13):2055-2059. doi:10.1007/BF00127043

38. Brandani S, Cavalcante C, Guimaraes A, Ruthven DM. Heat Effects in ZLC Experiments. *Adsorption*. 1998;4:275-285. doi:Doi 10.1023/A:1008837801299

39. Brandani S. Effects of nonlinear equilibrium on zero length column experiments. *Chem Eng Sci*. 1998;53(15):2791-2798. doi:10.1016/S0009-2509(98)00075-X

40. Brandani S, Jama MA, Ruthven DM. ZLC measurements under non-linear conditions. *Chem Eng Sci*. 2000;55(7):1205-1212. doi:10.1016/S0009-2509(99)00411-X

41. Brandani F, Ruthven D. Measurement of Adsorption Equilibria by the Zero Length Column (ZLC) Technique Part 2: Binary Systems. *Ind Eng Chem Res*. 2003;42(7):1462-1469. doi:10.1021/ie020573f

42. Brandani F, Ruthven D, Coe CG. Measurement of adsorption equilibrium by the zero length column (ZLC) technique part 1: Single-component systems. *Ind Eng Chem Res*. 2003;42(7):1451-1461. doi:10.1021/ie020572n

43. Ruthven D, Brandani F. ZLC response for systems with surface resistance control. *Adsorption*. 2005;11(1):31-34. doi:10.1007/s10450-005-1090-z

44. Ruthven DM, Vidoni A. ZLC diffusion measurements: Combined effect of surface resistance and internal diffusion. *Chem Eng Sci*. 2012;71:1-4. doi:10.1016/j.ces.2011.11.040

45. Gatti G, Vittoni C, Costenaro D, et al. The influence of particle size of amino-functionalized MCM-41 silicas on CO2 adsorption. *Phys Chem Chem Phys*. 2017;19(43):29449-29460. doi:10.1039/c7cp05177h

46. Gatti G, Costenaro D, Vittoni C, et al. CO2adsorption on different organo-modified SBA-15 silicas: A multidisciplinary study on the effects of basic surface groups. *Phys Chem Chem Phys*. 2017;19(21):14114-14128. doi:10.1039/c6cp08048k

47. Gibson JAA, Gromov A V., Brandani S, Campbell EEB. Comparison of amine-impregnated mesoporous carbon with microporous activated carbon and 13X zeolite for biogas purification. *J Porous Mater*. 2017;24(6):1473-1479. doi:10.1007/s10934-017-0387-0

48. Lawson S, Griffin C, Rapp K, Rownaghi AA, Rezaei F. Environmental and Carbon Dioxide Issues Amine-Functionalized MIL-101 Monoliths for CO2 Removal from Enclosed Environments. *Energy and Fuels*. 2019. doi:10.1021/acs.energyfuels.8b04508

49. Al-Mamoori A, Rownaghi A a., Rezaei F. Combined Capture and Utilization of CO2for Syngas Production over Dual-Function Materials. *ACS Sustain Chem Eng*. 2018;6(10):13551-13561. doi:10.1021/acssuschemeng.8b03769

50. Krishnamurthy A, Thakkar H, Rownaghi AA, Rezaei F. Adsorptive Removal of Formaldehyde from Air Using Mixed-Metal Oxides. *Ind Eng Chem Res*. 2018;57(38):12916-12925. doi:10.1021/acs.iecr.8b02962

51. Monazam ER, Spenik J, Shadle LJ. CO2desorption kinetics for immobilized polyethylenimine (PEI). *Energy and Fuels*. 2014;28(1):650-656. doi:10.1021/ef401879z

52. Monazam E, Shadle L, Miller D, et al. Equilibrium and Kinetics Analysis of Carbon dioxide Capture using Immobilized Amine on a Mesoporous Silica. *Rom J Morphol Embryol*. 2013;59(3):923-935. doi:10.1002/aic

53. Stuckert NR, Yang RT. CO2 capture from the atmosphere and simultaneous concentration using zeolites and amine-grafted SBA-15. *Environ Sci Technol*. 2011;45(23):10257-10264. doi:10.1021/es202647a

54. Wang X, Schwartz V, Clark JC, et al. Infrared Study of CO2 Sorption over "Molecular Basket" Sorbent Consisting of Polyethylenimine-Modified Mesoporous Molecular Sieve. *J Phys Chem C*. 2009;113(17):7260-7268. doi:10.1021/jp809946y

55. Heydari-Gorji A, Sayari A. CO2 capture on polyethylenimine-impregnated hydrophobic mesoporous silica: Experimental and kinetic modeling. *Chem Eng J*. 2011;173(1):72-79. doi:10.1016/j.cej.2011.07.038

56. Brandani S, Ruthven DM. Analysis of ZLC desorption curves for gaseous systems. *Adsorption*. 1996;2(2):133-143. doi:10.1007/BF00127043

57. Brandani S. A Simple Graphical Check of Consistency for Zero Length Column Desorption Curves. *Chem Eng Technol*. 2016;39(6):1194-1198. doi:10.1002/ceat.201500634

58. Neimark A V., Thommes M, Sing KSW, et al. Physisorption of gases, with special reference to the evaluation of surface area and pore size distribution (IUPAC Technical Report). *Pure Appl Chem*. 2015;87(9-10):1051-1069. doi:10.1515/pac-2014-1117

59. Chaikittisilp W, Kim H, Jones CW. Mesoporous Alumina-Supported Amines as Potential Steam-Stable Adsorbents for Capturing CO 2 from Simulated Flue Gas and Ambient Air. 2011:5528-5537. doi:10.1021/ef201224v

60. Wang X, Ma X, Song C, et al. Molecular basket sorbents polyethylenimine–SBA-15 for CO2 capture from flue gas: Characterization and sorption properties. *Microporous Mesoporous Mater*. 2013;169:103-111. doi:10.1016/j.micromeso.2012.09.023

61. Jahandar Lashaki M, Sayari A. CO2 capture using triamine-grafted SBA-15: The impact of the support pore structure. *Chem Eng J*. 2018;334(August 2017):1260-1269. doi:10.1016/j.cej.2017.10.103

62. Sanz R, Calleja G, Arencibia A, Sanz-Pérez ES. CO2 uptake and adsorption kinetics of pore-expanded SBA-15 double-functionalized with amino groups. *Energy and Fuels*. 2013;27(12):7637-7644. doi:10.1021/ef4015229

63. Lin Y, Lin H, Wang H, et al. Enhanced selective CO2adsorption on polyamine/MIL-101(Cr) composites. *J Mater Chem A*. 2014;2(35):14658-14665. doi:10.1039/c4ta01174k

64. Serna-Guerrero R, Belmabkhout Y, Sayari A. Modeling CO2 adsorption on amine-functionalized mesoporous silica: 1. A semi-empirical equilibrium model. *Chem Eng J*. 2010;161(1-2):173-181. doi:10.1016/j.cej.2010.04.024

65. Serna-guerrero R, Sayari A. Modeling adsorption of CO 2 on amine-functionalized mesoporous silica . 2 : Kinetics and breakthrough curves. *Chem Eng J*. 2010;161:182-190. doi:10.1016/j.cej.2010.04.042

66. Yan X, Komarneni S, Yan Z. CO 2 adsorption on Santa Barbara Amorphous-15 (SBA-15) and amine-modified Santa Barbara Amorphous-15 (SBA-15) with and without controlled microporosity. *J Colloid Interface Sci*. 2013;390(1):217-224. doi:10.1016/j.jcis.2012.09.038

67. Zhang W, Liu H, Sun C, Drage TC, Snape CE. Performance of polyethyleneimine-silica adsorbent for post-combustion CO2capture in a bubbling fluidized bed. *Chem Eng J*. 2014;251:293-303. doi:10.1016/j.cej.2014.04.063

68. Drese JH, Choi S, Lively RP, et al. Synthesis-structure-property relationships for Hyperbranched aminosilica CO2 adsorbents. *Adv Funct Mater*. 2009;19(23):3821-3832. doi:10.1002/adfm.200901461

69. Neaton JB, Poloni R, Planas N, et al. The Mechanism of Carbon Dioxide Adsorption in an Alkylamine-Functionalized Metal–Organic Framework. *J Am Chem Soc*. 2013;135(20):7402-7405. doi:10.1021/ja4004766

70. Xu X, Song C, Andresen JM, Miller BG, Scaroni AW. Novel Polyethylenimine-Modified Mesoporous Molecular Sieve of MCM-41 Type as High-Capacity Adsorbent for CO2 Capture. *Energy and Fuels*. 2002;(16):1463-1469. doi:10.1021/ef020058u

71. Brandani F. Development and Application of the Zero Length Column (ZLC) Technique for Measuring Adsorption Equilibria. *Electron Theses Diss*. 2002.

72. Zhang Z, Huang S, Xian S, Xi H, Li Z. Adsorption equilibrium and kinetics of CO2 on chromium terephthalate MIL-101. *Energy and Fuels*. 2011;25(2):835-842. doi:10.1021/ef101548g

73. Gücüyener C, Van Den Bergh J, Gascon J, Kapteijn F. Ethane/ethene separation turned on its head: Selective ethane adsorption on the metal-organic framework ZIF-7 through a gate-opening mechanism. *J Am Chem Soc*. 2010;132(50):17704-17706. doi:10.1021/ja1089765

74. Serna-Guerrero R, Belmabkhout Y, Sayari A. Modeling CO2 adsorption on amine-functionalized mesoporous silica: 1. A semi-empirical equilibrium model. *Chem Eng J*. 2010;161(1-2):173-181. doi:10.1016/j.cej.2010.04.024

75. Belmabkhout Y. Adsorption of CO2-containing gas mixtures over amine-bearing pore-expanded MCM-41 silica: Application for gas purification. *Ind Eng …*. 2009;49(1):359-365. http://pubs.acs.org/doi/abs/10.1021/ie900837t.

76. Yang ST, Kim JY, Kim J, Ahn WS. CO2capture over amine-functionalized MCM-22, MCM-36 and ITQ-2. *Fuel*. 2012;97:435-442. doi:10.1016/j.fuel.2012.03.034

77. Ojeda M, Mazaj M, Garcia S, Xuan J, Maroto-Valer MM, Logar NZ. Novel Amine-impregnated Mesostructured Silica Materials for CO2Capture. *Energy Procedia*. 2017;114(November 2016):2252-2258. doi:10.1016/j.egypro.2017.03.1362

78. Bollini P, Brunelli NA, Didas SA, Jones CW. Dynamics of CO2 adsorption on amine adsorbents. 2. insights into adsorbent design. *Ind Eng Chem Res*. 2012;(51):15153-15162. doi:10.1021/ie3017913

79. Luo S, Chen S, Chen Y, Chen S, Ma N, Wu Q. Sisal fiber-based solid amine adsorbent and its kinetic adsorption behaviors for CO2. *RSC Adv*. 2016;6(76):72022-72029. doi:10.1039/c6ra14627a

80. Yin F, Zhuang L, Luo X, Chen S. Simple synthesis of nitrogen-rich polymer network and its further amination with PEI for CO2 adsorption. *Appl Surf Sci*. 2018;434:514-521. doi:10.1016/j.apsusc.2017.10.198

81. Tykodi RJ. Thermodynamics of adsorption. *J Chem Phys*. 1954. doi:10.1063/1.1739867

82. Kolasinski KW. Thermodynamics and Kinetics of Adsorption and Desorption. In: *Surface Science*. ; 2012. doi:10.1002/9781119941798.ch4

83. Serna-Guerrero R, Sayari A. Modeling adsorption of CO2 on amine-functionalized mesoporous silica. 2: Kinetics and breakthrough curves. *Chem Eng J*. 2010;161(1-2):182-190. doi:10.1016/j.cej.2010.04.042

## SUPPORTING INFORMATION

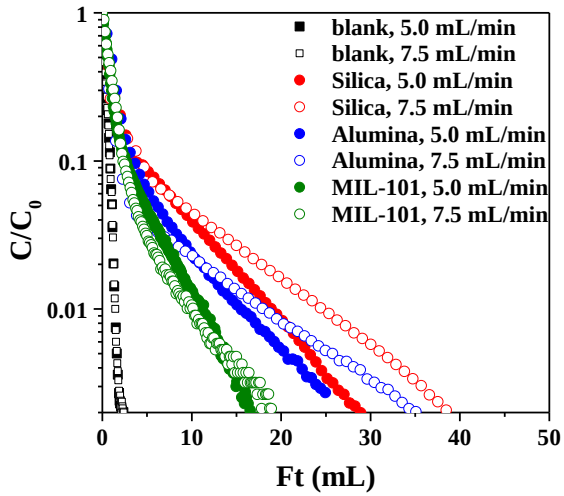


Figure S1. Experimental Ft (mL) plot demonstrating response and bare Silica, Alumina, and MIL-101 at 0.05 bar $CO_2$ in He at 25 °C.

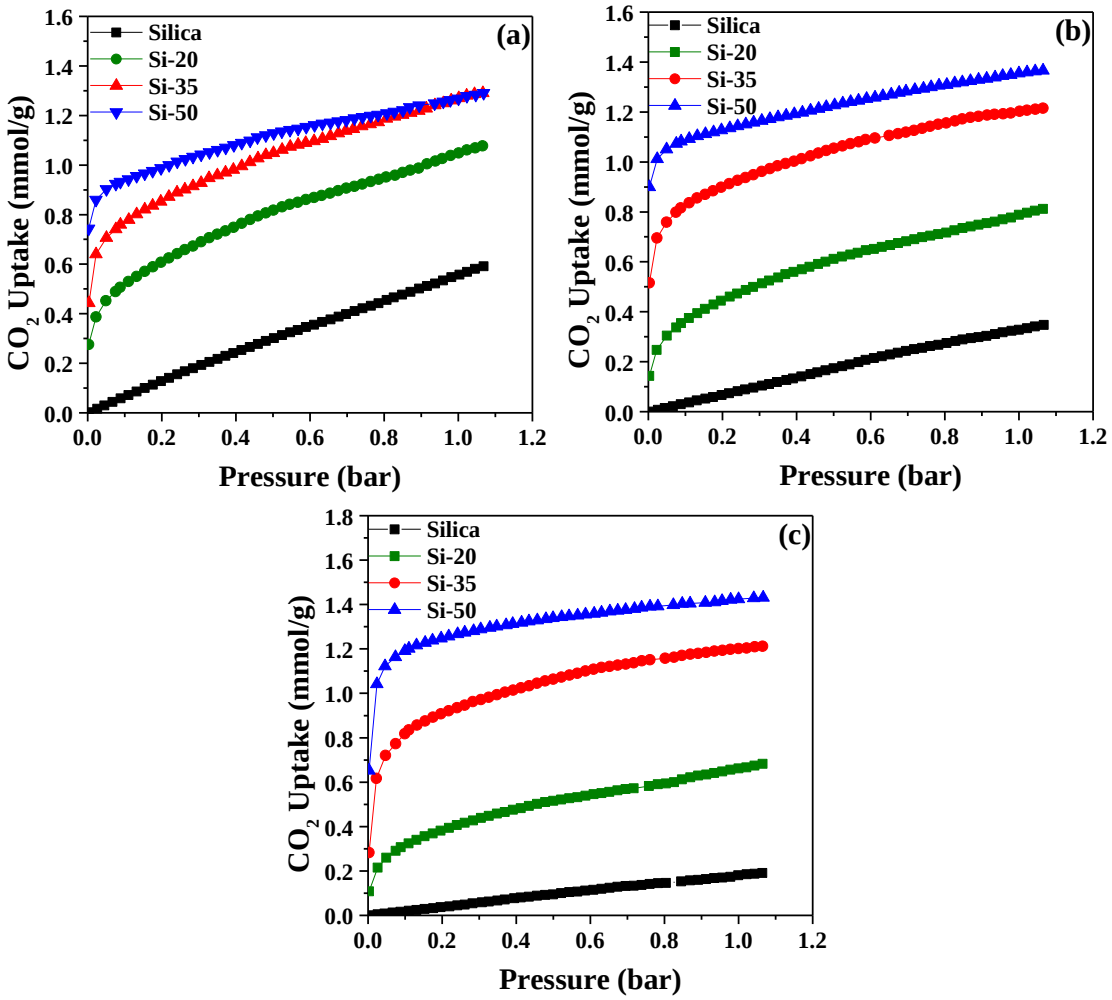


Figure S2. $CO_2$ adsorption isotherms for Silica, Si-20, Si-35, and Si-50 at (a) 25 °C, (b) 50 °C, and (c) 75 °C.

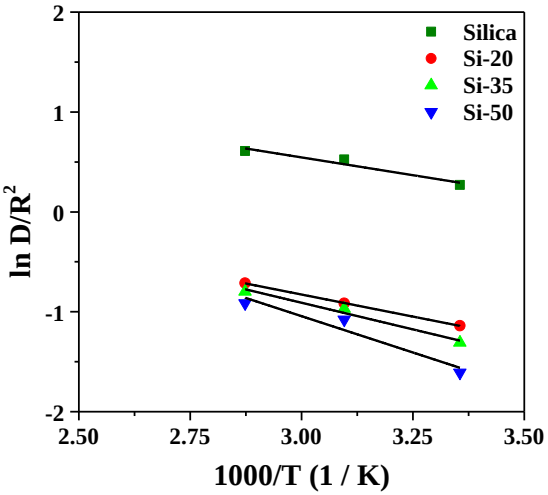


Figure S3. Arrhenius plot of $CO_2$ for Silica, Silica-20, Silica-35, and Silica-50.

Table S1. Diffusivity values for MIL-101 and PEI-MIL-101 at 25 °C.

| **Material** | **Flow Rate (mL/min)** | **$D_c/r_c^2$ x $10^3$ ($s^{-1}$)** | **$D_e/R^2$ x $10^3$ ($s^{-1}$)** | **L** |
|---|---|---|---|---|
| MIL-101 | 5.0 | 2.25 | - | 11 |
| | 7.5 | 2.28 | - | 33 |
| | 10.0 | 2.28 | - | 190 |
| **Avg** | | **2.27** | | |
| MIL-101-20 | 5.0 | - | 0.90 | 12 |
| | 7.5 | - | 0.90 | 45 |
| | 10.0 | - | 0.83 | 120 |
| **Avg** | | | **0.87** | |
| MIL-101-35 | 5.0 | - | 0.71 | 34 |
| | 7.5 | - | 0.71 | 53 |
| | 10.0 | - | 0.72 | 100 |
| **Avg** | | | **0.71** | |
| MIL-101-50 | 5.0 | - | 0.62 | 17 |
| | 7.5 | - | 0.71 | 39 |
| | 10.0 | - | 0.62 | 170 |
| **Avg** | | | **0.62** | |

Table S2. Diffusivity values for Alumina and PEI-Alumina at 25 °C.

| **Material** | **Flow Rate (mL/min)** | **-Slope x $10^2$ ($s^{-1}$)** | **$D_e/R^2$ x $10^3$ ($s^{-1}$)** | **L** |
|---|---|---|---|---|
| Alumina | 5.0 | 1.26 | - | 19 |
| | 7.5 | 1.24 | - | 35 |
| | 10.0 | 1.35 | - | 100 |
| **Avg** | | **1.25** | | |
| Al-20 | 5.0 | - | 0.79 | 10 |
| | 7.5 | - | 0.79 | 17 |
| | 10.0 | - | 0.80 | 39 |
| **Avg** | | | **0.79** | |
| Al-35 | 5.0 | - | 0.72 | 11 |
| | 7.5 | - | 0.75 | 21 |
| | 10.0 | - | 0.74 | 50 |
| **Avg** | | | **0.74** | |
| Al-50 | 5.0 | - | 0.66 | 17 |
| | 7.5 | - | 0.75 | 31 |
| | 10.0 | - | 0.65 | 100 |
| **Avg** | | | **0.69** | |

Table S3. Diffusivity values for Silica and PEI-Silica at 25 °C.

| **Material** | **Flow Rate (mL/min)** | **$D_s/R^2$ x $10^3$ ($s^{-1}$)** | **L** | **$D_e/R^2$ x $10^3$ ($s^{-1}$)** | **L** |
|---|---|---|---|---|---|
| Silica | 5.0 | - | - | 1.30 | 11 |
| | 7.5 | - | - | 1.31 | 16 |
| | 10.0 | - | - | 1.31 | 35 |
| **Avg** | | | | **1.31** | |
| Silica-20 | 5.0 | 0.73 | 13 | 0.31 | 65 |
| | 7.5 | 0.78 | 34 | 0.32 | 220 |
| | 10.0 | 0.73 | 88 | 0.33 | 300 |
| **Avg** | | **0.78** | | **0.32** | |
| Silica-35 | 5.0 | 0.70 | 15 | 0.25 | 100 |
| | 7.5 | 0.87 | 28 | 0.27 | 250 |
| | 10.0 | 0.70 | 81 | 0.29 | 300 |
| **Avg** | | **0.76** | | **0.27** | |
| Silica-50 | 5.0 | 0.70 | 14 | 0.18 | 110 |
| | 7.5 | 0.79 | 32 | 0.19 | 310 |
| | 10.0 | 0.69 | 82 | 0.23 | 410 |
| **Avg** | | **0.73** | | **0.20** | |

Table S4. Diffusivity values for Silica and PEI-Silica at 50 °C.

| **Material** | **Flow Rate (mL/min)** | **$D_s/R^2$ x $10^3$ ($s^{-1}$)** | **L** | **$D_e/R^2$ x $10^3$ ($s^{-1}$)** | **L** |
|---|---|---|---|---|---|
| Silica | 5.0 | - | - | 1.67 | 12 |
| | 7.5 | - | - | 1.70 | 14 |
| | 10.0 | - | - | 1.70 | 22 |
| **Avg** | | | | **1.69** | |
| Silica-20 | 5.0 | 0.65 | 12 | 0.41 | 22 |
| | 7.5 | 0.94 | 17 | 0.41 | 51 |
| | 10.0 | 0.95 | 38 | 0.40 | 130 |
| **Avg** | | **0.85** | | **0.41** | |
| Silica-35 | 5.0 | 0.79 | 10 | 0.38 | 26 |
| | 7.5 | 0.80 | 14 | 0.39 | 41 |
| | 10.0 | 0.75 | 26 | 0.38 | 66 |
| **Avg** | | **0.78** | | **0.38** | |
| Silica-50 | 5.0 | 0.70 | 11 | 0.35 | 33 |
| | 7.5 | 0.75 | 16 | 0.35 | 47 |
| | 10.0 | 0.76 | 26 | 0.32 | 78 |
| **Avg** | | **0.74** | | **0.34** | |

Table S5. Diffusivity values for Silica and PEI-Silica at 75 °C.

| **Material** | **Flow Rate (mL/min)** | **$D_s/R^2$ x $10^3$ ($s^{-1}$)** | **L** | **$D_e/R^2$ x $10^3$ ($s^{-1}$)** | **L** |
|---|---|---|---|---|---|
| Silica | 5.0 | - | - | 1.80 | 14 |
| | 7.5 | - | - | 1.87 | 23 |
| | 10.0 | - | - | 1.86 | 68 |
| **Avg** | | | | **1.84** | |
| Silica-20 | 5.0 | 0.90 | 8 | 0.49 | 23 |
| | 7.5 | 0.94 | 12 | 0.49 | 33 |
| | 10.0 | 0.90 | 26 | 0.47 | 72 |
| **Avg** | | **0.91** | | **0.48** | |
| Silica-35 | 5.0 | 0.92 | 8 | 0.45 | 35 |
| | 7.5 | 0.90 | 25 | 0.45 | 100 |
| | 10.0 | 0.87 | 53 | 0.46 | 170 |
| **Avg** | | **0.90** | | **0.45** | |
| Silica-50 | 5.0 | 0.91 | 8 | 0.40 | 46 |
| | 7.5 | 0.90 | 17 | 0.41 | 74 |
| | 10.0 | 0.81 | 46 | 0.40 | 144 |
| **Avg** | | **0.87** | | **0.40** | |

# SECTION

# 2. CONCLUSIONS

The separation of olefins from paraffins via cryogenic distillation and $CO_2$ from post-combustion flue gases via aqueous amine-absorption represent some of the most technologically mature and costly gas separation processes seen in industry. In order to provide insight into alternative solid-state adsorption gas separation methods, this study focused on providing novel characterizations of the transport kinetics of different promising adsorbents utilizing the ZLC technique.

Single and binary gas mixtures of ethane and ethylene were tested over paraffin-selective MOFs ZIF-7 and Ni-BT powder and pellet samples. The results of this study found that the diffusivity of ethane measured was slightly reduced from single to binary component trials, signifying the effects of coadsorption were present for both MOF materials. Additionally, it was found that the diffusion of ethylene was significantly affected by surface resistances due to strong interactions between the C-C double bonds at pore entrances.

$CO_2$ sorption kinetics were tested over three PEI-impregnated adsorbents, namely, MIL-101, γ-alumina, and UVM-7 silica, at three different amine contents at 25 °C. The results of this study found that both the amine-content and the porosity of the support are crucial in mitigating diffusional resistances of $CO_2$ within the amine-impregnated adsorbents. For all three materials it was found that as PEI-content was increased, $CO_2$ diffusion was reduced. Moreover, the PEI-silica was further tested a 50 and 75 °C, where

it was found that diffusion was enhanced at higher temperatures. Interestingly, the ZLC response curves of PEI-silica revealed two distinct regions of mass transfer control highlighting the influence of the independent mechanisms of physical and chemical diffusion on these materials. This study highlighted the importance of selecting PEI-adsorbents that exhibit both fast desorption kinetics and high working capacities.

## 2.1 FUTURE WORK ON OLEFIN/PARAFFIN SEPARATION

For the studies on olefin/paraffin separations, future work should focus on cyclic and stability testing of Ni-BT and ZIF-7 powders and pellets in order to determine changes that may occur in the diffusion kinetics over prolonged use, as well as to determine the overall long-term durability and efficacy of these materials.

## 2.2 FUTURE WORK ON ANTROPOGENIC $CO_2$ CAPTURE

Similarly, for the studies on $CO_2$ capture for PEI-impregnated MIL-101, γ-alumina, and UVM-7 silica, the powders should be synthesized into structured adsorbents and tested for their respective diffusivities. Other amines should be functionalized to these supports and tested for their respective diffusivities in order to provide comparisons onto the influence of amine type and size on $CO_2$ sorption kinetics. Once this has been completed, the materials should be tested to determine the concentration of irreversibly-adsorbed $CO_2$ due to chemical adsorption on each material, and then finally cyclic and stability testing should be conducted.

# REFERENCES

[1] R.B. Eldridge, Olefin/Paraffin Separation Technology: A Review, Ind. Eng. Chem. Res. 32 (1993) 2208–2212. doi:10.1021/ie00022a002.

[2] U.S. Department of Energy, Materials for separation technologies: energy and emission reduction opportunities, (2005) v. doi:10.2172/1218755.

[3] T. Ren, M. Patel, K. Blok, Olefins from conventional and heavy feedstocks: Energy use in steam cracking and alternative processes, Energy. 31 (2006) 425–451. doi:10.1016/j.energy.2005.04.001.

[4] D.J. Safarik, R.B. Eldridge, Olefin/paraffin separations by reactive absorption: a review, Ind. Eng. Chem. Res. 37 (1998) 2571–2581. doi:10.1021/ie970897h.

[5] J. Chen, B. Eldridge, E. Rosen, C. Bielawski, A Study of Cu(I)-Ethylene Complexatiopn for Olefin-Paraffin Separation, AIChE J. 57 (2010) 630–644. doi:10.1002/aic.

[6] M. Jiang, M. Eić, Transport properties of ethane, butanes and their binary mixtures in MFI-type zeolite and zeolite-membrane samples, Adsorption. 9 (2003) 225–234. doi:10.1023/A:1024797716739.

[7] M. Takht Ravanchi, T. Kaghazchi, A. Kargari, Application of membrane separation processes in petrochemical industry: a review, Desalination. 235 (2009) 199–244. doi:10.1016/j.desal.2007.10.042.

[8] R.W. Baker, Future directions of membrane gas separation technology, Ind. Eng. Chem. Res. 41 (2002) 1393–1411. doi:10.1021/ie0108088.

[9] I. Pinnau, L.G. Toy, Solid polymer electrolyte composite membranes for olefin / paraffin separation, J. Memb. Sci. 184 (2001) 39–48.

[10] K. ichi Okamoto, S. Kawamura, M. Yoshino, H. Kita, Y. Hirayama, N. Tanihara, Y. Kusuki, Olefin/paraffin separation through carbonized membranes derived from an asymmetric polyimide hollow fiber membrane, Ind. Eng. Chem. Res. 38 (1999) 4424–4432. doi:10.1021/ie990209p.

[11] M. Rungta, C. Zhang, W.J. Koros, L. Xu, Membrane-based ethylene/ethane separation: The upper bound and beyond, AIChE J. (2013). doi:10.1002/aic.14105.

[12] J. Padin, S.U. Rege, R.T. Yang, L.S. Cheng, Molecular sieve sorbents for kinetic separation of propane/propylene, Chem. Eng. Sci. 55 (2000) 4525–4535. doi:10.1016/S0009-2509(00)00099-3.

[13] C.A. Grande, A.E. Rodrigues, Adsorption Kinetics of Propane and Propylene in Zeolite 4A, Chem. Eng. Res. Des. 82 (2004) 1604–1612. doi:10.1205/cerd.82.12.1604.58029.

[14] S.U. Rege, J. Padin, R.T. Yang, Olefin/Paraffin Separations by Adsorption: π-Complexation vs. Kinetic Separation, AIChE J. 44 (1998) 799–809. doi:10.1002/aic.690440405.

[15] J. Padin, R.T. Yang, New sorbents for olefin / paraffon separations by adsorption via pi-complexation : synthesis and effects of substrates, Chem. Eng. Sci. 55 (2000) 2607–2616.

[16] D.M. Ruthven, S.C. Reyes, Adsorptive separation of light olefins from paraffins, Microporous Mesoporous Mater. 104 (2007) 59–66. doi:10.1016/j.micromeso.2007.01.005.

[17] M.C. Kroon, L.F. Vega, Selective paraffin removal from ethane/ethylene mixtures by adsorption into aluminum methylphosphonate-α: A molecular simulation study, Langmuir. 25 (2009) 2148–2152. doi:10.1021/la803042z.

[18] H. Leclerc, A. Vimont, J.C. Lavalley, M. Daturi, A.D. Wiersum, P.L. Llwellyn, P. Horcajada, G. Férey, C. Serre, Infrared study of the influence of reducible iron(III) metal sites on the adsorption of CO, CO2, propane, propene and propyne in the mesoporous metalorganic framework MIL-100, Phys. Chem. Chem. Phys. 13 (2011) 11748–11756. doi:10.1039/c1cp20502a.

[19] E. Bloch, W. Queen, R. Krishna, J. Zadrozny, C. Brown, J. Long, Hydrocarbon Separations in a Metal-Organic Framework with Open Iron(II) Coordination Sites, Science (80-. ). 335 (2012) 1606–1610.

[20] J. Van Den Bergh, C. Gücüyener, E.A. Pidko, E.J.M. Hensen, J. Gascon, F. Kapteijn, Understanding the anomalous alkane selectivity of ZIF-7 in the separation of light alkane/alkene mixtures, Chem. - A Eur. J. 17 (2011) 8832–8840. doi:10.1002/chem.201100958.

[21] C. Gücüyener, J. Van Den Bergh, J. Gascon, F. Kapteijn, Ethane/ethene separation turned on its head: Selective ethane adsorption on the metal-organic framework ZIF-7 through a gate-opening mechanism, J. Am. Chem. Soc. 132 (2010) 17704–17706. doi:10.1021/ja1089765.

[22] W. Liang, F. Xu, X. Zhou, J. Xiao, Q. Xia, Y. Li, Z. Li, Ethane selective adsorbent Ni ( bdc )( ted ) 0 . 5 with high uptake and its signi fi cance in adsorption separation of ethane and ethylene, Chem. Eng. Sci. 148 (2016) 275–281. doi:10.1016/j.ces.2016.04.016.

[23] H. Furukawa, K.E. Cordova, M. O'Keeffe, O.M. Yaghi, The chemistry and applications of metal-organic frameworks, Science (80-. ). 341 (2013). doi:10.1126/science.1230444.

[24] S.L. James, Metal-organic frameworks, Chem. Soc. Rev. 32 (2003) 276–288. doi:10.1039/b200393g.

[25] H.C. Zhou, J.R. Long, O.M. Yaghi, Introduction to metal-organic frameworks, Chem. Rev. 112 (2012) 673–674. doi:10.1021/cr300014x.

[26] H. Furukawa, N. Ko, Y.B. Go, N. Aratani, S.B. Choi, E. Choi, a O. Yazaydin, R.Q. Snurr, M. O'Keeffe, J. Kim, O.M. Yaghi, Ultrahigh Porosity in Meta-Organic Frameworks, Science (80-. ). 329 (2010) 424. doi:10.1126/science.1192160.

[27] J.R. Li, R.J. Kuppler, H.C. Zhou, Selective gas adsorption and separation in metal-organic frameworks, Chem. Soc. Rev. 38 (2009) 1477–1504. doi:10.1039/b802426j.

[28] H. Thakkar, Q. Al-Naddaf, N. Legion, M. Hovis, A. Krishnamurthy, A.A. Rownaghi, F. Rezaei, Adsorption of Ethane and Ethylene over 3D-Printed Ethane-Selective Monoliths, ACS Sustain. Chem. Eng. (2018) in press.

[29] F. Rezaei, P. Webley, Structured adsorbents in gas separation processes, Sep. Purif. Technol. 70 (2010) 243–256. doi:10.1016/j.seppur.2009.10.004.

[30] U.S.E.I.A. EIA, Annual Energy Outlook 2015, Off. Integr. Int. Energy Anal. (2015). doi:DOE/EIA-0383(2013).

[31] Intergovernmental Panel on Climate Change, International Cooperation: Agreements & Instruments, in: Clim. Chang. 2014 Mitig. Clim. Chang., 2015. doi:10.1017/cbo9781107415416.019.

[32] N.L. Bindoff, P.J. Durack, A. Slater, P. Cameron-Smith, Y. Chikamoto, O. Clifton, P.J. Durack, P. Ginoux, M. Holland, C. Holmes, J. Infanti, D. Jacob, J. John, T. Knutson, D. Lawrence, J. Lu, D. Murphy, V. Naik, A. Robock, A. Slater, S. Vavrus, P. Cameron-Smith, Y. Chikamoto, M. Ishii, S. Corti, T. Fichefet, J. García-Serrano, V. Guemas, L. Rodrigues, L. Gray, E. Hawkins, D. Smith, D.S. Stevenson, A. Voulgarakis, A. Weisheimer, O. Wild, T. Woollings, P. Young, V. Guemas, G. Krinner, Z. Klimont, Z. Klimont, J. Lu, V. Naik, J. Sedláček, B. van den Hurk, T. van Noije, A. Voulgarakis, A. Weisheimer, Near-term climate change: Projections and predictability, in: Clim. Chang. 2013 Phys. Sci. Basis Work. Gr. I Contrib. to Fifth Assess. Rep. Intergov. Panel Clim. Chang., 2013: pp. 953–1028. doi:10.1017/CBO9781107415324.023.

[33] T.R. Karl, K.E. Trenberth, Modern Global Climate Change, Science (80-. ). 302 (2003) 1719–1723. doi:10.1126/science.1090228.

[34] A. Al-Mamoori, A. Krishnamurthy, A. a. Rownaghi, F. Rezaei, Carbon Capture and Utilization Update, Energy Technol. 5 (2017) 834–849. doi:10.1002/ente.201600747.

[35] R. Stuart Haszeldine, Carbon capture and storage: how green can black be?, Science (80-. ). 325 (2009) 1647–1652. doi:10.1126/science.1172246.

[36] P. Markewitz, W. Kuckshinrichs, W. Leitner, J. Linssen, P. Zapp, R. Bongartz, A. Schreiber, T.E. Müller, Worldwide innovations in the development of carbon capture technologies and the utilization of CO<inf>2</inf>, Energy Environ. Sci. 5 (2012) 7281–7305. doi:10.1039/c2ee03403d.

[37] W.L. Ellsworth, Injection-induced earthquakes, Science (80-. ). (2013). doi:10.1126/science.1225942.

[38] International Energy Agency, Energy and climate change. World energy outlook special report, 2015. doi:10.1038/479267b.

[39] S. Japip, H. Wang, Y. Xiao, T.S. Chung, Highly permeable zeolitic imidazolate framework (ZIF)-71 nano-particles enhanced polyimide membranes for gas separation, J. Memb. Sci. (2014). doi:10.1016/j.memsci.2014.05.025.

[40] T.C. Merkel, H. Lin, X. Wei, R. Baker, Power plant post-combustion carbon dioxide capture: An opportunity for membranes, J. Memb. Sci. (2010). doi:10.1016/j.memsci.2009.10.041.

[41] S. Builes, P. López-Aranguren, J. Fraile, L.F. Vega, C. Domingo, Analysis of CO<inf>2</inf> adsorption in amine-functionalized porous silicas by molecular simulations, Energy and Fuels. (2015). doi:10.1021/acs.energyfuels.5b00781.

[42] G.T. Rochelle, Amine Scrubbing for CO2 Capture, Science (80-. ). 325 (2009) 1652–1655. doi:10.1126/science.1176731.

[43] D. Leung, G. Caramanna, M. Maroto-Valer, An overview of current status of carbon dioxide capture and storage technologies, Renew. Sustain. Energy Rev. 39 (2018) 426–443. doi:10.1016/j.rser.2014.07.093.

[44] S. Choi, J.H. Drese, C.W. Jones, Adsorbent materials for carbon dioxide capture from large anthropogenic point sources, ChemSusChem. (2009). doi:10.1002/cssc.200900036.

[45] H. Yang, Z. Xu, M. Fan, R. Gupta, R.B. Slimane, A.E. Bland, I. Wright, Progress in carbon dioxide separation and capture: A review, J. Environ. Sci. 20 (2008) 14–27. doi:10.1016/S1001-0742(08)60002-9.

[46] Y.S. Bae, R.Q. Snurr, Development and evaluation of porous materials for carbon dioxide separation and capture, Angew. Chemie - Int. Ed. 50 (2011) 11586–11596. doi:10.1002/anie.201101891.

[47] C. Yu, C. Huang, C. Tan, A Review of CO 2 Capture by Absorption and Adsorption, Aerosol Air Qual. Res. (2012) 745–769. doi:10.4209/aaqr.2012.05.0132.

[48] L.A. Darunte, K.S. Walton, D.S. Sholl, C.W. Jones, CO2capture via adsorption in amine-functionalized sorbents, Curr. Opin. Chem. Eng. 12 (2016) 82–90. doi:10.1016/j.coche.2016.03.002.

[49] C. Chen, J. Kim, W.S. Ahn, CO2 Capture by amine-functionalized nanoporous materials: A review, Korean J. Chem. Eng. 31 (2014) 1919–1934. doi:10.1007/s11814-014-0257-2.

[50] G. Qi, Y. Wang, L. Estevez, X. Duan, N. Anako, A.A. Park, W. Li, W. Jones, E.P. Giannelis, High efficiency nanocomposite sorbents for CO 2 capture based on amine-functionalized mesoporous capsules †, (2011) 444–452. doi:10.1039/c0ee00213e.

[51] R.A. Khatri, S.S.C. Chuang, Y. Soong, M. Gray, Thermal and chemical stability of regenerable solid amine sorbent for CO2capture, Energy and Fuels. (2006). doi:10.1021/ef050402y.

[52] W.J. Son, J.S. Choi, W.S. Ahn, Adsorptive removal of carbon dioxide using polyethyleneimine-loaded mesoporous silica materials, Microporous Mesoporous Mater. 113 (2008) 31–40. doi:10.1016/j.micromeso.2007.10.049.

[53] S. Gaikwad, S.J. Kim, S. Han, CO2 capture using amine-functionalized bimetallic MIL-101 MOFs and their stability on exposure to humid air and acid gases, Microporous Mesoporous Mater. 277 (2019) 253–260. doi:10.1016/j.micromeso.2018.11.001.

[54] A.G. Slater, A.I. Cooper, Function-led design of new porous materials, Science (80-. ). 348 (2015) aaa8075. doi:10.1126/science.aaa8075.

[55] X. Xu, C. Song, J.M. Andrésen, B.G. Miller, A.W. Scaroni, Preparation and characterization of novel CO2"molecular basket" adsorbents based on polymer-modified mesoporous molecular sieve MCM-41, Microporous Mesoporous Mater. 62 (2003) 29–45. doi:10.1016/S1387-1811(03)00388-3.

[56] H.Y. Huang, R.T. Yang, D. Chinn, C.L. Munson, Amine-grafted MCM-48 and silica xerogel as superior sorbents for acidic gas removal from natural gas, Ind. Eng. Chem. Res. (2003). doi:10.1021/ie020440u.

[57] Y. Labreche, Y. Fan, F. Rezaei, R.P. Lively, C.W. Jones, W.J. Koros, Poly(amide-imide)/silica supported PEI hollow fiber sorbents for postcombustion $CO_2$ capture by RTSA, ACS Appl. Mater. Interfaces. 6 (2014) 19336–19346. doi:10.1021/am505419w.

[58] M. Eic, D.M. Ruthven, A new experimental technique for measurement of intracrystalline diffusivity, Zeolites. 8 (1988) 40–45. doi:10.1016/S0144-2449(88)80028-9.

[59] S. Brandani, D.M. Ruthven, Analysis of ZLC desorption curves for gaseous systems, Adsorption. 2 (1996) 133–143. doi:10.1007/BF00127043.

[60] J.A.C. Silva, A.E. Rodrigues, Analysis of ZLC technique for diffusivity measurements in bidisperse porous adsorbent pellets, Gas Sep. Purif. (1996). doi:10.1016/S0950-4214(96)00021-7.

[61] S. Brandani, Effects of nonlinear equilibrium on zero length column experiments, Chem. Eng. Sci. 53 (1998) 2791–2798. doi:10.1016/S0009-2509(98)00075-X.

[62] S. Brandani, Analytical solution for ZLC desorption curves with bi-porous adsorbent particles, Chem. Eng. Sci. 51 (1996) 3283–3288. doi:10.1016/0009-2509(95)00399-1.

[63] S. Brandani, D.M. Ruthven, Analysis of ZLC desorption curves for liquid systems, Adsorption. 50 (1995) 2055–2059. doi:10.1007/BF00127043.

[64] S. Brandani, C. Cavalcante, A. Guimaraes, D.M. Ruthven, Heat Effects in ZLC Experiments, Adsorption. 4 (1998) 275–285. doi:Doi 10.1023/A:1008837801299.

[65] J.C.A. Silva, F.A. da Silva, A.E. Rodrigues, An analytical solution for the analysis of zero-length-column experiments with heat effects, Ind. Eng. Chem. Res. 40 (2001) 3697–3702. doi:10.1021/ie001045b.

[66] D. Ruthven, F. Brandani, ZLC response for systems with surface resistance control, Adsorption. 11 (2005) 31–34. doi:10.1007/s10450-005-1090-z.

[67] D.M. Ruthven, A. Vidoni, ZLC diffusion measurements: Combined effect of surface resistance and internal diffusion, Chem. Eng. Sci. 71 (2012) 1–4. doi:10.1016/j.ces.2011.11.040.

[68] S. Brandani, M.A. Jama, D.M. Ruthven, ZLC measurements under non-linear conditions, Chem. Eng. Sci. 55 (2000) 1205–1212. doi:10.1016/S0009-2509(99)00411-X.

[69] F. Brandani, D. Ruthven, Measurement of Adsorption Equilibria by the Zero Length Column (ZLC) Technique Part 2: Binary Systems, Ind. Eng. Chem. Res. 42 (2003) 1462–1469. doi:10.1021/ie020573f.

[70] F. Brandani, D. Ruthven, C.G. Coe, Measurement of adsorption equilibrium by the zero length column (ZLC) technique part 1: Single-component systems, Ind. Eng. Chem. Res. 42 (2003) 1451–1461. doi:10.1021/ie020572n.

[71] X. Hu, S. Brandani, A.I. Benin, R.R. Willis, Testing the stability of novel adsorbents for carbon capture applications using the zero length column technique, Chem. Eng. Res. Des. 131 (2018) 406–413. doi:10.1016/j.cherd.2018.01.023.

[72] S.F. Zaman, K.F. Loughlin, S.A. Al-Khattaf, Kinetics of desorption of 1,3-diisopropylbenzene and 1,3,5-triisopropylbenzene. 2. Diffusion in FCC catalyst particles by zero length column method, Ind. Eng. Chem. Res. 54 (2015) 4572–4580. doi:10.1021/ie504963e.

[73] N. Gargiulo, P. Aprea, D. Caputo, M. Eic, Q. Huang, C. Colella, Adsorption and Diffusion of Carbon Dioxide in Polyethylenimine-Modified SBA-15 Silicas, in: Spec. Top. Mater. Sci. Technol., [Sel. Pap. Natl. Conf.], 9th, 2008: pp. 213–220. doi:10.1163/ej.9789004172241.i-420.158.

# VITA

Teresa Gelles was born in Rolla, Missouri. Growing up in Rolla, she graduated from Rolla High School in 2012. After which, she attended Carnegie Mellon University in Pittsburgh, PA and graduated with a bachelor of science in Chemical Engineering in the spring of 2016. She enrolled in the master's degree program in Chemical Engineering at Missouri University of Science and Technology in the fall of 2017. At Missouri S&T, she has carried out research under the guidance of Dr. Fateme Rezaei, investigating the diffusion kinetics of promising adsorbent for gas capture and abatement processes. She received her master of science in Chemical Engineering from Missouri University of Science and Technology in May 2019.